

11-18-2015

Dynamic Phasor Based Analysis and Control in Renewable Energy Integration

Lakshan Prageeth Piyasinghe

University of South Florida, lakshan@mail.usf.edu

Follow this and additional works at: <http://scholarcommons.usf.edu/etd>

 Part of the [Electrical and Computer Engineering Commons](#)

Scholar Commons Citation

Piyasinghe, Lakshan Prageeth, "Dynamic Phasor Based Analysis and Control in Renewable Energy Integration" (2015). *Graduate Theses and Dissertations*.

<http://scholarcommons.usf.edu/etd/6015>

This Dissertation is brought to you for free and open access by the Graduate School at Scholar Commons. It has been accepted for inclusion in Graduate Theses and Dissertations by an authorized administrator of Scholar Commons. For more information, please contact scholarcommons@usf.edu.

Dynamic Phasor Based Analysis and Control in Renewable Energy Integration

by

Lakshan Piyasinghe

A dissertation submitted in partial fulfillment
of the requirements for the degree of
Doctor of Philosophy
Department of Electrical Engineering
College of Engineering
University of South Florida

Major Professor: Zhixin Miao, Ph.D.
Lingling Fan, Ph.D.
Fangxing Li, Ph.D.
Stephen Sadow, Ph.D.
Lee (Elias) Stefanakos, Ph.D.
Bo Zeng, Ph.D.

Date of Approval:
October 30, 2015

Keywords: Impedance model, DFIG, PV, TCSC, Stability, VSC, Resonance, Microgrid

Copyright © 2015, Lakshan Piyasinghe

DEDICATION

To my mother, my wife, my sister, my brothers, my friends and my teachers.

ACKNOWLEDGMENTS

First of all, I would like to express my deepest gratitude to my advisor Dr. Zhixin Miao for his guidance, caring, and providing me with an excellent atmosphere to do research.

Secondly, I would like to thank the rest of my committee members: Dr. Lingling Fan, Dr. Fangxing Li, Dr. Stephen Sadow Dr. Lee (Elias) Stefanakos and Dr. Bo Zeng for their encouragement and constructive comments. I would like to especially thank Dr. Lingling Fan for guiding in research for the past several years and helping me to develop my research skills.

I would like to thank Javad Khazaei, who was always willing to help as a good friend and an excellent team player. I would like to extend my gratitude to my recent and former colleagues from the smart grid power system lab, in particular Mohemmed Alhaider, Hossein Ghassempour, Ahmed Tazey, Yin Li, Yan Ma, Yi Zhou, Mingyue Ma, Yangkun Xu, Dr. Haiping yin, Dr. Yasser Wehbe, Dr. Ling Xu and Dr. Vahid Rasouli for all the discussions, help and enjoyable time I spent with them.

Last but not the least, I would like to thank my wife, Sandamali Halpegamage, my mother, Anoma Weeraman, my brothers, Chamika, Nishan and Rumes, my sister, Bhagya for all the encouragement, love and the support they provided from the beginning.

TABLE OF CONTENTS

LIST OF TABLES	iv
LIST OF FIGURES	v
ABSTRACT	x
CHAPTER 1 INTRODUCTION	1
1.1 Background	1
1.2 Statement of Problem	3
1.3 Outline of the Dissertation	5
CHAPTER 2 REVIEW OF RELEVANT LITERATURE AND THEORY	6
2.1 Dynamic Phasor Based Modeling and Analysis	6
2.1.1 Dynamic Phasor Concept	7
2.2 Impedance Modeling	7
2.2.1 Impedance Based Nyquist Stability Criterion	8
2.3 Dynamic Phasor Based Impedance Modeling and Analysis	8
CHAPTER 3 INITIALIZATION OF SYSTEMS WITH RENEWABLE INTEGRATION	9
3.1 Introduction	9
3.2 Analytical Modeling and Initializing of DFIG	9
3.2.1 Steady State Model of a Wind Farm	10
3.2.1.1 Wind Turbine Model	11
3.2.1.2 DFIG Model	11
3.2.1.3 Power Losses Inside the Wind Farm	12
3.2.2 Steady State Operating Conditions	13
3.3 Sweeping Method Implementation for Unbalanced Network	15
3.3.1 The Study System	16
3.3.2 Sweeping Method Procedure	17
3.3.3 Induction Machine Model and Initialization	19
3.3.4 Case Study	21
3.3.4.1 Case 1: Balanced System	22
3.3.4.2 Case 2: Unbalanced System	23
CHAPTER 4 DYNAMIC PHASOR BASED SSR ANALYSIS OF DFIGS	26
4.1 Introduction	26
4.2 Impedance Model of TCSC	27
4.2.1 Impedance Model with Fixed α	30

4.2.2	Impedance Model with α Control	31
4.3	Frequency Domain Analysis	32
4.3.1	Stability Criterion	32
4.3.2	Case Study	33
4.3.2.1	Fixed Series Compensation	35
4.3.2.2	TCSC Effect	37
4.4	Time-Domain Simulation Results	39
4.4.1	Scenario One	40
4.4.1.1	Effect of Different TCSC Gains	40
4.4.1.2	Effect of Different TCSC Compensation Level	42
4.4.1.3	Effect of Different RSC Gains	42
4.4.2	Scenario Two	44
4.4.2.1	Effect of Different Fixed Capacitor Compensation Level	44
4.4.2.2	Comparison of TCSC and Fixed Capacitor	45
4.5	Conclusion	46
CHAPTER 5 MODELING OF MICROGRIDS IN UNBALANCED CONDITIONS		47
5.1	Introduction	47
5.2	Dynamic Phasor Approach	49
5.3	System Configuration and Modeling	50
5.3.1	DP Model of a Single-Phase PV	51
5.3.1.1	DP Model of a PR Controller	53
5.3.2	DP Model of an Induction Machine	54
5.3.3	PFC and the Integrated System	56
5.4	Case Studies	57
5.4.1	Case Study 1	58
5.4.2	Case Study 2	59
5.4.3	Case Study 3	62
5.4.4	Remarks on Simulation Time	63
5.5	Conclusion	64
CHAPTER 6 PREDICTION AND OPTIMIZATION CONTROL FOR A MICROGRID		66
6.1	Introduction	66
6.2	Test System	69
6.3	ARMA Model for Estimation of Load and PV	69
6.4	Upper-Level Model Predictive Control Based Optimization	71
6.4.1	The Optimization Problem	72
6.4.2	Prediction Procedure	74
6.5	Lower-level Converter Controls	75
6.5.1	Power Control Loops	77
6.5.2	Inner Current Control Loops	78
6.6	Tests	78
6.6.1	Test 1: Prediction Validation in Simulink	79
6.6.2	Test 1: Peak Shaving at Grid-Connected Mode	80
6.6.3	Test 2: Sensitivity Analysis of Battery Size	81
6.6.4	Test 3: Real-time Simulator Performance	83

6.7	Conclusion	83
CHAPTER 7 MICROGRID OPERATION WITH INTERMITTENT LOADS		85
7.1	Introduction	85
7.2	Power Management in Microgrid Systems	86
7.3	Study System	88
7.3.1	Diesel Engine Synchronous Generator	89
7.3.2	VSC Based Inverter	89
7.3.3	PPL Model and Control	91
7.4	Simulation Results	92
7.4.1	Passive Control of the Inverter	94
7.4.2	Active Control of the Inverter	95
7.4.2.1	Centralized Control	95
7.4.2.2	Decentralized Control	96
7.5	Conclusion	98
CHAPTER 8 RT-LAB MODELING AND HIL SETUP FOR MICROGRIDS		101
8.1	Introduction	101
8.2	Real-Time Simulation and Hardware-In-The-Loop Tests of a Battery System	101
8.2.1	System Topology	102
8.2.1.1	HIL Testbed Setup	103
8.2.1.2	Battery Inverter Control	104
8.2.1.3	Coordinated Control of Battery and PV	105
8.2.2	Simulation Results for Battery Performance in Microgrid	105
8.2.2.1	Base Case	105
8.2.2.2	Performance of PV and Battery	106
8.2.2.3	Simulation Results Considering SOC Limits	106
8.2.3	HIL Experiments Results	107
8.3	Real-Time Modeling of Single-Phase PV in RT-LAB	109
8.3.1	System Configuration	110
8.3.2	PV Control	110
8.3.2.1	MPPT Control	110
8.3.2.2	Proportional Controller (PR)	112
8.3.3	Case Studies	113
8.3.3.1	Normal Case	113
8.3.3.2	Experimental Case with External Input	114
CHAPTER 9 CONCLUSIONS		118
REFERENCES		119
APPENDICES		128
Appendix A	Reuse Permissions of Published Papers for Chapters 3, 4, 5, 7, 8	129
ABOUT THE AUTHOR		End Page

LIST OF TABLES

Table 3.1	Parameters of the induction generator	25
Table 3.2	Data of the lines in network	25
Table 4.1	Parameters of the transmission lines	34
Table 4.2	Different reference impedance of TCSC for different compensation levels	37
Table 5.1	Eigenvalues of the system without PV	60
Table 5.2	Eigenvalues of the system with PV	60
Table 5.3	Eigenvalue comparison for different grid length	61
Table 5.4	Comparison of simulation time between two models	63
Table 5.5	Parameters of the induction machine	65
Table 5.6	Parameters of the PV	65
Table 5.7	Line data of the network	65
Table 6.1	Obtained ARMA model parameters for PV and load	71
Table 6.2	Parameters of the optimization problem	73
Table 6.3	Parameters of the system	84
Table 7.1	PPL model parameters	92
Table 7.2	Synchronous generator parameters in per unit	92
Table 7.3	Inverter model parameters	92
Table 8.1	Simulation system parameters	103

LIST OF FIGURES

Figure 1.1	Microgrid control level hierarchy.	2
Figure 2.1	Voltage source and a load.	8
Figure 3.1	Wind turbine and DFIG.	10
Figure 3.2	Equivalent circuit diagram of DFIG.	12
Figure 3.3	Iterative model for optimal power flow and steady state calculations.	14
Figure 3.4	The system under study.	16
Figure 3.5	The connection of PV and an LCL filter to the grid.	17
Figure 3.6	Flowchart of the sweeping method.	19
Figure 3.7	Conversion from abc to pnz and back to abc for an induction machine.	19
Figure 3.8	PCC voltages in balanced case.	22
Figure 3.9	Grid current and IM current.	22
Figure 3.10	Rotor speeds in balanced case.	23
Figure 3.11	Simulation results of sweeping method for voltages in unbalanced case.	24
Figure 3.12	Simulation results of sweeping method for currents in unbalanced case.	24
Figure 3.13	Simulation results of sweeping method for rotor speed in unbalanced case.	24
Figure 4.1	TCSC circuit diagram.	28
Figure 4.2	TCSC waveforms.	28
Figure 4.3	Control block diagram for α control in TCSC.	31
Figure 4.4	The study system: 100 MW Wind farm connected to infinity bus through two parallel transmission lines.	33
Figure 4.5	Inner current control loop for rotor side converter of DFIG.	34
Figure 4.6	Nyquist plots for different compensation levels, RSC: $K_p = 0.6$, $K_i = 8$.	36

Figure 4.7	Bode plots for different compensation levels, RSC: $K_p = 0.6, K_i = 8$.	36
Figure 4.8	Singular value plots of $1 + Y_{DFIG}Z_{net}$ for each compensation level of different modes; (a) fixed capacitor, (b) constant alpha mode for TCSC, (c) impedance control of TCSC, RSC: $K_P = 0.6, K_i = 8$, TCSC gains: $K_P = 0.53, K_i = 3$.	37
Figure 4.9	Singular value plot of $1 + Y_{DFIG}Z_{net}$ for different compensation levels of TCSC at steady-state, RSC: $K_P = 0.6, K_i = 8$, TCSC gains: $K_P = 0.53, K_i = 3$.	38
Figure 4.10	Singular value plot of $1 + Y_{DFIG}Z_{net}$ for different K_p, K_i of TCSC for 50% compensation level at steady-state, RSC: $K_P = 0.6, K_i = 8$.	39
Figure 4.11	Singular value plot of $1 + Y_{DFIG}Z_{net}$ for different K_p, K_i of RSC for 50% compensation level at steady-state, TCSC: $K_P = 0.32, K_i = 1.84$.	40
Figure 4.12	Simulation results for different K_p, K_i of TCSC for 50% compensation level at steady-state, RSC gains: $K_P = 0.6, K_i = 8$.	41
Figure 4.13	Simulation results for comparison of reference impedance and TCSC measured impedance for different K_p, K_i of TCSC for 50% compensation level at steady-state, RSC gains: $K_P = 0.6, K_i = 8$.	41
Figure 4.14	Simulation results for different compensation of TCSC, RSC: $K_P = 0.6, K_i = 8$, TCSC gains: $K_P = 0.53, K_i = 3$.	42
Figure 4.15	Simulation results for different K_p, K_i of DFIG RSC for 50% compensation level at steady-state, TCSC: $K_P = 0.32, K_i = 1.84$.	43
Figure 4.16	Simulation results for comparison of reference impedance and TCSC measured impedance for different K_p, K_i of DFIG RSC for 50% compensation level at steady-state, TCSC: $K_P = 0.53, K_i = 3$.	43
Figure 4.17	Simulation results for different compensation level of fixed capacitor, $X_L = 0.5(p.u.)$, RSC: $K_P = 0.6, K_i = 8$.	44
Figure 4.18	Results of comparison between fixed capacitor and TCSC in 70% compensation of the line reactance, RSC: $K_P = 0.6, K_i = 8$, TCSC: $K_P = 0.16, K_i = 0.92$.	45
Figure 5.1	The study system.	51
Figure 5.2	Basic configuration of PV system.	51
Figure 5.3	Simplified PV model with different combinations, (a) LCL filter, (b) L filter	52
Figure 5.4	Basic control of a single-phase PV.	53
Figure 5.5	Conversion from abc to pnz and back to abc for an induction machine.	56
Figure 5.6	(a) Model of microgrid with PV in phase a , (b) model of microgrid in phase b and c	56

Figure 5.7	Simulation results of torque and rotor speed due to a step change in mechanical torque (from 28 N.M to 23 N.M).	58
Figure 5.8	Simulation results of the IM stator current, stator voltage and PV current due to a step change in mechanical torque (from 28 N.M to 23 N.M).	59
Figure 5.9	Simulation results for the effect of irradiance change.	61
Figure 5.10	The dominant modes (120 Hz, and the voltage stability mode) by increasing the line length.	62
Figure 5.11	Stator voltage when the grid line length increases from 3 km to 30 km, Simulation results were produced by Matlab/SimPowerSystems.	63
Figure 5.12	RMS stator voltage when the grid line length increases from 3 km to 30 km.	63
Figure 5.13	Simpowersystems simulation results for the effect of grid line length increase, (a) torque (b) rotating speed (c) instantaneous current from PV.	64
Figure 6.1	Test system.	67
Figure 6.2	Step by step procedure to derive the ARMA model for load and PV.	70
Figure 6.3	Optimization procedure for real-time digital simulation of the microgrid.	73
Figure 6.4	Equivalent model of a voltage source converter connected to ac source.	75
Figure 6.5	Power control strategy of the inverter.	77
Figure 6.6	General structure of implementation of the proposed algorithm.	79
Figure 6.7	Three months real data captured by PV for SEEDS project.	79
Figure 6.8	Prediction of PV power by ARMA model for different hours ahead.	80
Figure 6.9	Power generation from each DG.	81
Figure 6.10	Total dynamic power contribution in the microgrid with and without battery.	81
Figure 6.11	Battery power and energy stored in the battery.	82
Figure 6.12	Effect of battery size on microgrid total power.	82
Figure 6.13	Comparison between 5 MWh and 10 MWh battery for total microgrid power.	82
Figure 6.14	RT-LAB performance in tracking the reference battery power.	83
Figure 6.15	Battery measurements and commands in RT-LAB.	84
Figure 7.1	Control diagram of the inverter.	87

Figure 7.2	Single line diagram of the microgrid.	88
Figure 7.3	Schematic diagram of the VSC model.	89
Figure 7.4	PPL model.	91
Figure 7.5	Capacitor current control (limit based control).	91
Figure 7.6	PSCAD model of the microgrid.	93
Figure 7.7	PPL power with limit based control.	93
Figure 7.8	Passive control of the inverter, (a) angular frequency of the system (b) system voltage (c) active power from the inverter (d) active power from synchronous generator.	94
Figure 7.9	Active control of the inverter with centralized control compared to passive control, (a) angular frequency of the system (b) system voltage (c) active power from the inverter (d) active power from the synchronous generator.	95
Figure 7.10	Angular frequency and the voltage of the system for different R_f and R_v .	96
Figure 7.11	Power output from the inverter for lower R_f and R_v .	97
Figure 7.12	Active control of the inverter with decentralized control compared to passive control, (a) angular frequency of the system (b) system voltage (c) active power from the inverter (d) active power from the synchronous generator.	97
Figure 7.13	PPL power with limit based control.	98
Figure 7.14	Effect of increased power limit in active control of the inverter with decentralized control, (a) angular frequency of the system (b) system voltage.	99
Figure 7.15	Repetitive PPL.	99
Figure 7.16	Active control of the inverter with decentralized control compared to passive control for repetitive PPL, (a) angular frequency of the system (b) system voltage.	100
Figure 8.1	Microgrid topology.	102
Figure 8.2	HIL testbed setup.	103
Figure 8.3	Hardware-in-the-loop simulation of the battery system.	104
Figure 8.4	Control of the battery inverter.	104
Figure 8.5	Upper level control considering SOC.	105
Figure 8.6	Coordinated control of a battery and a PV.	105

Figure 8.7	Reference active power change for a battery connected to the microgrid.	106
Figure 8.8	Coordinated control of battery and PV.	106
Figure 8.9	Coordinated control of battery and PV considering SOC limits.	107
Figure 8.10	Measured voltage and current profiles of a single battery cell.	108
Figure 8.11	Voltage and current profiles of a battery cell.	108
Figure 8.12	Energy profile of the battery cell.	108
Figure 8.13	Battery cell voltage profile for calculation of internal resistance.	108
Figure 8.14	Resistance calculation circuit.	109
Figure 8.15	Real-time digital simulation setup using RT-Lab.	110
Figure 8.16	System under investigation for simulation in RT-LAB, $L_a = 10e - 3$, $L_b = 20e - 3$, $C_f = 1e - 6$, $C_{dc} = 10e - 3$.	110
Figure 8.17	The MPPT structure for single phase PV in RT-LAB.	111
Figure 8.18	Error signal description based on I-V characteristic of PV.	112
Figure 8.19	The PR controller structure for single phase PV.	112
Figure 8.20	Irradiance change for PV in order to verify the stable operation.	113
Figure 8.21	PV responses due to the irradiance change composed of ramp and step changes.	114
Figure 8.22	Comparison of reference current and measured current of the PV.	114
Figure 8.23	PV response to the ramp change in irradiance.	115
Figure 8.24	PV response to the step change in irradiance.	115
Figure 8.25	Chroma setup.	115
Figure 8.26	Measured irradiance by Chroma and PV output power.	116
Figure 8.27	Results of the simulation with changing irradiance.	116
Figure 8.28	Simulation results from opmonitor block.	117

ABSTRACT

The objective of this dissertation is to carry out dynamic modeling, analysis and control of power systems with Renewable Energy Sources (RES) such as: Photovoltaic (PV) power sources and wind farms. The dissertation work is mainly focused on microgrid since it plays a major role in modern power systems and tend to have higher renewable power penetration. Two main theoretical concepts, dynamic phasor and impedance modeling have been adopted to model and analyze the power systems/microgrids with RES. The initial state calculation which is essential for small signal analysis of a system is carried out as the first step of the dissertation work. Dynamic phasor and impedance modeling techniques have been utilized to model and analyze power systems/microgrids as the second phase of the work. This part consists of two main studies. First case investigates the impedance modeling of Thyristor Controller Series Capacitor (TCSC) for sub-synchronous resonance (SSR) analysis where a wind farm is connected to a power system through series compensated line. Second case utilizes the dynamic phasor concept to model a microgrid in unbalanced condition. Here the unbalance is caused by a single phase PV connected to the microgrid. Third Phase of the dissertation work includes upper level control of the microgrid. Here prediction and optimization control for a microgrid with a wind farm, a PV system, an energy storage system and loads is evaluated. The last part of the dissertation work focuses on real time modeling and hardware in loop simulation test bed for microgrid applications.

This dissertation has led to four journal papers (three accepted, one submitted) and five conference papers.

CHAPTER 1

INTRODUCTION

1.1 Background

Generating electricity from clean and environmental friendly resources is the worldwide trend to develop the future power grid. The government's interest in promoting renewable energy by introducing renewable energy credit and the implementation of the carbon tax in some countries promotes rapid development of renewable energy in the world. The wind power and solar power can be considered as most promising and fastest growing renewable energy sources due to their low generation cost and the minimum environmental impact. Among these, wind power accounted for 42 % of all new electrical capacity added to the United States electrical system in 2008 [1] however, it is still a relatively small fraction of the total capacity in the USA. Wind power has the potential to reach 25 % of U.S. electricity capacity by 2050 [1]. Even though Renewable Energy Sources (RES) play a major role in modern power grid, due to intermittent nature, operational implications will occur. Hence it is essential to study the impact of renewable energy sources on the power system.

In modern power system, the microgrid concept has received much attention, due to its reliability, efficiency and low operation cost. Architecture of the microgrid can be explained in two levels, component level and the management level (control level). The microgrid is in fact a sub-part of a power distribution system. It consists of Distributed Energy Resources (DERs) and loads. DERs include Distributed Generation (DG) units and Distributed Storage (DS) units. Loads include residential type loads, commercial type loads and industrial parks. Microgrid is connected to the utility grid through Point of Common Coupling (PCC) which is located at the low voltage bus

of the substation transformer. DG units can be sub-categorized based on their interface with the Microgrid:

- Conventional DG units with rotating machines
- DG units with power electronic converters

Microgrid control level architecture has three hierarchical levels as shown in Fig.1.1:

- Distributed Network Operator (DNO)
- Microgrid Central Controller (MCC)
- Local Controller (LC)

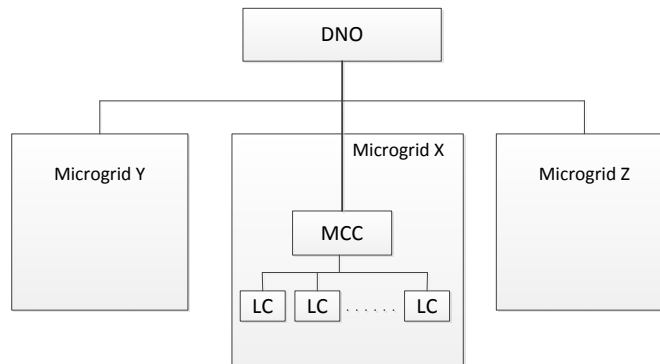


Figure 1.1. Microgrid control level hierarchy.

DNO is responsible for controlling the distributed network, which implies that it controls more than one microgrid. Each microgrid has one MCC which is the main controller of the microgrid. LCs are the lowest level controllers which are associated with each DER. Two control strategies are generally exercised in microgrid control and they are *centralized control* and *decentralized control*.

In centralized control, MCC is responsible for a major part of control. It issues the commands such as power production set points to the DERs and set points for loads to be served and shed. The function of the LCs in centralized control is to follow the MCC instructions. The main disadvantage

of the centralized control is the high cost involved with the fast communication system. This problem can be avoided by occupying decentralized control in power management. Droop control is an example of a decentralized control [2, 3, 4].

There are two possible operational scenarios in a microgrid.

- Grid following operation
- Islanded operation

In grid following operation microgrid follows the voltage and the frequency of the utility grid. Since the voltage and the frequency at the PCC are controlled by the utility grid, control function of dis-patchable DER units will be active/reactive power control. Power set points for DERs will be specified by the utility grid control based on power dispatch strategy.

Islanded operation of a microgrid will be formed when the microgrid is disconnected from the main grid. This can happen due to either pre-planned switching (for maintenance) or unplanned switching incidents (due to faults). Since microgrid is disconnected from the main grid, voltage and frequency of the microgrid should be controlled by itself. Hence, one or more DER units should be assigned to regulate the voltage and the frequency of the system and MCC will be responsible for implementing power dispatch strategy.

1.2 Statement of Problem

With the rapid development of microgrid concept, it is required to identify system stability limits and incorporate these constraints into upper level decision making process. Compared to the conventional three-phase power systems, microgrids are more prone to unbalanced and harmonic operating conditions due to the distribution system nature and the penetration of power electronic devices. In order to address the stability issue, it is vital to model microgrids with renewable energy sources such as wind and PV with power electronic converters.

First, accurate microgrid models which are able to capture unbalance and the harmonics have to be implemented. Here the dynamic phasor approach and the impedance modeling techniques have been utilized as the main tools in the dissertation. Impedance modeling approach is employed to

obtain a linear relationship between voltage and current for each block device. The key advantage of impedance modeling is to convert circuit analysis problems into the format of closed-loop feedback control problems. Therefore, rich linear control system analysis tools such as Bode plots and Nyquist plots can be used to detect instability. To derive accurate impedance models for subsystems under harmonic scenarios, the dynamic phasor concept is adopted to obtain time-varying complex Fourier coefficients for state variables. The dynamic phasor technique can not only facilitate the derivation of impedance models, but also facilitate to build analytical nonlinear system models suitable for small signal analysis. Compared to an instantaneous variable based system where the current and voltage are periodic at steady-state and it is not possible to derive a small signal stability model, dynamic phasor based system has constant value variables at steady-state. Both dynamic phasor and impedance modeling techniques are applied mainly in this research to develop microgrid component models and conduct stability analysis.

Second, proper initial values have to be obtained for small signal analysis. Small signal analysis is adopted for the work presented in this dissertation, to identify the stability limits of a power with renewable energy integration. Here, a sweeping method initialization technique is proposed to calculate the initial states of an unbalance microgrid. The dynamic phasor approach is utilized to capture unbalance components of the system.

Third, identified renewable energy constraints have been incorporated into microgrid system-level decision making procedure. Here a multi-horizon power dispatch algorithm is implemented, utilizing an energy storage system in a microgrid with wind and PV integration.

Fourth, modeling of microgrid components in real time simulator. Real time simulations and the Hardware in Loop (HIL) simulations are the state of the art techniques adopted in today's power system research. Hence the proposed microgrid components are modeled in Real-time simulator and HIL simulations are carried out as demonstrate the validity of the models used above.

1.3 Outline of the Dissertation

The structure of the dissertation is organized as follows.

Chapter 1 provides an introduction of the research problems and their background information.

Chapter 2 gives presents the review of relevant literature and theory. Dynamic phasor approach and the impedance modeling technique concepts are presented in detail.

Chapter 3 presents initialization and steady state calculations for power systems with renewable energy integration. Here two case studies are considered. First one is a power system with wind power integration and the second one is an unbalanced microgrid with single phase PV power integration.

Chapter 4 demonstrates the capability of dynamic phasor and impedance modeling techniques. Here, the well known SSR problem in the series compensated network is analyzed in detail, utilizing above techniques to identify the stability limits of the system. Effect of TSCS compensated line, is analyzed and its limitations and the advantages are identified.

Chapter 5 develops a detailed model for unbalanced microgrid. Single phase PV, induction machine, power factor correction and loads are modeled and several case studies conducted to study the system.

Chapter 6 presents the upper level control of a microgrid. Here, the microgrid consist of a PV system, wind farm, a battery storage and some loads. PV power, wind power and load power are predicted using prediction algorithms and battery storage is dispatched accordingly to optimized the power import of the microgrid.

Chapter 7 investigates the intermittent load applications in microgrid. Here a pulsed power load is implemented as intermittent load and VSC based inverter is proposed to mitigate the system dynamics due to the load behavior.

Chapter 8 develops test bed for microgrid simulations using real time simulations and hardware in loop simulations.

Chapter 9 summarizes the research conclusions.

CHAPTER 2

REVIEW OF RELEVANT LITERATURE AND THEORY

2.1 Dynamic Phasor Based Modeling and Analysis

The rapid evolution of wind energy leads to redefine the grid connection requirements of the wind generation systems. Among these, fault ride-through capability can be considered as one of the major requirement [5, 6, 7, 8, 9]. These new rules require wind farms to withstand steady state voltage unbalance and transient voltage unbalance without disconnecting the wind generators from the grid [6, 7]. Doubly Fed Induction Generator (DFIG) is the most employed wind generator in today's wind power generation [10]. Although the DFIG offers several advantages over fixed-speed generators [8] it is very sensitive to grid voltage disturbances [11]. Unbalanced distribution system will induced unbalanced current in the DFIG creating unequal heating and power loss on the winding as well as torque pulsations in the generator[10, 11, 8, 12, 13, 7]. This may even cause a control system instability in the DFIG [10]. Hence these issues should be addressed in the control architecture of the DFIG.

The dq based time domain simulations provide much accurate time response of a three phase balanced system. However the major problem involved with dq model is that negative sequence components in abc are converted to 120 Hz ac variables in dq. Hence dq based models offer no capability to perform small signal analysis under unbalanced conditions. On the other hand, dynamic phasor based modeling [14] has the capability of both accurate time-domains simulation and small signal analysis [15, 14, 16, 17].

2.1.1 Dynamic Phasor Concept

The Dynamic phasor concept is defined based on the Fourier series representation of a complex time domain waveform $x(\tau)$ in the interval $\tau \in (\tau - T, t)$ [14],

$$x(\tau) = \sum_{k=-\infty}^{\infty} X_k(t).e^{jk\omega\tau} \quad (2.1)$$

Here $\omega = \frac{2\pi}{T}$ and $X_k(t)$ is the k^{th} complex Fourier coefficient also referred as dynamic phasor. Although these coefficients are functions of time they vary slowly with the time which makes the dynamic phasor representation is a good candidate for small signal models. Dynamic coefficients of a complex time domain waveform $x(\tau)$ can be obtained using the following average operation [14].

$$X_k(t) = \frac{1}{T} \int_{t-T}^t x(\tau)e^{jk\omega\tau} d\tau = \langle x \rangle_k(t); \quad (2.2)$$

A good approximation of the original signal can be achieved by choosing suitable k values. One of the most important properties of dynamic phasor is the relationship between derivative of original signal and the derivative of dynamic coefficient, which can be obtained using (2.1).

$$\left\langle \frac{dx}{dt} \right\rangle_k = \frac{dX_k}{dt} + jk\omega X_k; \quad (2.3)$$

These concepts are applied in subsequent sections of this report for modeling components in microgrid.

2.2 Impedance Modeling

Impedance based models can be utilized to investigate electric system stability and insights. Nyquist stability criterion for impedance model has been widely employed in power electronic based systems to investigate stability and control design [18] .

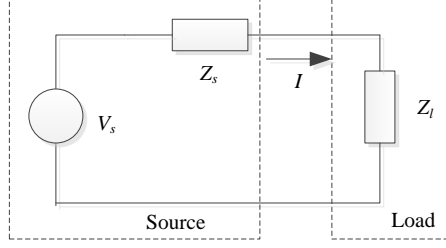


Figure 2.1. Voltage source and a load.

2.2.1 Impedance Based Nyquist Stability Criterion

The current in the system presented Fig.2.1 can be written as,

$$I(s) = \frac{V(s)}{Z_s(s) + Z_l(s)} = \frac{V(s)}{Z_l(s)} \frac{1}{1 + \frac{Z_s(s)}{Z_l(s)}} \quad (2.4)$$

Assuming the system is stable when the load is powered from ideal source, which implies $\frac{V(s)}{Z_l(s)}$ is stable, then $\frac{1}{1 + \frac{Z_s(s)}{Z_l(s)}}$ decides the system stability. In order to system to be stable, the denominator $1 + \frac{Z_s(s)}{Z_l(s)}$ should have all zeros in the open left-half-plane. Based on Nyquist stability criterion, if and only if the number of counterclockwise encirclement around $(-1,0)$ of $\frac{Z_s(s)}{Z_l(s)}$ is equal to the number of the right-half-plane (RHP) poles of $\frac{Z_s(s)}{Z_l(s)}$ then the system will be stable.

2.3 Dynamic Phasor Based Impedance Modeling and Analysis

Power electronics converters which are highly employed in today's microgrid can cause harmonic interaction and resonance in the system [19, 20]. Hence it is essential to analyze the system stability with harmonics. Combining both dynamic phasor approach and impedance model provides substantial advantage for stability analysis in power system since it can be utilized not only to analyze unbalance systems but also to analyze harmonic components.

CHAPTER 3

INITIALIZATION OF SYSTEMS WITH RENEWABLE INTEGRATION

3.1 Introduction

This Chapter presents the research on initialization of a power system with renewable integration. The first section ¹ presents an accurate dynamic model for a DFIG and steady state calculations considering losses inside the wind farm. Initial state calculations for an unbalance system with renewable penetration is presented in next section ². Here the unbalance of the system is caused by a single phase PV integration.

3.2 Analytical Modeling and Initializing of DFIG

Wind power can be considered as one of the most promising and fastest growing renewable energy sources due to its low generation cost and the minimum environmental impact. With the rapid increasing penetration to the system, it is essential to study the impact of wind generation on the power system. Wind forecasting plays a major role in implementing an accurate model to estimate the power generation of a wind farm. Several methods of wind forecasting are presented in [21, 22, 23]. At the same time building an accurate wind farm model is equally important to find the correct power dispatch and initial conditions. Doubly Fed Induction Generator (DFIG) is widely used in wind generation today. A detailed dynamic model of a DFIG is presented in [24]. However, it is logical to consider steady state model of a DFIG for power dispatch. A better approach to calculate steady state operating conditions for DFIG is discussed in [25]. It has considered the power losses due to stator and rotor resistance. Most of the work, including [26, 27, 28] consider

¹This section is based on the work published in North American Power Symposium (NAPS), pp. 1-6. IEEE, 2011. Permission is included in Appendix A.

²This section is based on the work published in Power & Energy Society General Meeting, 2015 IEEE. Permission is included in Appendix A.

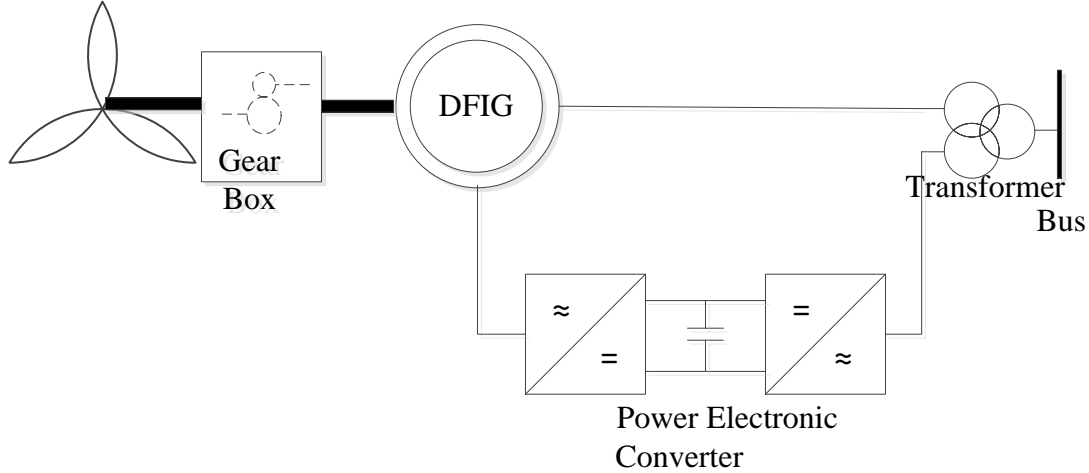


Figure 3.1. Wind turbine and DFIG.

the electrical power output of a DFIG is known for a given wind speed. This can be achieved either by assuming that there is no power loss within the wind farm or by referring to the power curve of the machine provided by the manufacture. If the power loss inside the wind farm is neglected, then the power output of the DFIG is equal to the mechanical power which can be calculated directly using the wind speed. Another method is to obtain the expected power output from the power curve of the machine under the assumption that the power given by the manufacture matches with the actual electrical power output of the machine. But in practice actual electric power will depend on the reactive power injection and the power system parameters. To overcome the above problem a method without those assumptions should be implemented. Then this model can be employed to obtain optimal power flow with wind power penetration.

3.2.1 Steady State Model of a Wind Farm

Steady State model of the wind farm consists of the wind turbine model and the DFIG model. Detailed models are employed in the following subsections. The power losses inside the wind farm are modeled separately.

3.2.1.1 Wind Turbine Model

The system presented in Fig.3.1 consists of a wind turbine with a DFIG. The mechanical power output of the wind turbine can be written as,

$$P_m = \frac{1}{2}\rho AC_p U^3 \quad (3.1)$$

where ρ, A, C_p, U are air density, area covered by the turbine rotor, power coefficient and wind speed.

Power coefficient C_p , depends on the tip speed ratio λ and the pitch angle β [24].

$$\lambda = \frac{V_t}{U} \quad (3.2)$$

where V_t is the tip speed. A wind turbine can be operated in three modes [25].

- Minimum rotor speed
- Maximum power production ($C_{p,max}$)
- Maximum rotor speed

The maximum power production mode operation is assumed in this work. This implies that the wind speed is below the rated speed and the pitch angle of the turbine is zero. Since C_p depends on λ and β , $C_{p,max}$ can be achieved at one specific λ value, which is the optimal value of λ . Therefore (3.2) can be written as,

$$P_m = k_0 U^3 \quad (3.3)$$

where $K_0 = \frac{1}{2}\rho AC_{p,max}$

3.2.1.2 DFIG Model

Equivalent circuit diagram of the DFIG is shown in Fig. 3.2. Since the core loss in a DFIG (Induction Generator) is very low compared to the rotor and the stator copper losses it is neglected

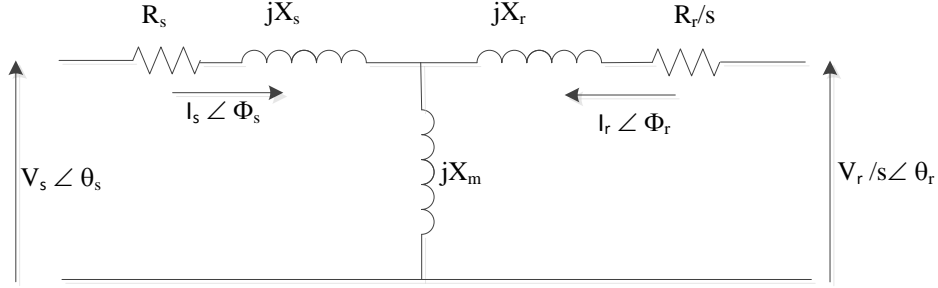


Figure 3.2. Equivalent circuit diagram of DFIG.

from the steady state model. By applying the Kirchhoffs Voltage law to the circuit,

$$V_s \angle \theta_s = -(R_s + j(X_s + X_m))I_s \angle \phi_s + jX_m I_r \angle \phi_r \quad (3.4)$$

$$V_r \angle \theta_r = (R_s + j(X_s + X_m))I_r \angle \phi_r - jX_m I_s \angle \phi_s \quad (3.5)$$

Stator and rotor powers can be calculated as,

$$P_s = V_s I_s \cos(\theta_s - \phi_s) \quad (3.6)$$

$$P_r = -V_r I_r \cos(\theta_r - \phi_r) \quad (3.7)$$

For the simplicity of steady state calculations, it is assumed that the reactive power is transferred through the stator only. This is achievable since reactive power through the rotor can be controlled in the grid side converter. Consequently the total reactive power of the DFIG can be expressed as,

$$Q = V_s I_s \sin(\theta_s - \phi_s) \quad (3.8)$$

3.2.1.3 Power Losses Inside the Wind Farm

Power losses inside the wind farm can be categorized as follows.

- Generator power losses
- Gear box power losses

- Converter power losses

Total power loss is given by

$$P_{Loss} = P_{Gen, Loss} + P_{GB, Loss} + P_{Conv, Loss} \quad (3.9)$$

3.2.2 Steady State Operating Conditions

The above expressions can be summarized as,

$$f1 = V_s \cos(\theta_s) + R_s I_s \cos(\phi_s) - (X_s + X_m) I_s \sin(\phi_s) + X_m I_r \sin(\phi_r) = 0 \quad (3.10)$$

$$f2 = V_s \sin(\theta_s) - R_s I_s \sin(\phi_s) + (X_s + X_m) I_s \cos(\phi_s) - X_m I_r \cos(\phi_r) = 0 \quad (3.11)$$

$$f3 = V_r \cos(\theta_r) - s X_m I_s \sin(\phi_s) - R_r I_r \cos(\phi_r) + s(X_s + X_m) I_r \sin(\phi_r) = 0 \quad (3.12)$$

$$f4 = V_r \sin(\theta_r) + s X_m I_s \cos(\phi_s) - R_r I_r \sin(\phi_r) - s(X_s + X_m) I_r \cos(\phi_r) = 0 \quad (3.13)$$

$$f5 = P - V_s I_s \cos(\theta_s - \phi_s) + V_r I_r \cos(\theta_r - \phi_r) = 0 \quad (3.14)$$

$$f6 = Q - V_s I_s \sin(\theta_s - \phi_s) = 0 \quad (3.15)$$

$$f7 = P + I_s^2 R_s + I_r^2 R_r + P_{GB, Loss} - k(1 - s)^3 = 0 \quad (3.16)$$

If the generator power outputs, P, Q are known for a given wind speed, then the steady state operating conditions can be achieved solving the above equations employing Newton-Raphson method. An iterative method is proposed to combine optimal power flow to obtain accurate power outputs of the wind farm. The proposed algorithm is presented in Fig.3.3 and can be described as follows:

1. Set the initial values for P and Q . For a given wind speed the mechanical power can be calculated and it can be set as the initial value of P because closer the initial value (set value) to the true value (actual power) is faster the algorithm converges.
2. Since the initial P and Q values are set, the DFIG can be considered as a PQ bus in the optimal power flow simulation. It is assumed that DFIG is dispatching the maximum possible power

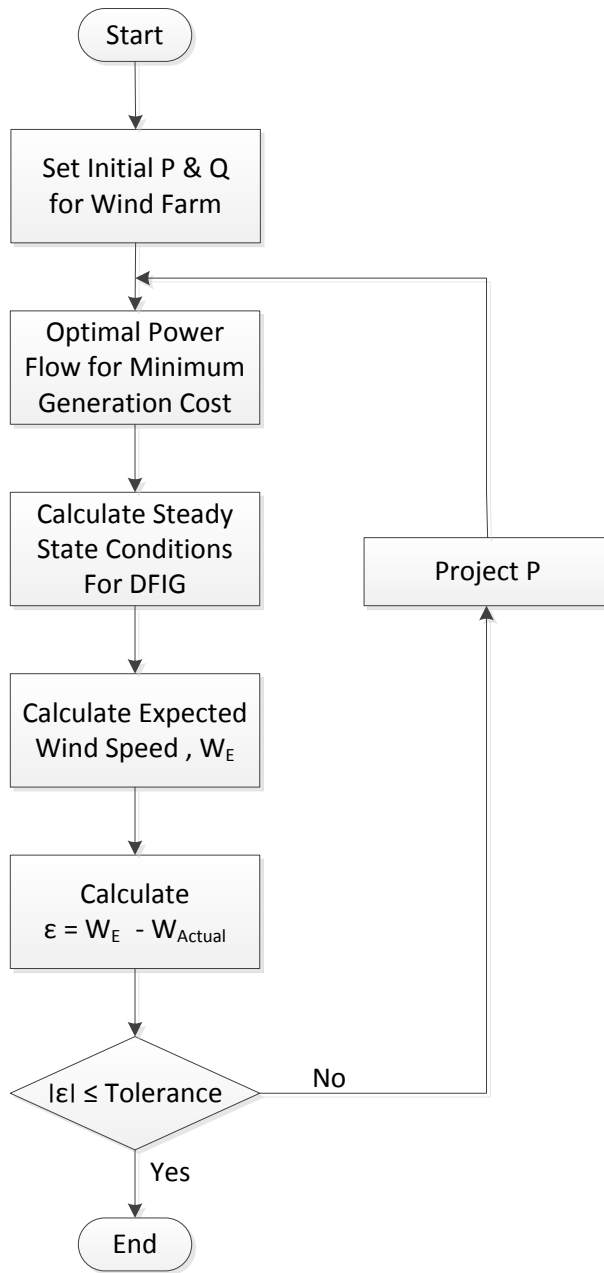


Figure 3.3. Iterative model for optimal power flow and steady state calculations.

to the system (this is reasonable because there is no fuel cost involved with wind generation). Voltage magnitude and angle of each bus in the system will be calculated during the optimal power flow. Hence the magnitude and the angle of stator voltage of the DFIG can be obtained.

3. Since P, Q, V_s and θ_s are known NR method can be used to find steady state conditions of DFIG.
4. Wind speed which is related to set P and Q can be calculated using the steady state variable, slip.
5. Error between the calculated wind speed and the actual wind speed can be found.
6. P can be adjusted according to the calculated error.
7. Steps 2-6 will be repeated until the error becomes less than the given tolerance. More accurate results can be obtained by reducing the tolerance. However it will take more time (number of iterations) to converge.
8. Final steady state operating conditions and the economic dispatch pattern can be used as the final result.

3.3 Sweeping Method Implementation for Unbalanced Network

Power system dynamic studies will be more complicated when the unbalance sources exist. Single phase PV is such kind of source which will introduce unbalance components to the distributed power system. In order to carry out more accurate simulations, the initial state calculations and load flow studies needed to be conducted more carefully [29]. This section presents a methodology to initialize a dynamic phasor based distribution system consist of single-phase PV and three-phase induction machine and loads. In order to carry out small signal analysis of a system, the system states should have a constant steady state value. Dynamic phasor models are capable of providing constant steady state values under unbalanced conditions[30, 31]. Hence the dynamic phasor model of the system presented in Fig. 3.4 is utilized to achieve the above objective. A proper initialization

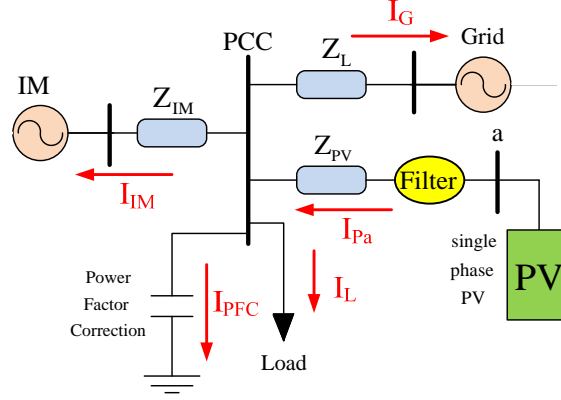


Figure 3.4. The system under study.

method has to be employed to obtain accurate initial values for this model. Following challenges needed to be addressed in this initialization method.

- Should be capable of providing an efficient computing method for unbalanced radial distribution network.
- Unbalance conditions needed be considered in the induction machine model.

Both these challengers are tackled in the work presented in this subsection. A sweeping technique [32] is utilized to address the first challenge while dynamic phasor based induction machine model is utilized to tackle the second challenge.

3.3.1 The Study System

The power system which is used in this study is an unbalanced radial distribution system, including an induction machine, Power Factor Correction (PFC) capacitors, a load and a single-phase PV. Fig. 3.4 shows the single-phase circuit diagram. All the elements are connected to the point of common coupling (PCC). Parameters of the system are given in the appendix. The single-phase PV is composed of an LCL filter for filtering out the unwanted harmonics. In the single line diagram shown in Fig. 3.4, all the lines except for the PV are three phase balanced, and the PV line is a single phase line.

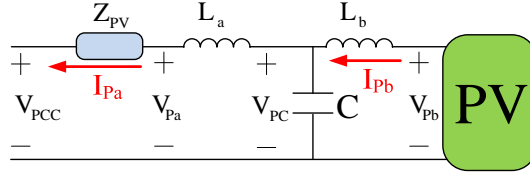


Figure 3.5. The connection of PV and an LCL filter to the grid.

Most distribution systems are radial which enables the calculation of load flow starting from one point and moving forward/backward to the other points of the system. Usually, distribution network matrices are ill-conditioned with sparse bus admittance matrix. This can be justified by excessive number of nodes in systems compared with a number of branches. Newton-Raphson or fast decoupled methods need to store the network admittance matrix and require computing power. On the other hand, sweeping method does not need to store the admittance matrix. In addition, fast decoupling methods can not apply when the ratio of $\frac{R_{line}}{X_{line}}$ is high. For a system in Fig. 3.4, sweeping method is more suitable.

3.3.2 Sweeping Method Procedure

The sweeping method starts from the initial guess of the PCC voltage. From the PCC voltage, and Newton-Raphson method, stator currents of the induction machine can be found. The line impedance Z_{L1} can be incorporated into the IM's stator impedance. Detailed description of the Newton-Raphson method for IM in unbalanced conditions is given in the next section. At the same time, with the first guess of PCC voltage, the PFC current and the load current will be calculated. The PV current will be also calculated based on reference PV power and initial PCC voltage using the Newton-Raphson method. Fig. 3.5 gives the topology of the PV system where an LCL filter connected PV's converter to the grid. The PV panel and the interfacing converter have been aggregated as a block in Fig. 3.5 where the output is a sinusoidal AC voltage. Therefore, the PV and its converter are modeled as a voltage source, V_{Pb} .

The following equations (in phasor domain) can be derived for the PV model presented in Fig. 3.5,

$$\begin{cases} V_{PCC} = I_{Pa}(Z_{PV} + j\omega L_a) + V_{PC} \\ V_{PC} = V_{Pb} - j\omega L_b I_{Pb} \\ I_{Pa} = I_{Pb} - j\omega C V_{PC} \\ P_{\text{ref_PV}} = \Re(V_{Pb} I_{Pb}^*) \end{cases} \quad (3.17)$$

The reference PV power will be further expressed by V_{PCC} and I_{Pa} . Since V_{PCC} is known, I_{Pa} can be found from the nonlinear equation using Newton-Raphson method.

Total current to the grid is then calculated by summing the PV current, PFC current, load current and IM currents. It should be noted that, as the PV is single-phase, currents for phase a is different from those of the two other phases. This will create an unbalance in the PCC voltage and the grid current. The grid currents can be expressed as:

$$\begin{aligned} I_{Ga} &= I_{Pa} - I_{IMa} - I_{PFCa} - I_{La} \\ I_{Gb} &= -I_{IMb} - I_{PFCb} - I_{Lb} \\ I_{Gc} &= -I_{IMc} - I_{PFCc} - I_{Lc} \end{aligned} \quad (3.18)$$

Assume that the grid voltage is fixed as V_{Ga}, V_{Gb}, V_{Gc} , the PCC voltage will be updated using the calculated grid currents:

$$V_{PCC}(\text{new}) = V_{Gabc} + I_{Gabc} Z_L \quad (3.19)$$

This new PCC voltage will be used to compute currents again until convergence. The flowchart of the sweeping algorithm is shown in Fig. 3.6.

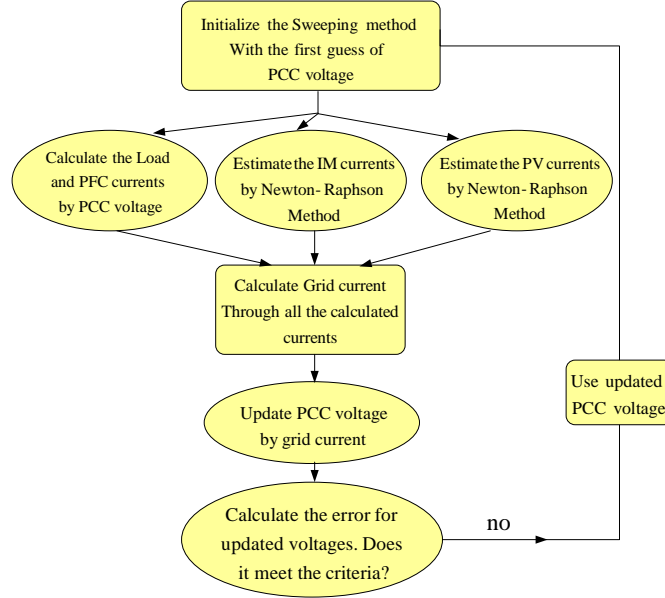


Figure 3.6. Flowchart of the sweeping method.

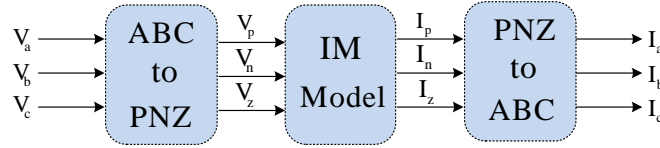


Figure 3.7. Conversion from abc to pnz and back to abc for an induction machine.

3.3.3 Induction Machine Model and Initialization

In this section, the initialization of an induction machine will be presented. The given information is the load torque (T_L) and the PCC voltage. The PCC voltage is treated as the stator voltage of the IM when the line impedance Z_{L1} is aggregated into the stator impedance.

To capture the dynamic behavior of an induction machine under unbalance condition, the dynamic model should include both positive, negative and zero (pnz) sequence components. The pnz dynamic phasor-based dynamic model for unbalanced IM has been developed in [30]. This model will be used in this work. All other elements, e.g., PV, PFC and the line, are all modeled by dynamic phasors in abc phase frame. Therefore, the pnz dynamic phasor-based IM model will be converted to abc dynamic phasor-based model as shown in Fig. 5.5.

In the pnz reference frame, IM model's state variables include the stator and rotor currents: $I_{Ps}, I_{Ns}, I_{Zs}, I_{Pr}, I_{Nr}, I_{Zr}$, respectively. Subscripts P, N, Z define the positive, negative, and zero, respectively where as subscripts s and r defines the stator and rotor signal respectively. Moreover, each signal has a real and imaginary part which will be shown by superscripts r for real and x for imaginary part of the signal. Neglecting the zero sequence components, eight current components ($I_{Ps}^r, I_{Ns}^r, I_{Pr}^r, I_{Nr}^r, I_{Ps}^x, I_{Ns}^x, I_{Pr}^x, I_{Nr}^x$) and three rotor speed components ($\omega_{r0}, \omega_{r2}^r$ and ω_{r2}^x) should be initialized. The inputs of the IM are three-phase voltages of the stator in abc frame. The rotor voltages are considered to be zero. The stator voltages in abc should be converted to the pnz . The basic dynamic model of IM now is extended to pnz reference frame and can be expressed by:

$$V = CI + D \frac{d}{dt} I \quad (3.20)$$

where, $V = [V_{Ps} \ V_{Ns}^* \ 0 \ V_{Pr} \ V_{Nr}^* \ 0]^T$, and $I = [I_{Ps} \ I_{Ns}^* \ 0 \ I_{Pr} \ I_{Nr}^* \ 0]^T$. Matrices C and D then can be formulated as (3.21). Then state-space model can be found:

$$C = \begin{bmatrix} r_s + j\omega_s L_s & 0 & j\omega_s L_m & 0 \\ 0 & r_s - j\omega_s L_s & 0 & -j\omega_s L_m \\ j\omega_s L_m - j\omega_{r0} \frac{P}{2} L_m & -j\omega_{r2} \frac{P}{2} L_m & r_r + j\omega_s L_r - j\omega_{r0} \frac{P}{2} L_r & -j\omega_{r2} \frac{P}{2} L_r \\ -j\omega_{r2}^* \frac{P}{2} L_m & -j\omega_s L_m - j\omega_{r0} \frac{P}{2} L_m & -j\omega_{r2}^* \frac{P}{2} L_r & r_r - j\omega_s L_r - j\omega_{r0} \frac{P}{2} L_r \end{bmatrix}$$

$$D = \begin{bmatrix} L_s & 0 & L_m & 0 \\ 0 & L_s & 0 & L_m \\ L_m & 0 & L_r & 0 \\ 0 & L_m & 0 & L_r \end{bmatrix} \quad (3.21)$$

$$\begin{cases} \dot{I} = F_x \\ F_x = D^{-1}CI + D^{-1}V \end{cases} \quad (3.22)$$

where F_x is the vector of the derivative of induction machine currents, including real and imaginary parts. Separating real and imaginary parts of F_x , eight equations of real and imaginary derivatives of IM currents will be achieved. Three equations of rotor speed in fundamental harmonic and second harmonic, presented in (5.9), can be added to shape the entire model in state space:

$$\begin{aligned}
\omega_{r0} &= \frac{1}{J}(PL_m \Im(I_{P_s} I_{P_r}^* + I_{N_s}^* I_{N_r}) - T_L - B\omega_{r0}) \\
\omega_{r2}^r &= \frac{1}{J} \Re(PL_m \frac{1}{2j}(I_{P_s} I_{N_r} - I_{N_s} I_{P_r}) - (B + j2J\omega_s)\omega_{r2}) \\
\omega_{r2}^i &= \frac{1}{J} \Im(PL_m \frac{1}{2j}(I_{P_s} I_{N_r} - I_{N_s} I_{P_r}) - (B + j2J\omega_s)\omega_{r2})
\end{aligned} \tag{3.23}$$

where, P is the number poles, J is the inertia constant, B is the damping factor, \Re is the real part and \Im is the imaginary part. Now, combining (5.9) and (5.8), an entire dynamic model of IM is obtained $\dot{X} = f(X)$,

where $X = [I_{P_s}^r \ I_{N_s}^r \ I_{P_r}^r \ I_{N_r}^r \ I_{P_s}^x \ I_{N_s}^x \ I_{P_r}^x \ I_{N_r}^x \ \omega_{r0} \ \omega_{r2}^r \ \omega_{r2}^i]^T$, and $f(X)$ is the derivative of X .

The initialization will find the solution for $f(X) = 0$. Newton-Raphson method starts with calculating the jacobian of $f(x)$. In the first step, initial guesses for the induction machine will be applied. Here, the initial guesses for all the parameters are set to zero except $\omega_{r0} = 188$, $I_{P_s}^r = 1$, and $I_{P_r}^r = 1$. The Newton's approach conducts the following iteration:

$$X_k = X_{k-1} - \left(\frac{\partial f}{\partial X} \right)^{-1} \Bigg|_{X_{k-1}} f(X_{k-1}) \tag{3.24}$$

where X_{k-1} is the initial value in the last step. This iteration process will be continued till the error value is less than 0.001. After the error is converged, the initial parameters of the induction machine are obtained which will be used in sweeping method that was described in the previous section.

3.3.4 Case Study

The model has been built in Matlab. The sweeping method along with two embedded Newton's approaches to find IM and PV initials have been applied. The IM model is built in pnz reference

frame, then it has been converted to *abc* frame, the grid is then modeled in *abc* and the single-phase PV is then added to the system in phase *a*. Two case studies have been conducted to examine the convergence of the algorithm for a balanced system (without PV) and an unbalanced system (with 2 kW PV). Moreover, dynamic simulations have also been carried out to demonstrate the system performance after a sudden torque change in the unbalanced system.

3.3.4.1 Case 1: Balanced System

In this case, the PV has been removed from the model and three-phase balanced voltages have been applied to the system. Convergence of the algorithm for the balanced case has been illustrated in Fig. 3.8 to Fig. 3.10. As it can be seen, the sweeping method for the entire system converges after five iterations which verifies the robustness of the algorithm in balanced condition.

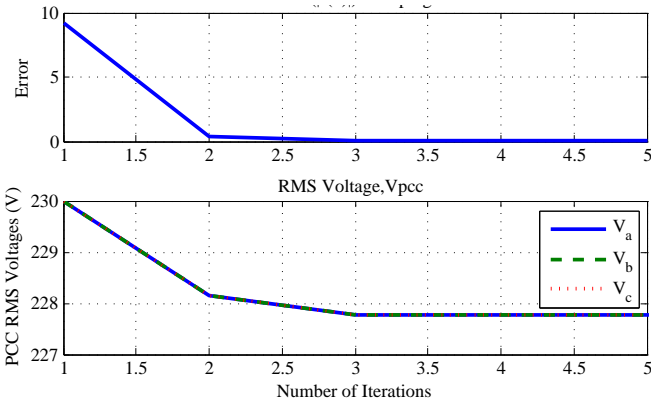


Figure 3.8. PCC voltages in balanced case.

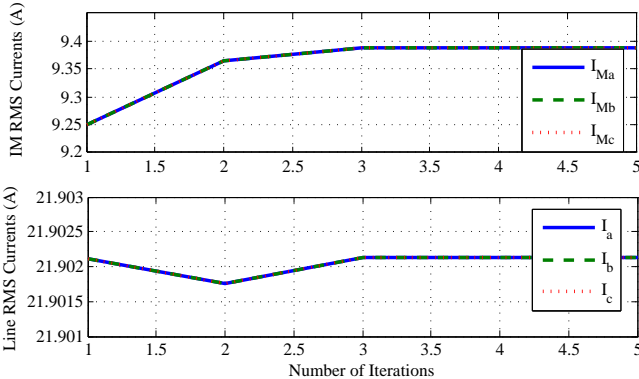


Figure 3.9. Grid current and IM current.

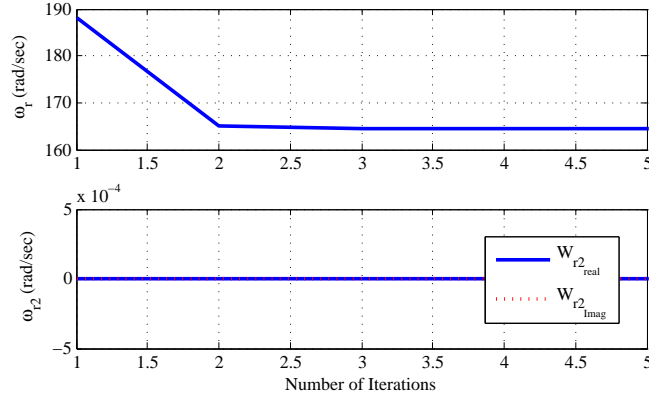


Figure 3.10. Rotor speeds in balanced case.

The results of the line and IM RMS currents for the balanced case have been illustrated in Fig. 3.9. As expected, magnitudes for all three phases are the same for the balanced case. Results for rotor speed is illustrated in Fig. 3.10 which verifies the rotor speed does not have any second harmonic component due to balanced operation.

3.3.4.2 Case 2: Unbalanced System

In this case, the system is faced with unbalance due to the connection of a single-phase PV at phase a . The power rating of the PV has been set to 2 kW. The iterative results for the unbalanced system has been illustrated in Fig. 3.11 to Fig. 3.13. As it can be seen, the sweeping method in this case takes seven iterations to converge.

Fig. 3.12 shows that line current at phase a is less than the other two phases which is caused by operation of a single-phase PV at phase a . Furthermore, Fig. 3.13 shows the rotor speed and its second harmonic components for unbalanced case. As it can be observed, by connecting the single phase PV, the second harmonic components of the PV will have a value and the sweeping method can obtain the initial values for these components as well.

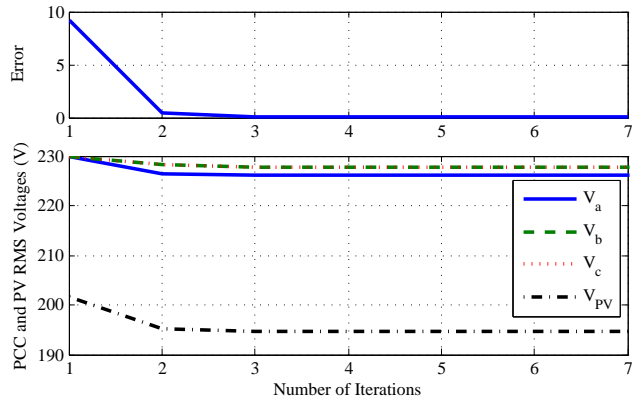


Figure 3.11. Simulation results of sweeping method for voltages in unbalanced case.

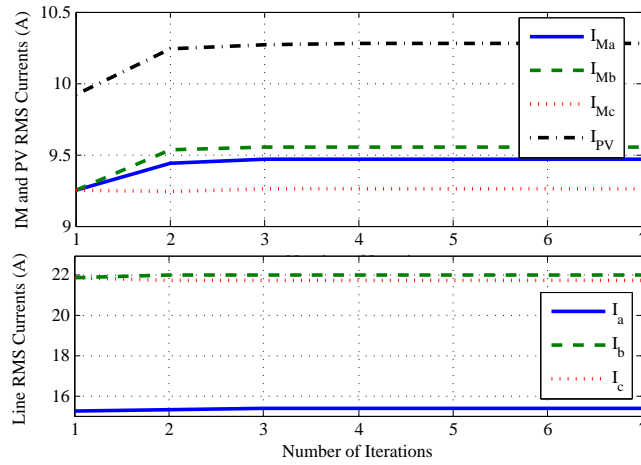


Figure 3.12. Simulation results of sweeping method for currents in unbalanced case.

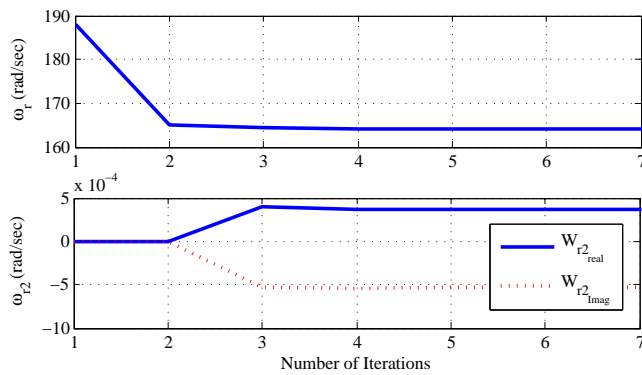


Figure 3.13. Simulation results of sweeping method for rotor speed in unbalanced case.

Table 3.1. Parameters of the induction generator

Total capacity	5.5 kVA
Nominal voltage	400V
Frequency	60Hz
R_s	2.52 Ω
R_r	2.67 Ω
X_{ls}	3.39 Ω
X_{lr}	3.39 Ω
X_M	197 Ω
J	0.486kg.m ²
P (poles)	4

Table 3.2. Data of the lines in network

Line No	Line Type	Z (Ω/km)	Length(m)
1	Grid Line (3-phase)	0.284+j0.0825	105
2	IM Line (3-phase)	0.497+j0.0861	105
3	PV Line (single-phase)	0.0144+j0.0064	30

CHAPTER 4

DYNAMIC PHASOR BASED SSR ANALYSIS OF DFIGS

4.1 Introduction

The Utility industry has been concerned with SSR issues in Type 3 wind generator with series compensated network [33]. There have been published a series of papers on this topic employing eigenvalue based analysis [34, 35, 36] and frequency domain impedance based analysis [37, 38, 39]. Compared to eigenvalue based analysis where an entire system's dynamic state matrix, eigenvalues and participation factors will be examined, impedance modeling approach is a frequency domain approach. Impedance modeling also provides a modular approach. We can develop an impedance model for a doubly fed induction generator (DFIG) and an impedance model for a transmission line. To examine the impact of line parameters on SSR, we only need to concern the line impedance model. Therefore, impedance modeling approach can provide more insights into impact factors of resonance stability.

This chapter ¹ will examine the effect of TCSC on SSR. It has been claimed in the literature that TCSC is neutral to SSR [40]. In addition, Varma *et al* have published experimental results to demonstrate that TCSC can successfully suppress SSR in Type 1 wind generator systems [41]. The purpose of this chapter is to provide a theoretic base to explain why TCSC has such capability and the approach we adopt is frequency domain impedance modeling approach.

To the best of the author's knowledge, TCSC is one of the power system components that is most difficult to model due to its low-order harmonic components in inductor currents and capacitor voltages. In the literature, other than dynamic phasor based models, TCSC's small signal model can be developed by two approaches. In the first approach [42], frequency responses in Bode

¹This chapter was published in Sustainable Energy, IEEE Transactions on 6, no. 1 (2015): 179-187. Permission is included in Appendix A.

plots are obtained from small perturbation of time-domain simulation models. From these Bode plots, transfer functions are tuned to match the Bode plots. Such method is also called frequency scanning and has been employed to develop HVDC models [43] and in SSR studies [44]. In the second approach, TCSC's steady-state model is derived [45] based on Fourier analysis and can be expressed in terms of the firing angle. This model can be used to develop an approximate impedance model. Both approaches cannot provide an accurate frequency domain impedance model.

Dynamic phasor based modeling technique can include harmonic and unbalance effects in analytical models and has been employed in the past for time-domain simulation and small signal analysis [46]. The work presented here provides one step further. The contribution of this work is to employ dynamic phasor technique in deriving accurate impedance models for TCSC with constant firing angle control and constant impedance control. With the derived impedance models, Nyquist-stability-criterion can be applied to detect SSR stability in systems with TCSC. This chapter successfully demonstrates TCSC's capability in avoiding SSR in Type 3 wind generator interconnection systems. In addition, sensitivity of TCSC's impedance control parameters on SSR stability is also investigated. The analytical results obtained through impedance models are validated by detail based time-domain simulation in Matlab/SimPowerSystems.

4.2 Impedance Model of TCSC

With the assumption of a sinusoidal imposed voltage, the fundamental frequency current through a Thyristor Controlled Reactor (TCR) can be obtained and further the inductance can be expressed as [47]:

$$L(\alpha) = L \frac{\pi}{\pi - 2\alpha - \sin 2\alpha} \quad (4.1)$$

where α is the firing angle measured from the zero crossing of the line current.

Therefore, a simple TCSC impedance model per-phase can be expressed as:

$$Z_{TCSC}(s) = \frac{sL(\alpha)}{1 + s^2L(\alpha)C} \quad (4.2)$$

The assumption of undistorted voltage is not the case in TCSC. Undistorted line current assumption is usually used for TCSC. Jalali *et al* [45] derived a complex steady-state reactance model for a TCSC. To account for dynamics and develop frequency domain impedance model, we start from the state-space model of fundamental frequency component developed in [46]. The circuit

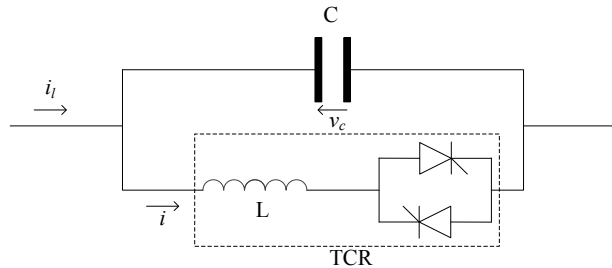


Figure 4.1. TCSC circuit diagram.

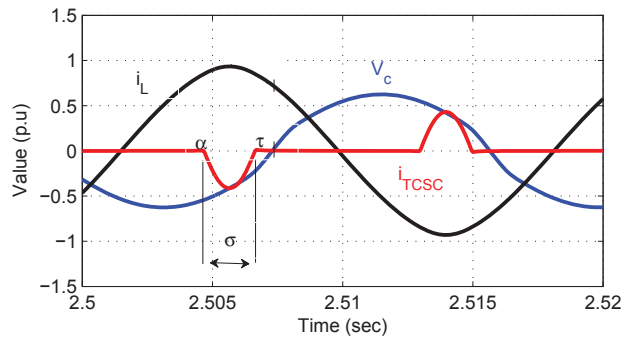


Figure 4.2. TCSC waveforms.

diagram of a TCSC is presented in Fig .4.1. This circuit consist of a capacitor in parallel with Thyristor Controlled Reactor (TCR). The net impedance of the TCSC can be controlled via controlling the fire angle α of the TCR. Fig. 4.2 shows the steady state voltage and current waveforms of the TCSC. The Thyristor is switched on α angle after the zero crossing of the line current and will be conducting till τ . Conduction angle is defined as, $\sigma = \tau - \alpha$ and it can be assumed that the angle σ is symmetrical with respect to the peak value of the line current to simplify model development. This assumption is employed in [46]. The dynamic phasor model for the fundamental voltage and current phasors can be developed as follows.

$$\begin{aligned}
\underbrace{\begin{bmatrix} \dot{V}_1^R \\ \dot{V}_1^I \\ \dot{I}_1^R \\ \dot{I}_1^I \end{bmatrix}}_{\dot{X}} &= \underbrace{\begin{bmatrix} 0 & -\omega_s & -\frac{1}{C} & 0 \\ \omega_s & 0 & 0 & -\frac{1}{C} \\ \frac{1}{\pi L}[\sigma + \sin(\sigma)\cos(2(\xi + \phi))] & \frac{1}{\pi L}\sin(\sigma)\sin(2(\xi + \phi)) & 0 & -\omega_s \\ \frac{1}{\pi L}\sin(\sigma)\sin(2(\xi + \phi)) & \frac{1}{\pi L}[\sigma - \sin(\sigma)\cos(2(\xi + \phi))] & \omega_s & 0 \end{bmatrix}}_A \underbrace{\begin{bmatrix} V_1^R \\ V_1^I \\ I_1^R \\ I_1^I \end{bmatrix}}_X + \underbrace{\begin{bmatrix} \frac{1}{C} & 0 \\ 0 & \frac{1}{C} \\ 0 & 0 \\ 0 & 0 \end{bmatrix}}_B \underbrace{\begin{bmatrix} I_{l1}^R \\ I_{l1}^I \end{bmatrix}}_U \\
& \tag{4.3}
\end{aligned}$$

$$\begin{aligned}
\underbrace{\begin{bmatrix} V_1^R \\ V_1^I \end{bmatrix}}_Y &= \underbrace{\begin{bmatrix} 1 & 0 & 0 & 0 \\ 0 & 1 & 0 & 0 \end{bmatrix}}_C \underbrace{\begin{bmatrix} V_1^R \\ V_1^I \\ I_1^R \\ I_1^I \end{bmatrix}}_X \\
& \tag{4.4}
\end{aligned}$$

The dynamics of the TCSC are as follows:

$$\begin{cases} C \frac{dv_c}{dt} = i_l - i \\ L \frac{di}{dt} = qv_c \end{cases} \tag{4.5}$$

where i_l is the line current v_c is the voltage across the capacitor, i is the current through the TCR and q is the switching function which represents the TCR switching. $q = 1$ when one of the thyristors is conducting and $q = 0$ when both are not conducting. Fundamental dynamic phasor representation of (4.5) can be obtained using the dynamic phasor concept [46].

$$\begin{cases} C \frac{dV_1}{dt} = I_{l1} - I_1 - j\omega_s CV_1 \\ L \frac{dI_1}{dt} = \langle qv_c \rangle_1 - j\omega_s LI_1 \end{cases} \tag{4.6}$$

where subscript "1" denotes phasors related to the fundamental frequency. These phasors are complex variables and can be expressed by the real part and the imaginary part.

$$\begin{cases} V_1 = V_1^R - jV_1^I \\ I_1 = I_1^R - jI_1^I \\ I_{l1} = I_{l1}^R - jI_{l1}^I \end{cases} \quad (4.7)$$

When a TCSC is operating in capacitive region, the fundamental component gives a good approximation for the capacitor voltage, v_c [46]. Hence v_c can be represented by only fundamental dynamic phasor coefficients,

$$v_c = V_1 e^{j\omega_s t} + V_1^* e^{-j\omega_s t} \quad (4.8)$$

Assuming the fundamental component of the inductor current is symmetric with respect to the peak of actual inductor current [46], then

$$\langle qv_c \rangle_1 = \frac{2}{\pi} \int_{\alpha}^{\tau} v_c e^{-j\theta} d\theta = \frac{1}{\pi} \left[V_1 \sigma + V_1^* \sin(\sigma) e^{-2j(\xi+\phi)} \right] \quad (4.9)$$

where the definitions of ξ and ϕ can refer [46] and are also shown in Fig. 4.2.

The fourth-order state-space model of the TCSC is presented in (4.3) and (4.4).

4.2.1 Impedance Model with Fixed α

With fixed α control, the system matrix A is a constant matrix, hence the state space model given in (4.3) and (4.4) can be utilized to obtain the impedance matrix directly as follows:

$$Z_{TCSC}(s) = \frac{Y(s)}{U(s)} = C(SI - A)^{-1}B. \quad (4.10)$$

4.2.2 Impedance Model with α Control

Fig. 4.3 shows the impedance control loop of the TCSC.

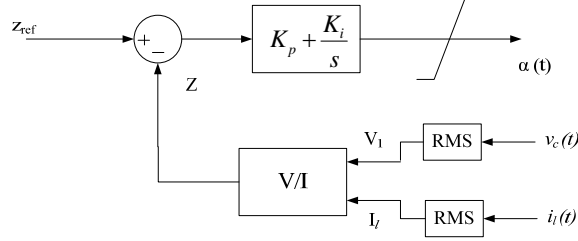


Figure 4.3. Control block diagram for α control in TCSC.

The Laplace expression of the firing angle is as follows:

$$\Delta\alpha(s) = -H(s)\Delta Z(s). \quad (4.11)$$

Impedance Z is computed from the instantaneous voltage and current measurements as shown in Fig. 4.3. The expression of Z is as follows:

$$Z = \left| \frac{V_1}{I_{l1}} \right| = \sqrt{\frac{(V_1^R)^2 + (V_1^I)^2}{(I_{l1}^R)^2 + (I_{l1}^I)^2}} \quad (4.12)$$

where I_l^0 and V_1^0 are the fundamental components of initial line current and capacitor voltage.

Applying small perturbation and the resulting impedance deviation ΔZ can be expressed as:

$$\Delta Z = \left[\frac{\partial Z}{\partial X} \right]^T \Delta X + \left[\frac{\partial Z}{\partial U} \right]^T \Delta U \quad (4.13)$$

When α is controlled, the system matrix A is no longer a constant matrix. The resulting small signal state space model is given as:

$$\Delta \dot{X} = A(\alpha_0)X + \frac{\partial A}{\partial \alpha} X_0 \Delta \alpha + BU \quad (4.14)$$

Applying Laplace transformation leads to

$$sX(s) = A(\alpha_0)X(s) + \frac{\partial A}{\partial \alpha} X_0 \Delta \alpha + BU(s) \quad (4.15)$$

Substituting (4.11) and (4.13) into (4.15) leads to

$$\frac{X(s)}{U(s)} = \underbrace{\left(sI - A + \frac{\partial A}{\partial \alpha} X_0 H(s) \frac{\partial Z}{\partial X} \right)^{-1} \left(-\frac{\partial A}{\partial \alpha} X_0 H(s) \frac{\partial Z}{\partial U} + B \right)}_{G_{UX}(s)} \quad (4.16)$$

Hence the impedance model is expressed as:

$$Z_{TCSC}(s) = \frac{Y(s)}{U(s)} = CG_{UX}(s) \quad (4.17)$$

4.3 Frequency Domain Analysis

4.3.1 Stability Criterion

For single-input single-output (SISO) systems, Nyquist plots and Bode plots of the loop gain $Y(s)Z(s)$ can be used to detect stability issues and determine phase margin and gain margins. However, the derived impedance models in this chapter are two by two matrices for each impedance. In turn, the equivalent control systems are multi-input multi-output (MIMO) systems. To examine stability for MIMO system, [48] proposes to plot the Nyquist maps of the eigenvalues of the loop gain. Such technique is employed in [49].

Singular values of the return matrix $T(s) = I + Y_l(s)Z_s(s)$ delivers a good measure of stability of a system [50]. The difference between maximum and minimum singular value can be used as an indicator of the system “ill conditioning” [50]. The larger the difference, the more the system is prone to “ill condition”. In addition, if the minimum singular value of the return reference matrix is equal to or more than one, the system is guaranteed to have a phase margin of ± 60 which means the

system is stable. The corresponding frequency at the minimum singular value indicates resonance frequency. This criteria can be employed to identify the ill conditioning frequencies of the system.

4.3.2 Case Study

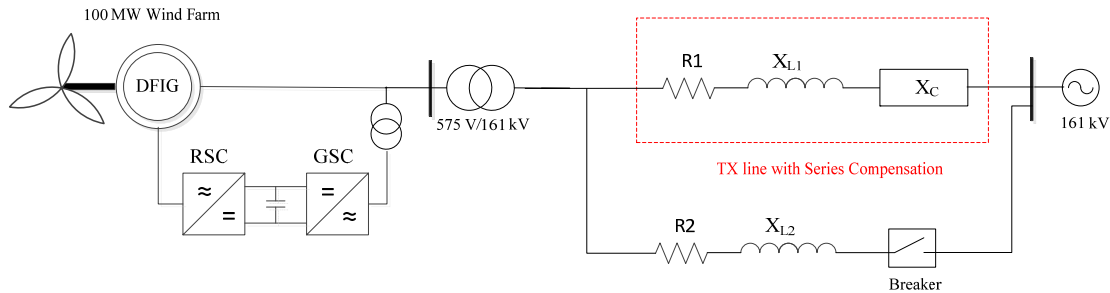


Figure 4.4. The study system: 100 MW Wind farm connected to infinity bus through two parallel transmission lines.

In this subsection, the developed TCSC impedance model is used for stability analysis. A case study considered is a Type 3 wind farm interconnected with a series compensated network. The system is modified Second Benchmark model which has been widely used for SSR studies [51]. It is composed of two parallel transmission lines, one of them is series compensated. To entice the SSR mode, three-phase breakers have been used in uncompensated line to trip the line at specific moment. The system diagram is shown in Fig. 4.4.

The wind farm is represented with a lumped DFIG model which is connected to the system through a transformer. This model is considered as the study system for the proposed work here. SSR study is carried out for two series compensation methods: fixed capacitor and a TCSC. Series capacitor circuit can be modeled easily with space vector representation hence impedance model can be achieved directly [38]. As one case study is defined based on different control parameters of the Rotor Side Converter (RSC) controller, the inner current control loop of the RSC is illustrated in Fig. 4.5. Two PI controllers have been used to regulate the currents to yield a proper voltage output. The gain settings of two PI controllers are the same for d - axis and q - axis. For fixed capacitor and TCSC scenarios, the compensation degree at 60 Hz will be the same. The parameters of the transmission line, capacitor size and TCSC parameters are listed in Table 4.1.

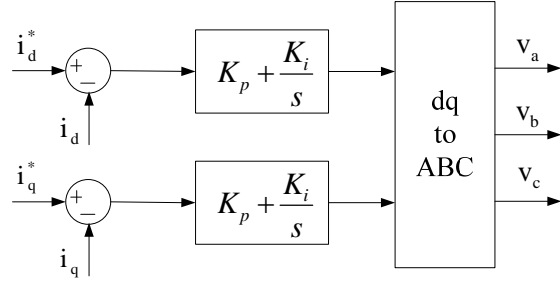


Figure 4.5. Inner current control loop for rotor side converter of DFIG.

Table 4.1. Parameters of the transmission lines

Transformer Ratio	575V/161kV
Transformer X_t	0.1 pu
Power base	100 MVA
Frequency	60Hz
R_1	0.02 pu
R_2	0.02 pu
X_{l1}	0.5 pu
X_{l2}	0.02 pu
X_c at 50 % compensation	64.8 Ω
L_{TCSC}	3.8 mH
C_{TCSC}	65e-6 F
α at 50% compensation level	72 $^\circ$

4.3.2.1 Fixed Series Compensation

Phase domain based scalar impedance models for an DFIG has been developed in [38]. For a transmission line with fixed series compensation, the scalar impedance model is $R + sL + \frac{1}{sC}$.

Fig. 4.6 and 4.7 present the Nyquist plot for the loop gain $Y_{DFIG}(s)Z_{net}(s)$ and the Bode plots for $Z_{DFIG}(s)$ and $Z_{net}(s)$, where $Z_{net}(s)$ is the impedance of the series compensated line, $Z_{DFIG}(s)$ is the DFIG impedance, and $Y_{DFIG} = 1/Z_{DFIG}$. The two figures show the resonance frequencies at different compensation level. It can be seen from the bode plot that the higher the compensation degree, higher the network resonance frequency f_n . Resonant frequencies for 40 %, 50 %, and 70 % are 29 Hz, 32 Hz and 38 Hz, respectively. It is shown that phase margin reduced with increasing the compensation level and nyquist plot for all compensation levels encircles[-1,0] in clockwise direction implying the system goes unstable for all compensation levels. Simpower simulation presented in section IV validates this. Note that the network resonant at f_n will be observed as an oscillation made with a complementary frequency which is $f_s - f_n$, where f_s is 60 Hz.

Considering only the fundamental frequency component, the dynamic phasor based impedance models for the transmission line and the fixed capacitor are presented as follows.

$$Z_{line} = \begin{bmatrix} R + sL & \omega_s L \\ -\omega_s L & R + sL \end{bmatrix} \quad (4.18)$$

$$Z_{FC} = \begin{bmatrix} \frac{s}{s^2 C + \omega_s^2 C} & -\frac{\omega_s}{s^2 C + \omega_s^2 C} \\ \frac{\omega_s}{s^2 C + \omega_s^2 C} & \frac{s}{s^2 C + \omega_s^2 C} \end{bmatrix} \quad (4.19)$$

$$Z_{net} = Z_{line} + Z_{FC} \quad (4.20)$$

Fig. 4.8 (a) presents the singular value of the return different matrix $1 + Y_{DFIG}Z_{net}$. It is found that ill conditioning frequencies correspond to the frequencies of the SSR modes. As for all the compensation levels the minimum singular value is less than one at SSR frequencies, implying instability in the system for all the cases.

For example, at 40% compensation level, the singular value plot shows that at 31 Hz, the minimum singular value reaches the lowest point. This corresponds to the 29 Hz resonance frequency in

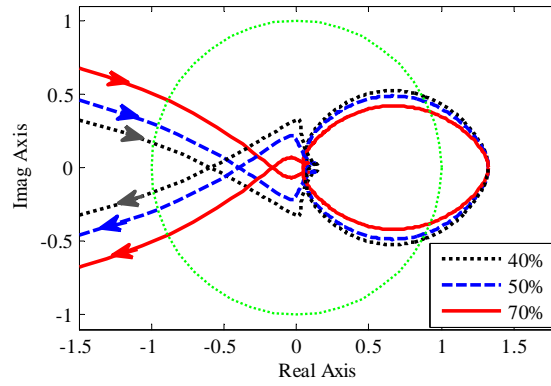


Figure 4.6. Nyquist plots for different compensation levels, RSC: $K_p = 0.6$, $K_i = 8$.

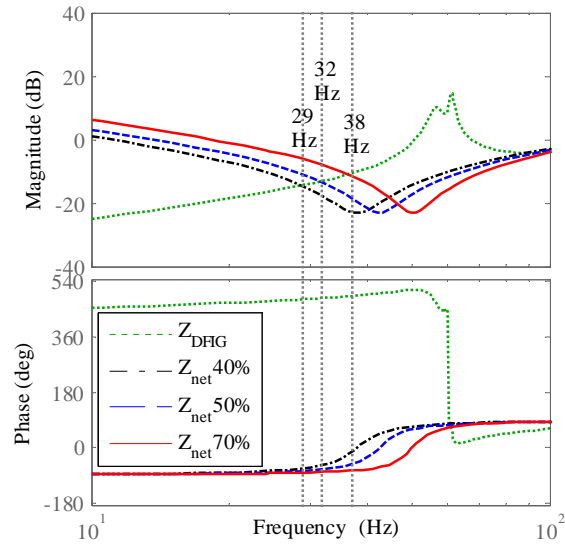


Figure 4.7. Bode plots for different compensation levels, RSC: $K_p = 0.6$, $K_i = 8$.

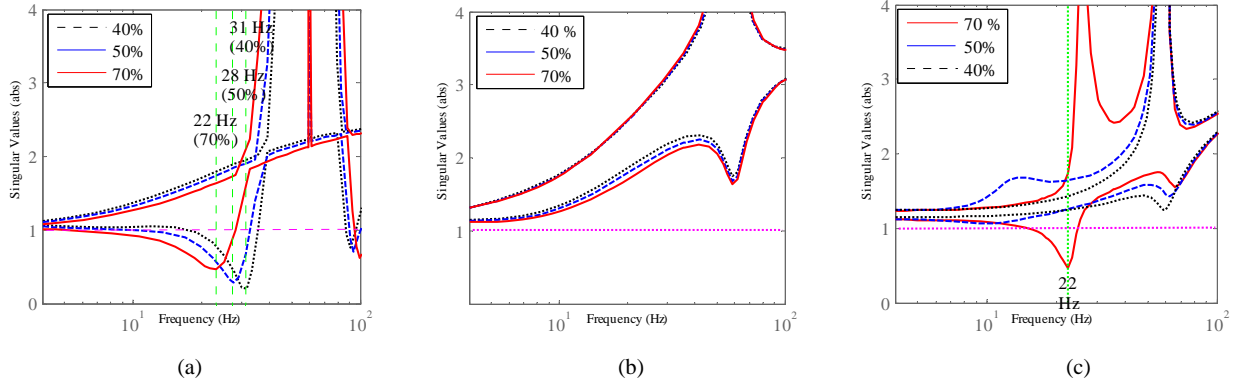


Figure 4.8. Singular value plots of $1 + Y_{DFIG}Z_{net}$ for each compensation level of different modes; (a) fixed capacitor, (b) constant alpha mode for TCSC, (c) impedance control of TCSC, RSC: $K_P = 0.6$, $K_i = 8$, TCSC gains: $K_P = 0.53$, $K_i = 3$.

the phase domain in Fig. 4.7 because they are complementary to each other. At 50% compensation level, the singular value plot shows that at 28 Hz, the minimum singular value reaches the lowest point. This corresponds to the 32 Hz resonance frequency in the phase domain in Fig. 4.7. At 70% compensation level, the singular value plot shows that at 22 Hz, the minimum singular value reaches the lowest point. This corresponds to the 38 Hz resonance frequency in the phase domain in Fig. 4.7.

4.3.2.2 TCSC Effect

- Effect of Fixed α Mode:

Fig. 4.8 (b) shows the effect of different compensation levels of TCSC in constant alpha mode on system stability. Different values for Alpha are given in Table 4.2. It can be concluded that TCSC in constant alpha mode for all the compensation levels wont provide any instability problems for the system cause the absolute value of singular values are greater than one for three cases.

Table 4.2. Different reference impedance of TCSC for different compensation levels

Compensation	α	Z_{ref}
40 %	75^0	52 Ω
50 %	71.9^0	65 Ω
70 %	69.35^0	91 Ω

- Impedance control of TCSC:

Effect of different compensation levels of the TCSC when it is enhanced with Impedance controller in capacitive mode is illustrated in Fig. 4.8 (c). The reference values of TCSC impedances for different compensation level are presented in Table 4.2. It can be observed that as the compensation level increases to 70 % the system faces with SSR and the frequency of the unstable mode is 22 Hz. However, impedance control mode of the TCSC is stable for 40 % and 50 % compensation of TCSC.

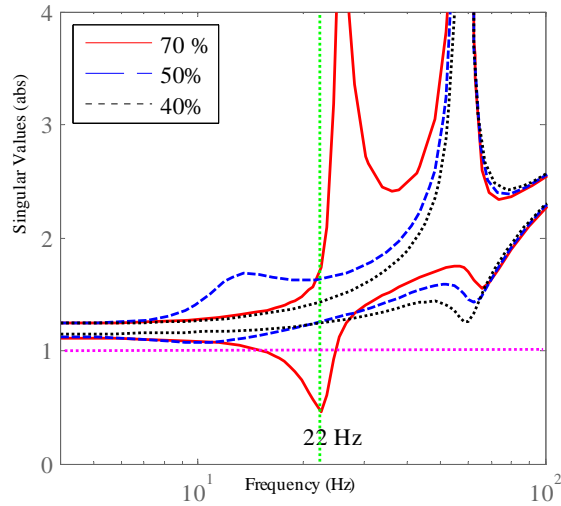


Figure 4.9. Singular value plot of $1 + Y_{DFIG}Z_{net}$ for different compensation levels of TCSC at steady-state, RSC: $K_P = 0.6$, $K_i = 8$, TCSC gains: $K_P = 0.53$, $K_i = 3$.

- Effect of TCSC Controller parameters:

Fig. 4.10 presents singular value plots of the return matrix $1 + Y_{DFIG}Z_{net}$ for different gains of TCSC controller in impedance control mode. The higher the gain of TCSC controller, the system is more prone to ill conditioning. This implies that lower gains in TCSC impedance control increase the stability margin of the system. From this figure it can be noted that the SSR mode is 28 Hz when the TCSC K_p is set to 0.8 which is the highest one.

- Effect of RSC parameters:

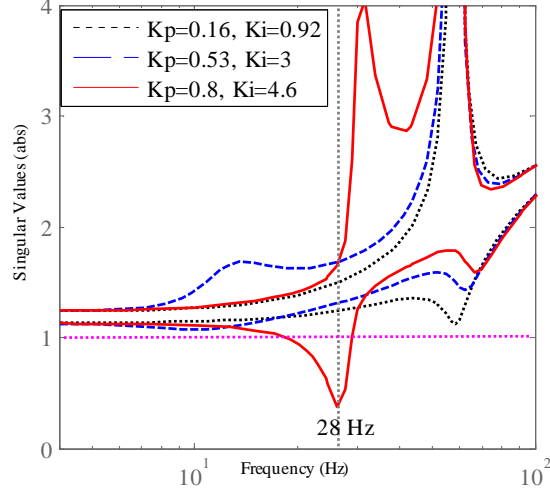


Figure 4.10. Singular value plot of $1 + Y_{DFIG} Z_{net}$ for different K_p , K_i of TCSC for 50% compensation level at steady-state, RSC: $K_P = 0.6$, $K_i = 8$.

In this case, the TCSC is in impedance control (capacitive mode) and the controller parameters are fixed. The DFIG RSC parameters are changed to examine the effect of different RSC gains on SSR. Fig. 4.11 presents the singular values of the return different matrix for different RSC controller parameters. It is found that when TCSC is in constant impedance control mode, for the selected RSC gains, the system is stable, but from the difference between lower and higher singular values for each case, the lower the gain of RSC controller, the gap between lower and higher singular value is more which clarifies the system is more prone to ill conditioning.

4.4 Time-Domain Simulation Results

In this section, analysis results will be verified by time-domain simulation results. Time-domain simulation is carried out in Matlab/Simpowersystems where Thyristor switching details are included. Two different scenarios will be studied.

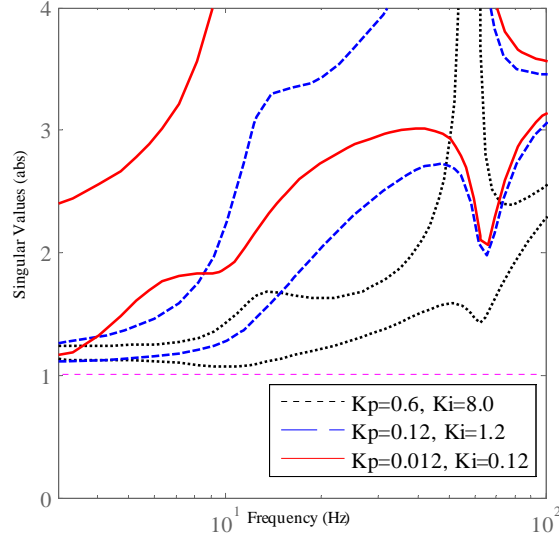


Figure 4.11. Singular value plot of $1 + Y_{DFIG}Z_{net}$ for different K_p, K_i of RSC for 50% compensation level at steady-state, TCSC: $K_P = 0.32, K_i = 1.84$.

4.4.1 Scenario One

In this case, the power system is composed of a wind farm integration of 70 wind turbines with 1.5 MW output power, as a whole transmitting the 100 MW power to the grid through two AC transmission lines. A TCSC is inserted in series with one of the transmission lines aiming to inject a series capacitance into the line and increase the power transfer capability of that AC line. A line trip is considered for the uncompensated AC line at time 4 sec as a contingency studied. The main aim of this scenario is to investigate the effect of different parameters of the system on SSR.

4.4.1.1 Effect of Different TCSC Gains

Fig. 4.12 shows the effect of different TCSC controller gains on SSR. It should be noted that the gain settings of the RSC of the DFIG has been kept constant and also the compensation level is set to 50% to verify the effect of different TCSC gains on SSR. It has been observed that as the gain settings of TCSC controller are increased, the system is more likely to be unstable as for the $K_p = 0.8$ the SSR happens at the frequency around 27 Hz. The simulation findings corroborate with the analysis findings shown in Fig. 4.10.

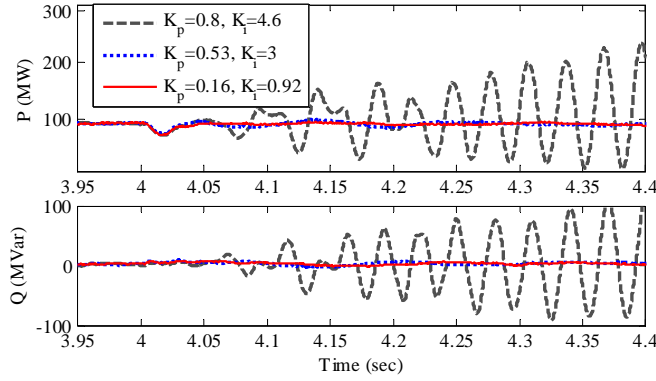


Figure 4.12. Simulation results for different K_p , K_i of TCSC for 50% compensation level at steady-state, RSC gains: $K_P = 0.6$, $K_i = 8$.

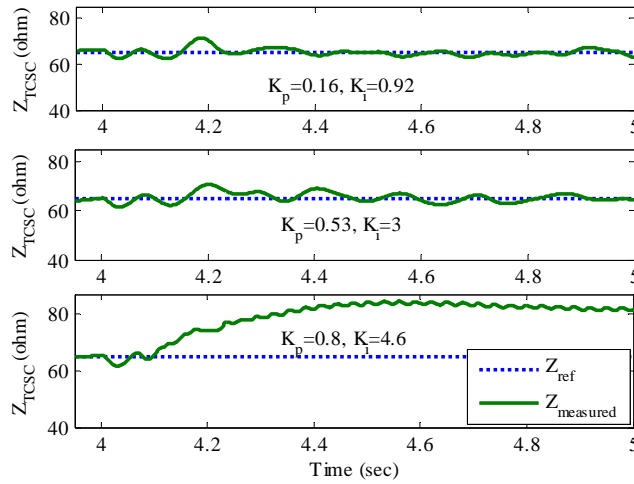


Figure 4.13. Simulation results for comparison of reference impedance and TCSC measured impedance for different K_p , K_i of TCSC for 50% compensation level at steady-state, RSC gains: $K_P = 0.6$, $K_i = 8$.

Comparison of different TCSC gains on measured and reference impedance of DFIG is also shown in Fig. 4.13 which verifies for the highest TCSC gains, the system is unstable which verifies the analysis part.

4.4.1.2 Effect of Different TCSC Compensation Level

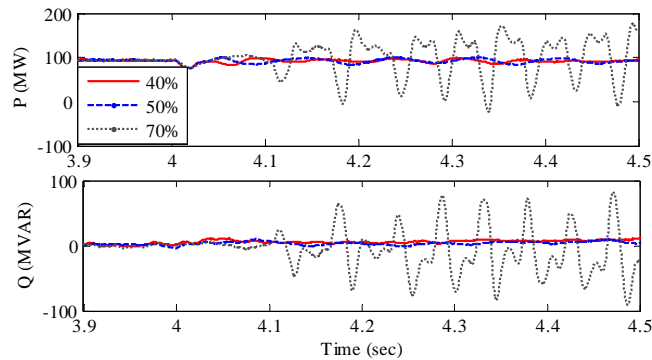


Figure 4.14. Simulation results for different compensation of TCSC, RSC: $K_P = 0.6$, $K_i = 8$, TCSC gains: $K_P = 0.53$, $K_i = 3$.

In this part, three different compensation levels have been considered for TCSC as 40%, 50%, and 70% in impedance control mode of operation. The level of compensation can be mentioned as the percentage of the line reactance to be compensated by the TCSC and it will be inserted as the reference value of TCSC impedance. For example for 50 % the reference TCSC impedance is set to 65Ω . Results of simulation for this case has been illustrated in Fig. 4.14. The RSC gains of the DFIG and the TCSC impedance controller gain have been kept constant in different compensation levels. It can be observed that as the compensation level is increased to 70 %, the active power of the line is faced with oscillations around 22 Hz, but for the 40 % and 50 % the system is stable. These results match with the singular value analysis results in Fig. 4.9.

4.4.1.3 Effect of Different RSC Gains

in this situation, the compensation level of the TCSC is set to 50% and the TCSC controller gains have been kept constant. All three cases are stable as previously discussed in Fig. 4.11. It can be observed from Fig. 4.15 that, as the gain settings of RSC are increased, the system is more

likely to be stable. This phenomenon is very different from the case where fixed capacitor is used. In [52, 38], studies show that increasing RSC gains makes the system prone to SSR.

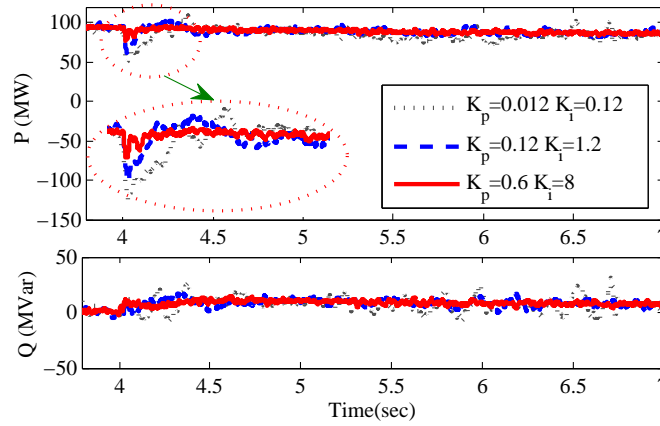


Figure 4.15. Simulation results for different K_p , K_i of DFIG RSC for 50% compensation level at steady-state, TCSC: $K_P = 0.32$, $K_i = 1.84$.

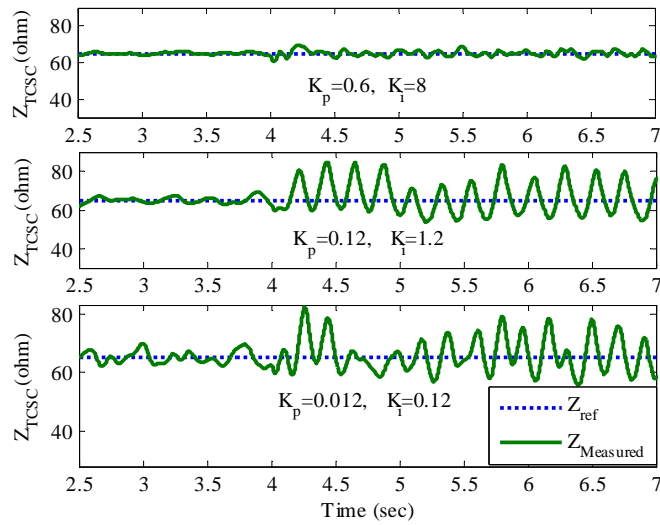


Figure 4.16. Simulation results for comparison of reference impedance and TCSC measured impedance for different K_p , K_i of DFIG RSC for 50% compensation level at steady-state, TCSC: $K_P = 0.53$, $K_i = 3$.

Moreover, comparison of TCSC measured impedance and reference signal has been illustrated in Fig. 4.16 which verifies the more RSC gains of DFIG, the system is more stable.

4.4.2 Scenario Two

This case is dedicated to compare the results of TCSC compensated system with Fixed Capacitor compensated power system. Same power system has been considered here but the TCSC is replaced with fixed series capacitor. The contingency for this case is considered as a line trip which is applied at time 3 sec. To study this case, firstly, the power system is enhanced with three different levels of fixed capacitors. At the latter point, the Fixed Capacitor in the 70% compensation level will be replaced by the 70% compensated TCSC in order to compare the results of fixed capacitor with TCSC.

4.4.2.1 Effect of Different Fixed Capacitor Compensation Level

Results of simulation for different compensation level are illustrated in Fig. 4.17. It can be observed that, as the compensation level is increased, the system is more prone to instability and for the all the compensation levels, the system has lost his stability completely. The dominant mode in this condition has the frequency of about 21 Hz for 70% compensation, 28 Hz for 50% compensation and 32 Hz for 40% compensation. Referring to Fig. 4.8 the results of simulation are in agreement with singular value analysis which has been performed in the previous section.

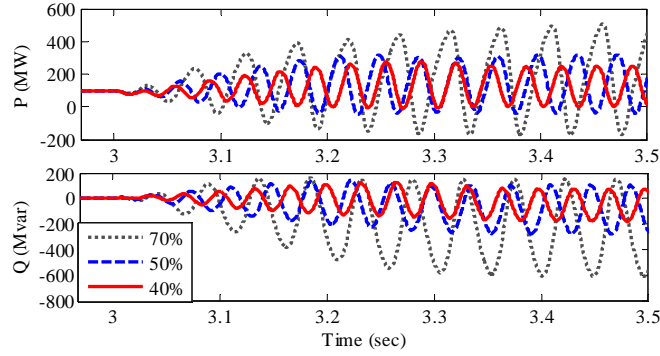


Figure 4.17. Simulation results for different compensation level of fixed capacitor, $X_L = 0.5(p.u.)$, RSC: $K_P = 0.6$, $K_i = 8$.

4.4.2.2 Comparison of TCSC and Fixed Capacitor

In this part, the compensation level is selected as 70% and the results of simulation for TCSC and Fixed capacitor is shown in Fig. 4.18. It can be observed that, as the line trip happens, the fixed capacitor compensated power system fails to sustain the stability and large fluctuations will be experienced in the active and reactive power of the DFIG unit. In contrast, the TCSC in impedance control mode can handle the SSR even in high level of compensation and the system will retain the stability after a few cycles. It has to be mentioned that in this case, the gain settings of the TCSC has been selected as lowest as possible to make the controller robust enough.

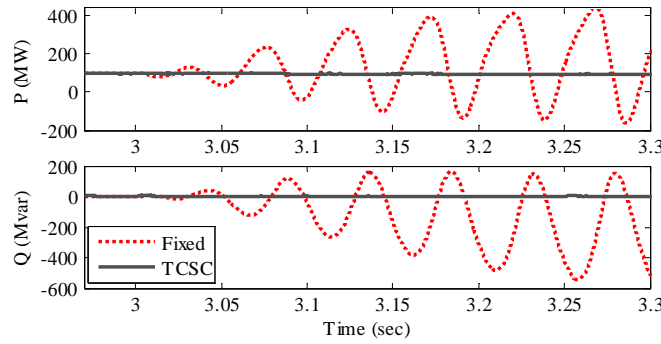


Figure 4.18. Results of comparison between fixed capacitor and TCSC in 70% compensation of the line reactance, RSC: $K_P = 0.6$, $K_i = 8$, TCSC: $K_P = 0.16$, $K_i = 0.92$.

The simulation results corroborate with the analysis results. In addition, important observations with reference value are drawn as follows:

1. With a TCSC compensated transmission line, a DFIG based wind farm can be radially connected with the line and operate. On the other hand, if fixed capacitor is used, Type 3 wind farms cannot be radially connected with series compensated lines due to SSR.
2. RSC current controllers no longer pose threat to SSR in TCSC compensated Type 3 wind farm systems.

4.5 Conclusion

This chapter develops impedance models of TCSC based on dynamic phasor concept. This model is applied for SSR analysis and can shed insights into identifying impacting factors on SSR. With the derived impedance models, Nyquist-stability-criterion can be applied to detect SSR stability in systems with TCSC. This chapter successfully demonstrates TCSC's capability in avoiding SSR under capacitive mode scheme in Type 3 wind generator interconnection systems. In addition, sensitivity of TCSC's impedance control parameters on SSR stability is also investigated. The analytical results obtained through impedance models are validated by detail based time-domain simulation in Matlab/SimPowerSystems.

CHAPTER 5

MODELING OF MICROGRIDS IN UNBALANCED CONDITIONS

This chapter ¹ investigates the effect of unbalance modeling of microgrid based on dynamic phasor approach.

5.1 Introduction

Increasing efficiency and decreasing cost of solar technology promotes substantial growth of Photovoltaic (PV) power integration in modern power systems. The total capacity of grid connected PV systems has increased from 300 MW in 2000 to 21 GW in 2010 [53]. PV has shared a fair amount of renewable energy penetration in microgrids where the PV power supplies electrical loads for local communities[54, 55, 56]. New government policies and incentives encourage more and more single-phase PV systems to be connected. In addition, induction machine based loads are dominant in distribution systems. Analytical models of such unbalanced distribution systems would provide insights of the system and further be used for small-signal and large-signal stability analysis. The analysis will help identify stability issues and mitigate related problems.

For unbalanced systems, abc frame-based dynamic models can be used for dynamic performance examination. Simulation packages such as PSCAD [57] and Matlab/SimPowerSystems [58] are based on simulation models with instantaneous variables, *e.g.* instantaneous voltages and currents in three phases. Conventional linearization at an operating condition cannot be applied to linearize these models due to the periodic varying state variables. The necessary condition for small-signal analysis is to have constant values for state variables at steady state [59]. Transforming the models to a synchronous rotating reference (dq) frame is the most common technique utilized to overcome

¹This chapter was published in in Power Systems, IEEE Transactions on , vol.30, no.6, pp.3102-3109, Nov. 2015. Permission is included in Appendix A.

the above problem [59]. However the negative-sequence components presented in an unbalance system will be converted to 120 Hz ac variables in a dq -reference frame. Hence, dq -reference frame based models do not offer the capability of small-signal analysis under unbalanced topology and operating conditions.

On the other hand, dynamic phasor-based modeling [30, 60, 61, 31, 62], an averaging technique, has been demonstrated to be capable of converting periodic varying state variables into dc state variables. It has been used in electrical machines analysis [30, 63, 64], HVDC and FACTS analysis [61, 31, 62]. For example [62] presents an averaged model of LCC based HVDC system which is capable of representing low frequency dynamic of the converters in both AC and DC sides. Dynamic phasor models are ideal for small-signal analysis. Dynamic phasor modeling technique also provides very accurate simulations for larger time steps [30, 62, 63]. Moreover, it can reflect the unbalance modeling techniques as well [30, 60, 61, 31, 64]. For example, in [30] the Induction Machine (IM) as well as Permanent Magnet Synchronous Generator (PMSG) model in unbalanced conditions have been analyzed based on Positive, Negative, Zero (PNZ) reference frame analysis conducted by Dynamic Phasor. Furthermore, in [61] the dynamic phasor modeling technique is used to model the Unified Power Flow Controller (UPFC) as a FACTS device in unbalanced operating conditions connected to single machine infinite bus power system.

In [65] dynamic phasor has been adopted in modeling for distribution systems, considering fundamental frequency component only. The case study does not contain single-phase elements or unbalanced topologies. The work in [66] presents a microgrid model containing a synchronous generator model while considering both positive- and negative- sequence components. However the inverter control is not modeled in detail.

The literature lacks a comprehensive unbalanced distribution system model (methodology) suitable for both small-signal analysis and nonlinear time-domain simulation at unbalanced conditions. Hence work presented here investigates the effect of unbalance modeling of microgrid based on dynamic phasor approach. A typical load, Induction Machine (IM), are modeled based on pnz dynamic phasor approach in order to reflect the dynamics under the unbalanced conditions. The major contribution of this work is the detailed modeling of single phase PV system with PR con-

troller and LCL filter, and studying the impact on the system performance using dynamic phasor. In addition, Power Factor Correction (PFC) and resistive load are added to the system to form a real microgrid characteristics. Final model is achieved by converting the entire system to abc reference frame. Since the model is based on dynamic phasor approach, fast and accurate simulation can be guaranteed. The nonlinear model is built in favor of transfer function-based or impedance based models. Hence the model we built can be used for large-signal stability analysis. The model can be linearized at an operating condition to carry out small-signal analysis as well.

5.2 Dynamic Phasor Approach

Dynamic Phasor (DP) models provides abundant merits, including: (i) the capability of small-signal analysis and (ii) availability of large step size simulations. The main idea of DP comes from describing the waveform $x(\tau)$ on interval $[t - T, t]$ by Fourier Series:

$$x(\tau) = \sum_{k=-\infty}^{\infty} X_k(t) e^{jk\omega_s t} \quad (5.1)$$

where $\omega_s = 2\pi/T$ and X_k is the k -th complex Fourier coefficient or Dynamic Phasor (DP). Due to the fact that these coefficients are constant at steady state, the DP model can be linearized for small-signal analysis. The k -th DP of the time varying signal $x(\tau)$ can be obtained by (5.2) [67]:

$$X_k(t) = \frac{1}{T} \int_{t-T}^t x(\tau) e^{-jk\omega_s \tau} d\tau = \langle x \rangle_k(t). \quad (5.2)$$

where $\langle \cdot \rangle_k$ denotes the k th harmonic DP.

The main characteristics of the DP modeling are as follow [67]:

$$\left\langle \frac{dx}{dt} \right\rangle_k = \frac{dX_k}{dt} + jk\omega X_k \quad (5.3)$$

$$\langle x \cdot y \rangle_k = \sum_{l=-\infty}^{\infty} (X_{k-l} \cdot Y_l) \quad (5.4)$$

(5.3) describes the relationship between the DP of a derivative versus the DP of the original signal while (5.4) describes the relationship between the DP of a product versus the DPs of the individual variables.

In this study, the main aim is to derive the DP model of a distribution system composed of a single-phase PV, a three-phase induction machine, a PFC and distribution lines represented by RL circuits. The DP models in the abc frame can be derived by converting the DP model from the positive-, negative-, and zero-sequence (*pnz*) reference frame [30]. The original signals in the abc frame can be expressed by *pnz* DPs as follows.

$$\begin{bmatrix} x_a \\ x_b \\ x_c \end{bmatrix} (\tau) = \sum_{l=-\infty}^{\infty} e^{jk\omega_s\tau} \frac{1}{\sqrt{3}} \underbrace{\begin{pmatrix} 1 & 1 & 1 \\ \alpha^* & \alpha & 1 \\ \alpha & \alpha^* & 1 \end{pmatrix}}_M \begin{bmatrix} X_{p,l} \\ X_{n,l} \\ X_{z,l} \end{bmatrix} \quad (5.5)$$

where l stands for the harmonic component index, M is the transformation matrix ($M^H = M^{-1}$) from *pnz* to *abc* and p , n , and z stand for positive-, negative-, and zero-sequences. It is easy to see that the DPs of abc variables have the following relationship with the DPs of *pnz*-sequences.

$$\begin{bmatrix} X_{a,l} \\ X_{b,l} \\ X_{c,l} \end{bmatrix} = M \begin{bmatrix} X_{p,l} \\ X_{n,l} \\ X_{z,l} \end{bmatrix} \quad (5.6)$$

In the next section, after introducing the entire system topology, the DP models of each element will be presented one by one, which will be integrated into the system model.

5.3 System Configuration and Modeling

The parameters presented in [68, 66] are utilized for the proposed study system shown in Fig. 5.1. The distributed system consists of a single-phase PV station installed in phase a of the system, a 3-phase induction machine, a 3-phase PFC and a 3-phase load.

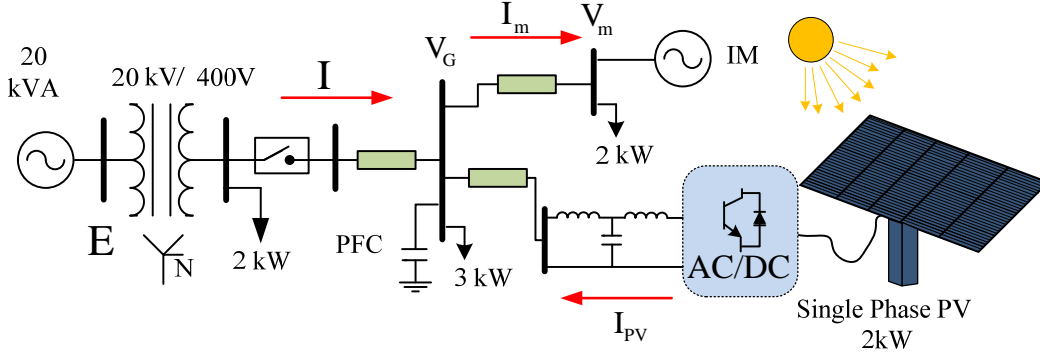


Figure 5.1. The study system.

5.3.1 DP Model of a Single-Phase PV

Traditionally, two-stage converters (a DC-AC converter after a DC-DC converter) have been used for PV systems. Two-stage converters need additional devices compared with single-stage converters. Therefore, single-stage converters have been implemented in PV grid integration [69, 70, 71, 72]. The basic configuration of a single-phase PV is illustrated in Fig 5.2. The main elements of the single-stage PV are the Proportional Resonant (PR) current controller and the output filters.

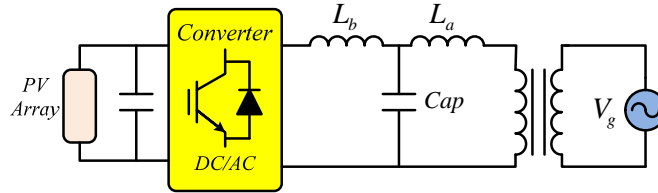


Figure 5.2. Basic configuration of PV system.

Fig. 5.2 shows the basic configuration of the LCL filter in a single-phase PV. It is composed of two inductances and one capacitor connected to the grid through a single phase transformer. The simplified model of PV connected to the grid with L or LCL filter has been illustrated in Fig 5.3. The output voltage of the DC-AC converter is v_{con} , the filter inductances for LCL filter are L_a and L_b . And the grid side voltage is v_G . The deducing process from Fig. 5.2 to Fig. 5.3 has been conducted based on the supposition that the PV can be modeled as voltage source V_{Con} in series with an inductance L_{Con} . Furthermore, the transformer can be modeled as an inductance X_T . Therefore, the relationship between L_a , L_b , L_1 and L_2 for the PV model with LCL filter can be

considered as: $L_2 = L_b + L_{Con}$ and $L_1 = L_a + L_T$. Furthermore, for PV connected to the L filter, if L_f is used for the L filter inductance, the deduction process is summarized to $L_3 = L_f + L_{Con} + L_T$.

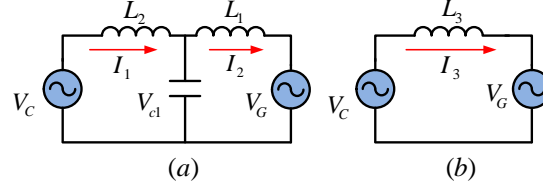


Figure 5.3. Simplified PV model with different combinations, (a) LCL filter, (b) L filter

Now, using the simple KVL and KCL laws, time domain equations of the system for the LCL filter can be derived based on:

$$\begin{aligned}
 L_1 \frac{di_1}{dt} &= (v_{c1} - v_G) \\
 L_2 \frac{di_2}{dt} &= (v_{con} - v_{c1}) \\
 C_1 \frac{dv_{c1}}{dt} &= (i_2 - i_1)
 \end{aligned} \tag{5.7}$$

The dynamics of the PV system with the LCL filter in DP is expressed as follows (It should be noted that only the first harmonic is considered for the derivation of dynamic phasor coefficients).

$$\begin{aligned}
 \dot{I}_1 &= \frac{1}{L_1}(V_{c1} - V_G) - j\omega_s I_1 \\
 \dot{I}_2 &= \frac{1}{L_2}(V_{con} - V_{c1}) - j\omega_s I_2 \\
 \dot{V}_{c1} &= \frac{1}{C_1}(I_2 - I_1) - j\omega_s V_{c1}
 \end{aligned} \tag{5.8}$$

It should be noted that V_{con} is the DP of the output voltage of the PV controller. For the L filter the basic DP equation of the PV system connected to the grid can be derived as:

$$\dot{I}_3 = \frac{1}{L_3}(V_{con} - V_G) - j\omega_s I_3 \tag{5.9}$$

A detailed control block diagram of the single-stage single phase PV is illustrated in Fig 5.4. It is composed of a Maximum Power Point Tracking (MPPT) unit, a Proportional Resonant (PR) controller, a Phase-Locked-Loop (PLL), and a Pulse Width Modulation (PMW) pulse generation unit. In this chapter, the effect of MPPT dynamics and PLL has been neglected for simplicity and special attention has been dedicated to the PR controller and the LCL filter.

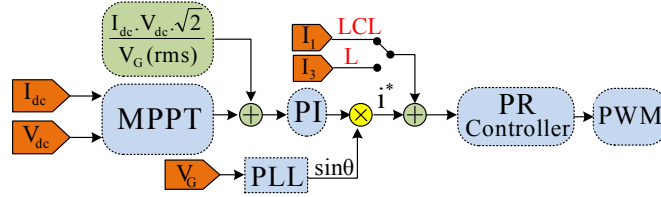


Figure 5.4. Basic control of a single-phase PV.

5.3.1.1 DP Model of a PR Controller

PR control is used to track AC signals. The PR controller in Fig. 4 tries to provide unity power factor power from the PV. Therefore, the current reference is synchronized with the grid voltage through a phase locked loop (PLL). The dynamics of a PR controller considering only the fundamental harmonics can be expressed as:

$$\begin{aligned}
 v_{con} &= \left(K_p + \frac{K_r s}{s^2 + (\omega_0)^2} \right) (i^* - i_1) \\
 &= \left[K_p + K_r \left(\frac{0.5}{s + j\omega_0} + \frac{0.5}{s - j\omega_0} \right) \right] (i^* - i_1)
 \end{aligned} \tag{5.10}$$

where i^* is the reference current comes from the PV array.

In the analytical model, the dynamics of PLL and MPPT are neglected for simplicity of the analysis. i_1 is the grid current when the PV is linked to the LCL filter. In a case where the PV is connected to the L filter, i_1 will be replaced by i_3 , which is the grid current. For the rest of modeling, the LCL filter is considered only. By defining intermediate state variables x_1 and x_2 ,

where

$$\begin{aligned}(s + j\omega_0)x_1 &= 0.5(i^* - i_1), \\ (s - j\omega_0)x_2 &= 0.5(i^* - i_1).\end{aligned}\tag{5.11}$$

Converting these equations to DP model results in (5.12).

$$\begin{aligned}\dot{X}_1 &= 0.5(I^* - I_1) - 2\omega_0 X_1 \\ \dot{X}_2 &= 0.5(I^* - I_1)\end{aligned}\tag{5.12}$$

The DP of the converter output voltage's fundamental frequency component can be expressed as:

$$V_{con} = K_{p1}(I^* - I_1) + K_{r1}(X_1 + X_2)\tag{5.13}$$

The DP model of a single-phase PV consists of (5.8), (5.12) and (5.13). The current reference I^* comes from this equation: $I^* = \frac{\sqrt{2}V_{dc}I_{dc}}{V_G(rms)} = \frac{\sqrt{2}P_{ref}}{V_G(rms)}$.

5.3.2 DP Model of an Induction Machine

Since the single-phase PV will introduce unbalance in the distribution system, the induction machine will be modeled to include the unbalance effect. Negative sequence component in the stator voltage can cause a clockwise rotating stator flux. When this flux is interacting with the clockwise rotating rotor flux, a 120 Hz torque ripple will appear. Therefore, the rotating speed will have a 120 Hz ripple. To count in the negative effect, the dynamic model of three-phase induction machine in [30] based on pnz -sequence components is adopted in this chapter. The space vector model of a squirrel cage induction machine with magnetic saturation and slot harmonics neglected is presented as follows.

$$\begin{aligned}
\vec{v}_s &= (r_s + L_s \frac{d}{dt}) \vec{i}_s + L_m \frac{d}{dt} \vec{i}_r \\
0 &= L_m \frac{d}{dt} \vec{i}_s + (r_r + L_r \frac{d}{dt}) \vec{i}_r - j\omega_r \frac{P}{2} (L_m \vec{i}_s + L_r \vec{i}_r) \\
J \frac{d}{dt} \omega_r &= \frac{3P}{4} L_m \Im(\vec{i}_s \vec{i}_s^*) - B\omega_r - T_L
\end{aligned} \tag{5.14}$$

where $\vec{v}_s, \vec{i}_s, \vec{i}_r$ denote the stator voltage, stator current and rotor current respectively. T_L is the mechanical torque and ω_r is the rotor speed. s and r denote the stator and rotor quantities, respectively. \Im denotes the imaginary part. The DP model of an induction machine can be derived by considering the positive- and negative-sequence components in stator/rotor voltages and currents, as well as the dc and the 120 Hz components in the rotating speed [30].

$$\begin{aligned}
V_{ps} &= (r_s + j\omega_s L_s + L_s \frac{d}{dt}) I_{ps} + (j\omega_s L_m + L_m \frac{d}{dt}) I_{pr} \\
0 &= (j\omega_s L_m + L_m \frac{d}{dt}) I_{ps} + (r_r + j\omega_s L_r + L_r \frac{d}{dt}) I_{pr} \\
&\quad - j\omega_{r0} \frac{P}{2} (L_m I_{ps} + L_r I_{pr}) - j\omega_{r2} \frac{P}{2} (L_m I_{ns}^* + L_r I_{nr}^*) \\
V_{ns}^* &= (r_s - j\omega_s L_s + L_s \frac{d}{dt}) I_{ns}^* - (j\omega_s L_m - L_m \frac{d}{dt}) I_{nr}^* \\
0 &= (L_m \frac{d}{dt} - j\omega_s L_m) I_{ns}^* + (r_r - j\omega_s L_r + L_r \frac{d}{dt}) I_{nr}^* \\
&\quad - j\omega_{r0} \frac{P}{2} (L_m I_{ns}^* + L_r I_{nr}^*) - j\omega_{r2} \frac{P}{2} (L_m I_{ps} + L_r I_{pr}) \\
J \frac{d}{dt} \omega_{r0} &= \frac{2P}{4} L_m \Im(I_{ps} I_{pr}^* + I_{ns}^* I_{nr}) - B\omega_{r0} - T_L \\
J \frac{d}{dt} \omega_{r2} &= \frac{2P}{j8} L_m \Im(I_{ps} I_{nr} - I_{ns} I_{pr}) \\
&\quad - (B + j2J\omega_s) \omega_{r2}
\end{aligned} \tag{5.15}$$

where subscripts p and n stand for positive and negative sequence components, respectively.

Since the DP model for the PV system is based on phase a, to integrate the induction machine model with the PV system model, the above pnz model will be converted to the abc frame using the relationship presented in (5.6). The block diagram of the conversion has been illustrated in Fig 5.5.

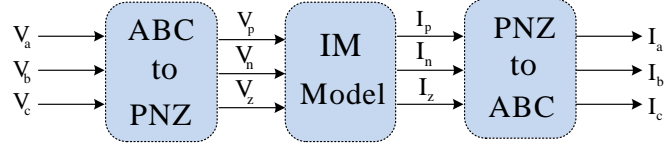


Figure 5.5. Conversion from abc to pnz and back to abc for an induction machine.

5.3.3 PFC and the Integrated System

Considering that there is a three-phase PFC in parallel with the PV, the circuit model of the microgrid can be illustrated as in Fig 5.6. where C denotes the capacitance of the PFC, I_M is

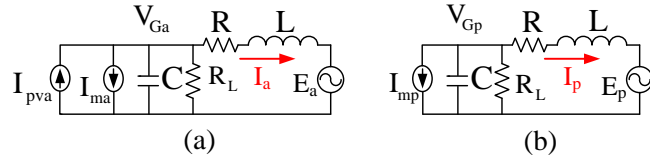


Figure 5.6. (a) Model of microgrid with PV in phase a , (b) model of microgrid in phase b and c

the induction machine's stator current, I is the line current, R and L are the distribution line's parameters, R_L is the load model and E is the system voltage.

For phase a, the DP model of the integrated system can be expressed as

$$\begin{aligned} \frac{d}{dt} I_a &= \frac{1}{L} (-(j\omega L + R)I_a + V_{Ga} - E_a) \\ \frac{d}{dt} V_{Ga} &= \frac{1}{C} (-(j\omega C + \frac{1}{R_L})V_{Ga} + I_{ma} + I_{PV} - I_a) \end{aligned} \quad (5.16)$$

where two state variables (grid voltage and grid current) have been introduced.

For phase b and c, the DP model of the integrated system can be expressed as:

$$\begin{aligned}\frac{d}{dt}I_p &= \frac{1}{L}(-(j\omega L + R)I_p + V_{Gp} - E_p) \\ \frac{d}{dt}V_{Gp} &= \frac{1}{C}(-(j\omega C + \frac{1}{R_L})V_{Gp} + I_{mp} - I_p)\end{aligned}\quad (5.17)$$

where p represents either phase b or phase c.

The entire system is composed of a PV system, an induction machine, a PFC, a load and the RL line. As a total, 17 complex state variables are presented, including the line currents (I_{abc}), PFC voltage ($V_{G,abc}$), induction machine stator currents ($I_{s,pn}$), induction machine rotor currents ($I_{r,pn}$), induction machine rotor speed (ω_{r0}, ω_{r2}), PV system state variables (output current (I_1), current before filter (I_2), voltage across the LCL filter capacitor (V_{c1}), the stator variables in the PR controller of the PV (X_1 and X_2)).

The complex state variables will be separated into real and imaginary components. Therefore, as a total, 34 real state variables are introduced for this DP model and small-signal analysis will show 34 eigenvalues.

5.4 Case Studies

The analytical model for the entire distribution system has been derived. The model was built in Matlab/Simulink. The nonlinear analytical model can be linearized based on a certain operating point using Matlab function “linmod”. Eigenvalue analysis can then be carried out for the linearized model. The same system was also built in Matlab/SimPowerSystems based on the physical circuit connection. The Matlab/SimPowerSystem model captures power electronic switching details and therefore is considered high-fidelity simulation model.

Three case studies have been carried out.

- In the *first* case, the analytical model in Simulink is benchmarked with the high-fidelity model in SimPowerSystemes. Dynamic simulation results are compared for the same dynamic event: a step change in load torque of the induction machine.

- In the *second* case, the effect of unbalance on the dynamic performance is investigated by applying a ramp change in irradiance of the PV. This dynamic event emulates the cloud effect on a PV and a distribution system.
- In the *third* case, the effect of grid line length on stability is investigated. Eigenvalue analysis and dynamic simulation are carried out.

5.4.1 Case Study 1

In this part, the analytical model-based simulation results are compared with the SimPowerSystems model based simulation results. A single-phase PV is connected to the phase *a* of the system at the Point of Common Coupling (PCC) shown as Fig.5.1. At $t = 4s$, the induction machine's mechanical torque was applied a step change from 28 N.M to 23 N.M.

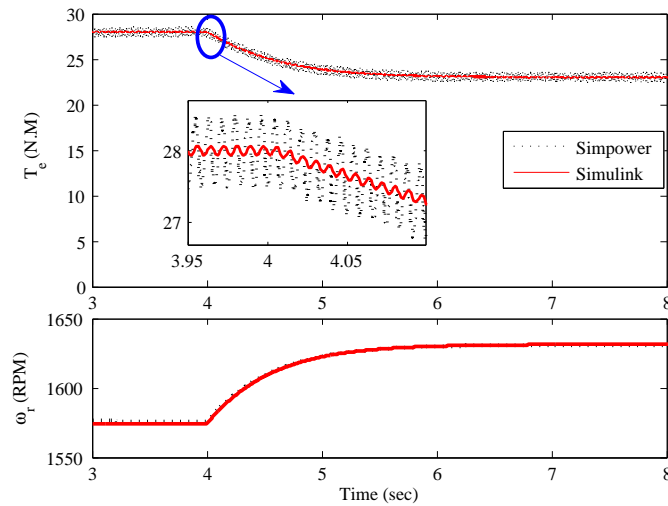


Figure 5.7. Simulation results of torque and rotor speed due to a step change in mechanical torque (from 28 N.M to 23 N.M).

The simulation results of the electromagnetic torque and the rotor speed of the induction machine have been illustrated in Fig. 5.7. The dynamic responses from the two models match each other well.

The simulation results for the line current, the line voltage and the PV current are presented in Fig. 5.8. The line current and line voltage simulation results from both models match well,

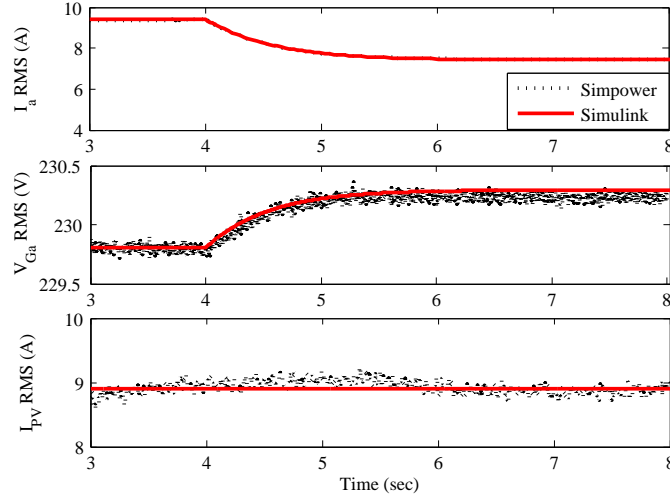


Figure 5.8. Simulation results of the IM stator current, stator voltage and PV current due to a step change in mechanical torque (from 28 N.M to 23 N.M).

which demonstrates the accuracy of the analytical model derived in this chapter. The PV current from the SimPowerSystems simulation has dynamics related to the MPPT control and the dc side capacitor. In the analytical model, MPPT effect is neglected and the PV power is constant. V_G has negligible variation and therefore the PV current of the analytical model is almost constant.

5.4.2 Case Study 2

Eigenvalue analysis for the system with and without PV has been conducted and the results are presented in Tables 5.1 and 5.2. It can be observed from the tables that, due to the introduction of the PV, five pairs of eigenvalues are introduced and these eigenvalues are related to PV state variables such the LCL capacitor voltage V_{c1} , PR controller state variables X_1 , X_2 and the PV current I_{PV} .

In this part, the effect of the PV irradiance change will be simulated in both Matlab/Simulink and Matlab/SimPowersystems. The PV irradiance was set to 1000 W/M^2 previously. A ramp change will be applied at 4 sec to decrease the irradiance to 200 W/M^2 in 0.2 sec. Then after 1.4 sec, the irradiance will be set back to 1000 W/M^2 . The change of the irradiance has been illustrated in detail in the first figure of Fig. 5.9. The second figure of Fig. 5.9 shows the PV power

Table 5.1. Eigenvalues of the system without PV

Eigenvalue	damping ratio %	frequency(Hz)	dominant state
$\left\{ \begin{array}{l} -959 \pm 5768i \\ -966 \pm 5935i \\ -966 \pm 5935i \\ -959 \pm 5014i \\ -966 \pm 5181i \\ -966 \pm 5181i \end{array} \right\}$	$\left\{ \begin{array}{l} 16.4 \\ 16.07 \\ 16.06 \\ 18.78 \\ 18.33 \\ 18.33 \end{array} \right\}$	$\left\{ \begin{array}{l} 918 \\ 945 \\ 945 \\ 798 \\ 825 \\ 825 \end{array} \right\}$	V_G, I
$-133.37 \pm 308i$	39.68	49	I_{ps}
$-137.95 \pm 117i$	76.37	18.6	I_{pr}
$-133.38 \pm 445i$	28.69	70.9	I_{ns}
$-137.95 \pm 637i$	21.15	101	I_{nr}
-0.76 ± 754	0.1	120	ω_{r2}
$-1.54 \pm 0i$	100	0	ω_r

Table 5.2. Eigenvalues of the system with PV

Eigenvalue	damping ratio %	frequency(Hz)	dominant state
$\left\{ \begin{array}{l} -966 \pm 5935i \\ -967 \pm 5848i \\ -993 \pm 5607i \\ -993 \pm 4853i \\ -966 \pm 5181i \\ -967 \pm 5094i \end{array} \right\}$	$\left\{ \begin{array}{l} 16.06 \\ 16.31 \\ 17.43 \\ 20.04 \\ 18.33 \\ 18.65 \end{array} \right\}$	$\left\{ \begin{array}{l} 944 \\ 931 \\ 892 \\ 772 \\ 824 \\ 810 \end{array} \right\}$	V_G, I
$\left\{ \begin{array}{l} -855 \pm 8475i \\ -855 \pm 7721i \end{array} \right\}$	$\left\{ \begin{array}{l} 10.04 \\ 11.01 \end{array} \right\}$	$\left\{ \begin{array}{l} 1349 \\ 1229 \end{array} \right\}$	V_{c1}
$\left\{ \begin{array}{l} -1.87 \pm 754i \\ -1.87 \pm 0.10i \end{array} \right\}$	$\left\{ \begin{array}{l} 0.25 \\ 99.8 \end{array} \right\}$	$\left\{ \begin{array}{l} 120 \\ 0.02 \end{array} \right\}$	X_1, X_2
$-8218 \pm 377i$	99.9	60	I_{pv}
$-133.37 \pm 308i$	39.68	49	I_{ps}
$-137.96 \pm 117i$	76.23	18.6	I_{pr}
$-133.37 \pm 445i$	28.68	70.9	I_{ns}
$-137.96 \pm 637i$	21.17	101	I_{nr}
-0.75 ± 754	0.1	120	ω_{r2}
$-1.52 \pm 0i$	100	0	ω_r

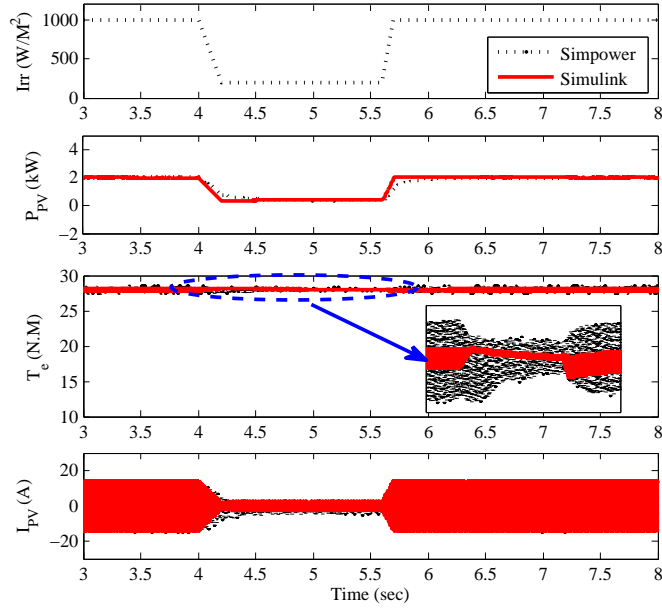


Figure 5.9. Simulation results for the effect of irradiance change.

which follows the irradiance command. The PV power of the analytical model is set to follow the change of the irradiance. It is noticed that the maximum power level (2 kW) is obtained when the irradiance is set to $1000 \text{ W}/\text{M}^2$. The third figure shows the electrical torque of the induction machine. When the irradiance is decreased due to clouds, the PV power is decreased, which leads to decrease the unbalance injection level to the system. The magnitude of the 120 Hz ripple has been decreased during the interval of 4 to 6 seconds. The last figure shows the PV current which has been decreased due the irradiance change.

Table 5.3. Eigenvalue comparison for different grid length

$l = 3km$			$l = 10km$			$l = 15km$			dominant State
Eigen value	damping ratio %	frequency(Hz)	Eigen value	damping ratio %	frequency(Hz)	Eigen value	damping ratio %	frequency(Hz)	
$\{-967 \pm 5848i\}$	$\{16.31\}$	$\{931\}$	$\{-984 \pm 3942i\}$	$\{24.23\}$	$\{627\}$	$\{-993 \pm 3411i\}$	$\{27.95\}$	$\{543\}$	V_G, I
$\{-993 \pm 5607i\}$	$\{17.43\}$	$\{892\}$	$\{-973 \pm 3700i\}$	$\{25.42\}$	$\{589\}$	$\{-968 \pm 3120i\}$	$\{29.64\}$	$\{497\}$	
$\{-133.37 \pm 308i\}$	39.68	49	$\{-123.21 \pm 321i\}$	35.81	51	$\{-116.74 \pm 328i\}$	33.53	52	I_{ps}
$\{-137.96 \pm 117i\}$	76.23	18.6	$\{-126.8 \pm 107i\}$	76.49	17	$\{-119.66 \pm 103i\}$	75.9	16.3	I_{pr}
$\{-133.37 \pm 445i\}$	28.68	70.9	$\{-123.21 \pm 432i\}$	27.38	69	$\{-116.74 \pm 426i\}$	26.43	67.8	I_{ns}
$\{-137.96 \pm 637i\}$	21.17	101	$\{-126.81 \pm 647i\}$	19.23	103	$\{-119.67 \pm 651i\}$	18.07	104	I_{nr}
$\{-0.75 \pm 754\}$	0.1	120	$\{-0.68 \pm 754\}$	0.09	120	$\{-0.60 \pm 754\}$	0.08	120	ω_{r2}
$\{-1.52 \pm 0i\}$	100	0	$\{-1.36 \pm 0i\}$	100	0	$\{-1.21 \pm 0i\}$	100	0	ω_r

5.4.3 Case Study 3

In Case 3, impact of the line length on the system stability has been investigated by both eigenvalue analysis and time-domain simulation in Matlab/SimPowerSystems. The eigenvalues of the system are presented in Table 5.3. The movement of the dominant modes is presented in Fig. 5.10. One of the dominant modes is related to a real-axis eigenvalue. The grid line length has been changed from 3 km to 15 km in order to observe its effect on dynamics. It is worth mentioning that increasing the line length more than 15 km causes non-convergence of the sweeping method for initialization. Therefore the results are only shown for the initial conditions where the system is able to converge. It can be found from Fig. 5.10 that as the line length increases, the real-axis eigenvalue will move to the right half plane. This can cause voltage instability of the system.

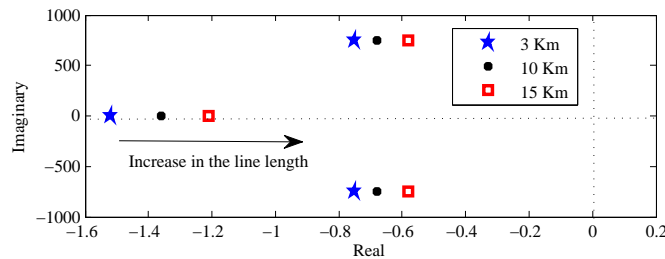


Figure 5.10. The dominant modes (120 Hz, and the voltage stability mode) by increasing the line length.

In time-domain simulations, a dynamic event to increase the grid line from 3 km to 30 km was triggered. Initially the grid connection consists of two parallel lines. At $t = 4s$, a breaker of one line is opened so the effective line impedance increases suddenly. Such an event causes the voltage stability mode to move to the right half plane (RHP). The stator voltage of the induction machine decreases significantly as shown in Fig. 5.11.

Fig. 5.12 presents the dynamic response of the RMS value of stator voltage from 3.5 seconds to 6 seconds, which clearly shows the decline of the voltage magnitude.

Due to the decrease of the stator voltage and system voltage magnitude, for the induction machine, its electromagnetic torque will decrease and its rotor speed will decrease as shown in Fig. 5.13 (a) and (b). For the PV, since the reference power is kept constant, the reference current

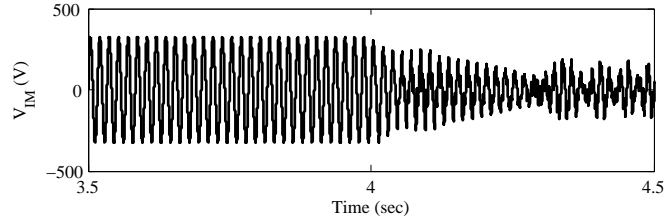


Figure 5.11. Stator voltage when the grid line length increases from 3 km to 30 km, Simulation results were produced by Matlab/SimPowerSystems.

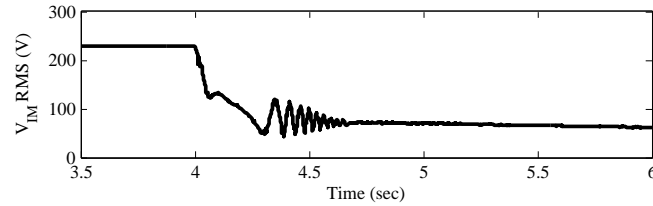


Figure 5.12. RMS stator voltage when the grid line length increases from 3 km to 30 km.

increases due to the decrease of the voltage. Hence, the PV current's magnitude increases as shown in Fig. 5.13. The entire system becomes unstable.

5.4.4 Remarks on Simulation Time

In the previous sections, it has been demonstrated that, time-domain simulation can be carried out by the Simulink model and the detailed model in SimPowerSystems. Due to its modeling details, the simulation time for the SimPowerSystems is considerably long. A comparison (Table 5.4) has been carried out to show the simulation time difference between the two models. Table

Table 5.4. Comparison of simulation time between two models

Time to be simulated	SimPowerSystems	Simulink
2 sec	4 min and 12 sec	2 sec
4 sec	9 min and 55 sec	4 sec
8 sec	18 min and 33 sec	6 sec
100 sec	Memory error	58 sec

5.4 shows that the analytical model can be simulated in a much shorter period of time compared with the SimPowerSystems model.

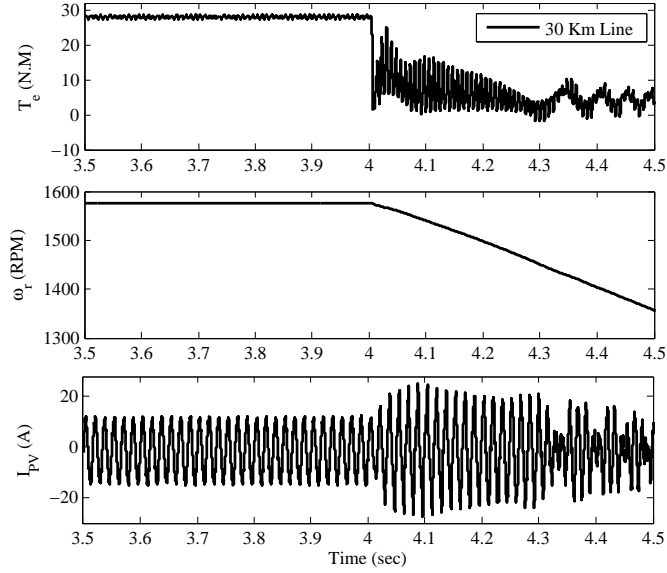


Figure 5.13. Simpowersystems simulation results for the effect of grid line length increase, (a) torque (b) rotating speed (c) instantaneous current from PV.

5.5 Conclusion

In this chapter, a dynamic phasor-based model was derived for an unbalanced distribution system consisting of a single-phase PV, a three-phase induction machine, three phase resistive load, and a three-phase power factor correction capacitor. The model is capable of fast time-domain simulation and small-signal analysis. The model's accuracy in capturing time-domain dynamics has been validated by Matlab/SimPowerSystems based models. The model's capability of small-signal analysis was also demonstrated. The eigenvalue analysis results corroborate with the time-domain simulation results in Matlab/SimPowerSystems.

Table 5.5. Parameters of the induction machine

Total capacity	5.5 kVA
Nominal voltage	400 V
Frequency	60 Hz
R_s	2.52 Ω
R_r	2.67 Ω
X_{ls}	3.39 Ω
X_{lr}	3.39 Ω
X_M	197 Ω
J	0.486 $kg.m^2$
P (poles)	4

Table 5.6. Parameters of the PV

Total capacity	2000 W
Frequency	60Hz
L_a	0.01 H
L_b	0.02 H
Cap	3 μH
$K_p(PLL)$	180
$K_i(PLL)$	3200
$K_p(PR)$	200
$K_i(PR)$	1500

Table 5.7. Line data of the network

Line No	Line Type	Z (Ω/km)	Length(m)
1	Z_{Grid}	0.579+j1.75	105
2	Z_{IM}	0.497+j2.47	105
3	Z_{PV}	0.462+j0.564	30

CHAPTER 6

PREDICTION AND OPTIMIZATION CONTROL FOR A MICROGRID

Energy storage systems have been used in utility systems to mitigate the intermittent nature of the renewable energy sources and provide desired demand response to utilities. In this chapter, operation and control of a microgrid, particularly a battery system, will be investigated.

6.1 Introduction

For battery converter control, research has been conducted in the literature to investigate converter control's role in achieving power control at the grid-connected mode and voltage/frequency control during the autonomous mode [73]. Previous work [74] designed battery management system for battery converter control by considering the state of the charge (SOC) of the battery. In addition, previous work [75] addressed the synchronizing issues of battery converter control during the transients of microgrid mode switching. The major test and validation tools for converter control are based on time-domain simulation. Simulation tools such as PSCAD and Matlab/SimPowersystems are often employed. Real-time digital simulation is also adopted to conduct time-domain simulation for very large models in real-time for up to hours [76].

Converter control focuses on dynamic responses of short-time scales such as tens of seconds. Operation problems or renewable intermittent mitigation problems focus on a much longer time scales such as sub-hour or hours. Given the varying outputs from wind and solar, the role of energy storage systems includes storing extra energy and release energy at a needed time. Due to the capacity limits of energy storage systems, it is more reasonable to operate a battery considering multi-time horizons (hourly based values) instead of operating a battery just based on the current horizon.

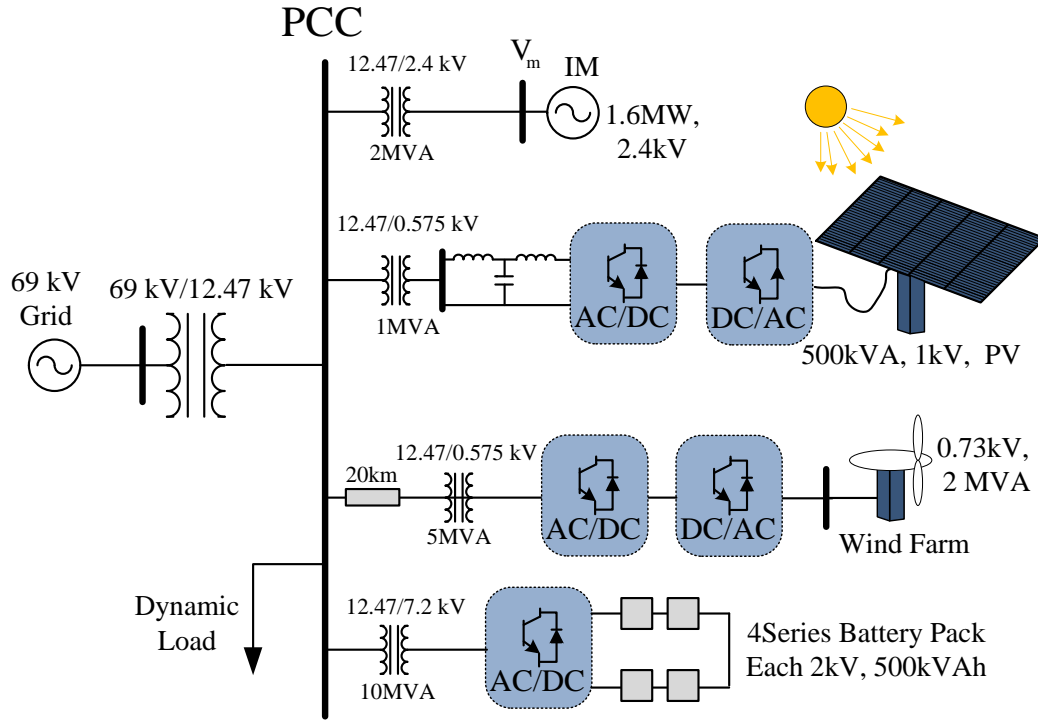


Figure 6.1. Test system.

Research on how to dispatch a battery while considering the uncertainty of wind and solar resulted in many types of optimization problem formulation. For example, a stochastic programming problem is formulated in [77, 78]. Model Predictive Control (MPC) problems have been formulated to find battery dispatch pattern [79, 80]. Model predictive control has two components: prediction and multi-horizon optimization. First, prediction of wind, solar or load demand of a microgrid is carried out for the desired time-horizons, say 24 hours. Next, a 24-horizon optimization problem is formulated to find the best dispatch schedule of a battery for the next 24 horizons based on the prediction. Only the dispatch schedule of the current step will be applied. When time evolved to the next time step, prediction and optimization will be carried out again.

In optimization problems, system short-time scale dynamics are usually ignored at the both problem formulation stage and validation stage. For example, among the above cited literature, few have carried out tests in detailed-dynamic-model-based simulation. Only [79] carried out time-domain simulation using PSCAD. However, in such simulation, converter switching and their con-

trols were ignored and represented by a gain block only. In addition, PSCAD simulation is not a real-time simulation and cannot reflect if an optimization scheme can be found in real time. In order to verify the optimization and control schemes, real-time simulation based tests will be more convincing. Such tests were carried out in [81] to verify an optimal battery schedule algorithm to mitigate PV intermittence. The dynamic programming technique is used to solve the algorithm within one minute. The simulation model for validation does not include power electronic switching and converter control.

In this chapter, real-time simulation including converter dynamics will be carried out for verification. Such verification will be closer to the real-world than the verification conducted in [81].

There are two reasons to carry out the upper-level optimization more frequently instead of every hour: (i) The prediction will be more accurate if the time horizons are near to the current stage. (ii) The power converter controls employed in microgrids can achieve fast and flexible power control compared to the traditional controls employed in power systems (e.g., OLTC). Therefore, in this chapter, dispatch for every 15 minutes for the battery is examined.

The upper-level optimization will calibrate the optimal battery dispatch level at the current step and send the power order to the battery. The lower-level converter control will follow the power order and provide the required power. The entire architecture will be tested in RT-lab based real-time simulation. Real-time simulation-based tests will not only provide high-fidelity system responses, but also examine the feasibility of the optimization algorithms by monitoring CPU usage in real time.

The contribution of the work is highlighted below.

1. Two-level design of microgrid control enables both long-term battery scheduling and fast power control.
2. A comprehensive model of a microgrid including converter dynamics is used in real-time simulation for optimization algorithm verification. Such verification is close to the real-world scenario due to the high fidelity model. In addition, the feasibility of the optimization algorithm can be well tested.

6.2 Test System

The community power system is a grid connected Microgrid which connects the 69 kV grid to the Point of Common Coupling (PCC) of the 12.47 kV microgrid via a transformer. The microgrid structure consists of a 500-kVA PV generation system, and 2 MVA wind farm based on Permanent Magnet Synchronous Generator (PMSG) which is connected to the PCC via a 20 kM transmission line. Furthermore, four series battery pack, each with 2kV dc voltage, 500 kWh energy capacity is also connected to the microgrid PCC via step up transformers. The internal demand of the microgrid consists of 1 MW dynamic load and a 1.6 MW induction machine. The system is shown in Fig. 6.1. In this system, power electronic converter switching details and controls are all included. Wind and PV dynamics are also included. The dynamic load is considered as a programmable load with controllable active and reactive power commands. The battery dynamic model follows [74]. The detailed system modeling information can be found in this report [82].

6.3 ARMA Model for Estimation of Load and PV

The ARMA model or Box-Jenkins model is one of the common time series statistical models for solving problems with large amounts of observed data in past [83]. The general ARMA model has two parts; Auto Regressive (AR) and Moving Average (MA) and the model for forecasting a signal at time t is expressed by:

$$Pred(t) = \sum_{i=1}^p \alpha_i Pred(t-i) + \sum_{j=1}^q \beta_j X(t-j) \quad (6.1)$$

where $Pred(t)$ in this study is the output power of PV and Load output, p is the order of AR process, and q is the order of MA process. Furthermore, α_i and β_j are coefficients of AR and MA processes, respectively. Finally, $X(t)$ is a randomly produced white noise with zero mean value and unity variance. Generally, in order to derive the ARMA model properly, historical data for a long time should be provided. In this study, historical data for the last three months is used to derive the coefficients of ARMA model. The main step for identifying the ARMA model is to identify the

p and q orders with trial and error method. Next step is to determine the coefficients α and β . Step by step procedures to derive the ARMA model is illustrated in Fig. 6.8. It can be observed that

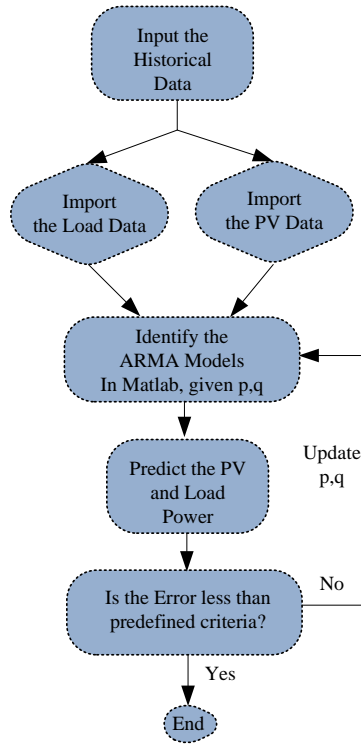


Figure 6.2. Step by step procedure to derive the ARMA model for load and PV.

in the first step, historical data for the load and PV are used as two inputs for the ARMA model. The modeling is done separately, it means that for each prediction model (PV and Load) different ARMA model is derived and different orders will be used. The data is up to the last three months hourly based for PV output power and load power. In the next step of identifying the ARMA model, the historical data is used to simulate the hourly distribution of PV and load output power. The nominal parameters of PV and load are given in Section II. Next step is to derive the ARMA model coefficients for given p and q . Identification of ARMA model coefficients is then carried out by the MATLAB inbuilt command. After deriving the ARMA model, the next step is to forecast the future values. The next state update is easily calculated by [83]:

$$Pred(t+1) = \sum_{i=1}^p \alpha_i Pred(t-i) + \sum_{j=1}^q \beta_j X(t-j) \quad (6.2)$$

where $Pred(t+1)$ is the predicted value of PV power or load power in the next hour. The last step is to examine the performance of the derived ARMA model. To achieve the best performance, actual data should be compared with the forecasted value as an error. If the calculated error is less than the predefined value, the accuracy of the ARMA model is acceptable, otherwise, system's order should be change and model derivation should be performed again. Normally, absolute value of mean squared error is used as an index for calculating the error between prediction and actual data. Obtained ARMA model parameters for PV and load are illustrated in Table 6.1. For the PV ARMA model, p is 12 which means 12 previous hourly data will be used to predict next hour PV power. In order to estimate the second hour first hour prediction and 11 previous hourly data will be selected.

Table 6.1. Obtained ARMA model parameters for PV and load

DG	p, q	α	β
PV	12, 1	$[-1.94, 0.977, -0.007, 0.025, 0.070, -0.077, -0.024, -0.093, -0.027, 0.046, 0.128, -0.132]$	-0.987
Load	11, 1	$[-2.453, 2.040, -0.696, 0.147, 0.075, -0.056, -0.046, -0.037, -0.215, 0.501, -0.259]$	-0.909

6.4 Upper-Level Model Predictive Control Based Optimization

At the grid-connected operation mode, the battery is operated for peak shaving in order to compensate the highly intermittent nature of PV, wind and the dynamic load. The battery must be operated efficiently to keep the power output of the microgrid ($P_{\mu G}$) on its predetermined reference value. The decision variable of the optimization problem is battery discharging power (P_{batt}). In optimization process, it is required to consider the power and energy limits of the battery. As the energy stored in the battery is the integration of the battery power during the

time, the optimization problem must be solved in a horizon of time considering the prediction of PV generation (P_{PV}^{pred}) and load power output (P_{load}^{pred}). At each time step, the predicted values are updated based on the real-time measurements. Algorithm 1 presents the algorithm designed for the peak shaving process. Fig. 6.3 also illustrates how the optimization machine, prediction updating module, and RT-LAB communicate with each other.

6.4.1 The Optimization Problem

The objective of battery operation is to minimize the error between the power output of the microgrid and its reference value for the next optimization horizon as (6.3). The optimization problem which is solved at time step t is described as below.

$$\min \quad SSE(t) = \sum_{k=0}^{h-1} (P_{ref}(t+k) - P_{\mu G}(t+k))^2 \quad (6.3)$$

$$\text{s.t.} \quad \forall k \in [1, h-1]$$

$$P_{\mu G}(t) = P_{PV}(t) + P_{wind}(t) + P_{batt}(t) - P_{load}(t) \quad (6.4)$$

$$\begin{aligned} P_{\mu G}(t+k) &= P_{PV}^{pred}(t+k|t) + P_{wind}^{pred}(t+k|t) \\ &+ P_{batt}(t+k) - P_{load}^{pred}(t+k|t) \end{aligned} \quad (6.5)$$

$$E_{batt}(t+k+1) = E_{batt}(t+k) - P_{batt}(t+k)\Delta t \quad (6.6)$$

$$-\overline{P_{batt}} \leq P_{batt}(t+k) \leq \overline{P_{batt}} \quad (6.7)$$

$$\underline{E_{batt}} \leq E_{batt}(t+k) \leq \overline{E_{batt}} \quad (6.8)$$

where t , $t+k$, and h denote the current time step, next k^{th} time step from current time t , and the length of the optimization horizon, respectively. (6.5) defines the total power output of the microgrid to the main grid. (6.6) determines the relationship between the battery discharging power and energy stored in the battery. (6.7) and (6.8) consider the battery power and energy limitations. $P_{PV}^{pred}(t+k|t)$ and $P_{wind}^{pred}(t+k|t)$ represent the predicted power generations of PV and wind at time $t+k$ given their actual measurements until time t . Parameters of the optimization problem are shown in Table 6.2.

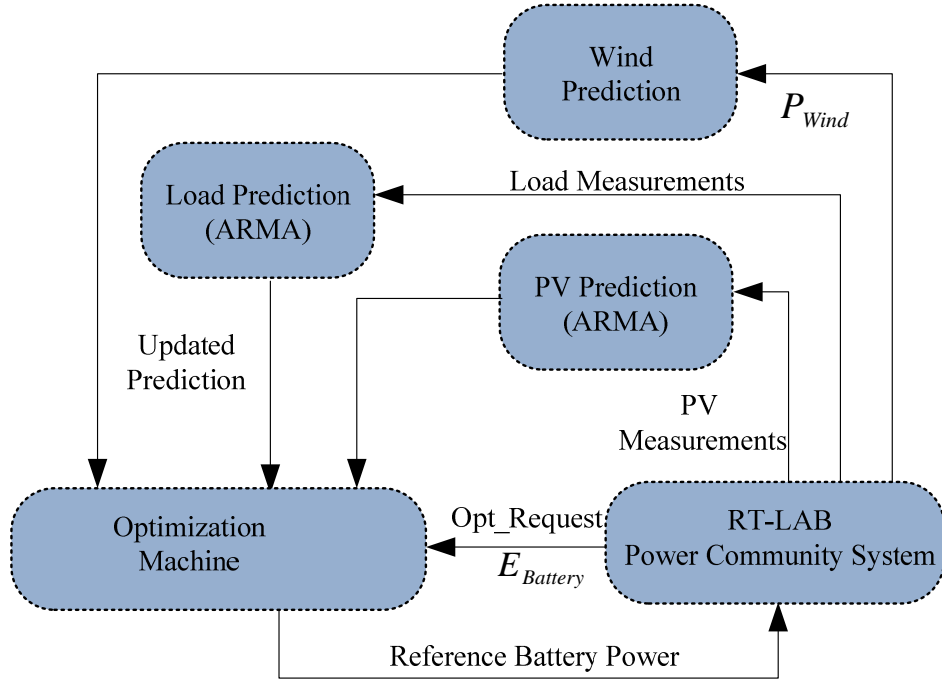


Figure 6.3. Optimization procedure for real-time digital simulation of the microgrid.

Table 6.2. Parameters of the optimization problem

Parameter	Value
\overline{P}_{batt}	2 MW
\overline{E}_{batt}	1.9 MWhr
E_{batt}	0.2 MWhr
h	4 hours

6.4.2 Prediction Procedure

At each time step t the prediction module updates the predicted values for PV output (P_{PV}^{pred}), wind prediction (P_{wind}^{pred}) and load (P_{load}^{pred}) for the time steps $\{t+1, t+2, \dots, t+h-1\}$. PV and Load prediction have been done utilizing proposed ARMA models. Actual PV data recorded from USF power group SEEDS2 project has been used for training and testing the ARMA model. Training data are selected from January 2nd to April 2nd of year 2014 as presented in Fig. 6.7. Testing data is selected between April 9th to 11th of the data gathered from USF St. Petersburg airport site as presented in Fig. 6.8. Real load data are obtained from [84]. Three months of data are used for training the ARMA model. A different statistical approach is applied for wind generation prediction.

$$k_{wind}(t) = \frac{P_{wind}(t)}{P_{wind}^{ref}(t)} \quad (6.9)$$

$$P_{wind}^{pred}(t+k|t) = k_{wind}(t)P_{wind}^{ref}(t+k) \quad (6.10)$$

where $P_{wind}(t)$ is the actual value measured for wind power generation at time t . The reference pattern of wind generation P_{wind}^{ref} is produced based on a random process. The prediction module compares the wind power measurements with its reference patterns to define its scale factor, k_{wind} . This scale factor is used to update the prediction of wind farm generation levels.

Applying (6.9) and (6.10) to (6.5) leads to a new expression for the prediction:

$$\begin{aligned} P_{\mu G}(t+k) &= P_{PV}^{pred}(t+k|t) + k_{wind}(t)P_{wind}^{ref}(t+k) \\ &+ P_{batt}(t+k) - P_{load}^{pred}(t+k|t) \end{aligned} \quad (6.11)$$

The entire algorithm is summarized in **Algorithm 1**. The optimization problem formulated is a linear programming problem and will be solved by Matlab toolbox CVX [85].

Algorithm 1 Optimization of Battery Operation at time step t

Estimate the energy stored in the battery based on measurements $E_{batt}(t)$.
 Measure PV output power and update the predictions using ARMA model.
 Measure Load power and update the predictions using ARMA model.
 Measure wind farm generation and update the predictions according to the wind generation pattern.
 Solve (6.3) considering the constraints (6.6)-(6.8).
 Apply $P_{batt}(t)$ to the system.
 Wait for the optimization request signal.

6.5 Lower-level Converter Controls

The battery system can be operated at either the power control or the voltage/frequency control modes. The former mode can be used when the microgrid is grid-connected and the second control mode is applied when the microgrid is at its autonomous mode. An equivalent model of a voltage source converter (VSC) connected to ac sources is shown in Fig. 6.4.

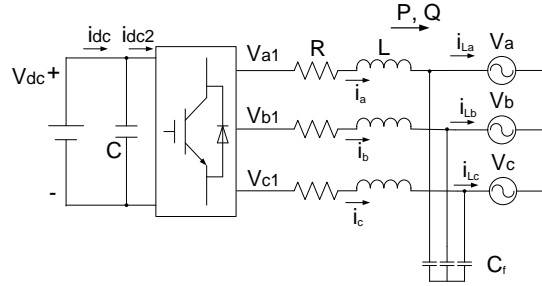


Figure 6.4. Equivalent model of a voltage source converter connected to ac source.

Assuming that the operating condition is three-phase balanced, then the space vector variables for the current (i_p where $p = a, b, c$) and voltages (v_{p1} and v_p) relationship can be expressed as follows.

$$\vec{v} = \vec{v}_1 - R \vec{i} - L \frac{d\vec{i}}{dt} \quad (6.12)$$

where $\vec{\cdot}$ represents the space vector ($\vec{f} = \frac{2}{3}f_a + e^{j2\pi/3}f_b + e^{-j2\pi/3}f_c$).

For three-phase balanced variables with a constant synchronous frequency ω_s , $\vec{f} = \bar{F}e^{j\omega_s t}$, where \bar{F} is called a complex vector, which is be a constant vector at steady-state. (6.12) can be

represented completely by complex vectors as presented in (6.13).

$$\bar{V} = \bar{V}_1 - R\bar{I} - L\frac{d\bar{I}}{dt} - j\omega_s L\bar{I} \quad (6.13)$$

where $\bar{F} = f_d + jf_q$.

Therefore the VSC model presented in Fig. 6.4 can be modeled in a synchronous reference frame as in (6.14) and (6.15),

$$v_{d1} = -(Ri_d + L\frac{di_d}{dt}) + \omega_s Li_q + v_d \quad (6.14)$$

$$v_{q1} = -(Ri_q + L\frac{di_q}{dt}) - \omega_s Li_d \quad (6.15)$$

$$C_f \frac{dv_d}{dt} = \omega_s C_f v_q + i_d - i_{Ld} \quad (6.16)$$

$$C_f \frac{dv_q}{dt} = -\omega_s C_f v_d + i_q - i_{Lq} \quad (6.17)$$

where v_d , v_q , v_{d1} , and v_{q1} represent the d and q components of the point of common coupling (PCC) voltage (v_a, v_b, v_c) and VSC output voltage (v_{a1}, v_{b1}, v_{c1}), respectively, and i_d, i_q, i_{Ld} and i_{Lq} represent the d and q components of the current flowing to the VSC (i_a, i_b, i_c) and current flowing from the PCC (i_{La}, i_{Lb}, i_{Lc}), respectively.

The representation of the system model in the synchronous reference frame helps derive the control schemes. The control system of a VSC consists of two loops: inner current control loop and outer control loop. The outer control loop is active power control loop when the microgrid is grid-connected. When the battery is supplying an autonomous microgrid, the outer control loop will be switched to ac voltage and frequency control. Inner current control can be derived based on the system model (6.14) and (6.15) [86, 87, 88, 89].

6.5.1 Power Control Loops

If the d -axis of the synchronous frame is aligned with the complex vector of the grid voltage \bar{V} , then $v_q = 0$. The complex power flowing to the grid before the capacitor can be expressed as:

$$P + jQ = (v_d + jv_q)(i_d - ji_q) \quad (6.18)$$

Therefore $P = v_d i_d$ and $Q = -v_d i_q$. If the grid voltage is assumed to be constant, the active power sent from the converter to the grid is dependent on the d -axis current i_d only. The reactive power sent from the converter to the grid is dependent on the q -axis current i_q only. Decoupled PQ control can be realized by controlling dq -axis currents respectively. Fig. 6.5 presents the outer power control loops where P and Q are measured and compared with their references. The errors are passed through PI controllers respectively to generate desired dq current references. Inner current controls will track these reference values in a much faster fashion. Therefore, the bandwidth of the power control loop will affect the response time of the battery system.

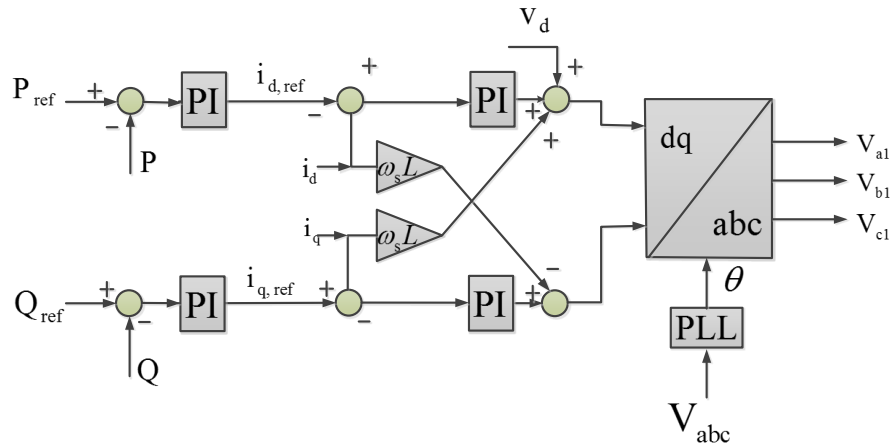


Figure 6.5. Power control strategy of the inverter.

6.5.2 Inner Current Control Loops

The objective of the inner current control is to track the current references by adjusting the converter output voltage. The control is realized in the dq reference frame through PI controls, cross coupling and feed-forward blocks [73].

Based on the system model presented in (6.14) and (6.15), fictitious plant inputs $u_d = v_{d1} - v_d - \omega_s L i_q$ and $u_q = v_{q1} + \omega_s i_d$ can be assumed. Therefore the plant models become:

$$\frac{i_d}{u_d} = \frac{1}{R + Ls} \quad (6.19)$$

$$\frac{i_q}{u_q} = \frac{1}{R + Ls} \quad (6.20)$$

For each plant, we can design a PI controller to track the reference current. To generate the desired converter voltage, cross coupling and feed forward blocks are then needed to find v_{d1} ($v_{d1} = u_d + \omega_s L i_q + v_d$) and v_{q1} ($v_{q1} = u_q - \omega_s L i_d$) as shown in Fig. 6.5. The dq -axis voltages are then converted to the desired abc voltages. Through PWM or space vector PWM switching schemes, the converters will generate voltage with fundamental waveforms same as v_{a1} , v_{b1} and v_{c1} . The detailed design procedure can be referred from [73].

6.6 Tests

Case studies are included in this section. The microgrid is modeled in real-time simulator (RT-LAB) and the prediction and optimization process are carried out in MATLAB. The interface between Matlab and RT-LAB is also created. The Matlab CVX optimization toolbox is in charge of the optimization process. The optimization result (Battery power in this case) is sent to the Microgrid model in RT-LAB in order to optimize the entire system and minimize the objective function. Such an interface is shown in Fig. 6.6. It should be noted that the measured data is also sent from the Microgrid model to the prediction process for predicting the PV, load and wind power for the next three hours.

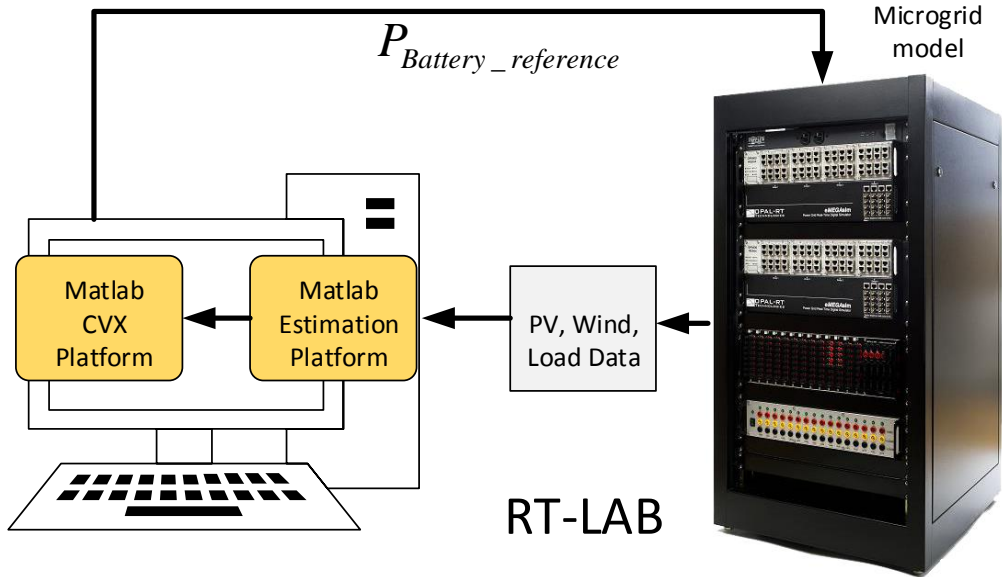


Figure 6.6. General structure of implementation of the proposed algorithm.

6.6.1 Test 1: Prediction Validation in Simulink

The three months data for PV prediction is obtained from SEEDS project sponsored by Duke Energy. Fig. 6.7 shows the PV data captured for three months, which is used for deriving the ARMA coefficients.

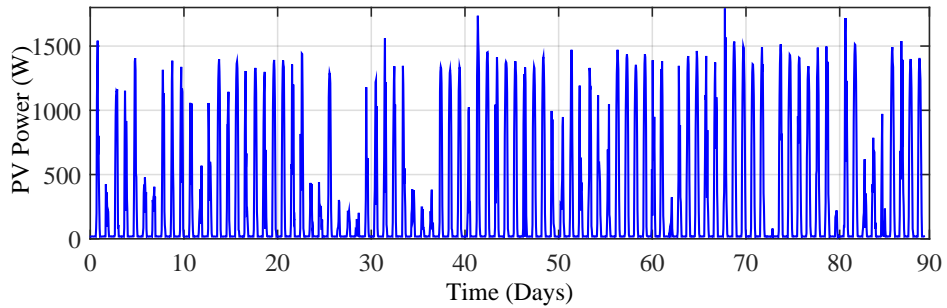


Figure 6.7. Three months real data captured by PV for SEEDS project.

In-order to test the ARMA prediction, PV estimation process for three days is illustrated in Fig. 6.8. The prediction is carried out for the next three hours. As it is illustrated, the prediction process accuracy is low for 3rd hour PV power prediction.

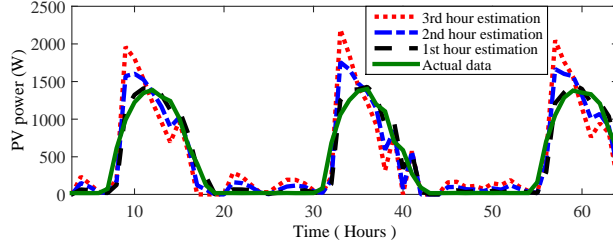


Figure 6.8. Prediction of PV power by ARMA model for different hours ahead.

6.6.2 Test 1: Peak Shaving at Grid-Connected Mode

In this case study, the MPC is designed considering next 4 hours. Every 10 minutes, the prediction of PV, load and wind generation will be updated and the optimal dispatch of the battery will be decided based on the optimization algorithm. This 4 hour horizon will be moved every 10 minutes creating a moving horizon optimization. Fig. 6.9 depicts the PV, load and wind power outputs for a 24-hour simulation. The real-world PV data from SEEDS2 project located in St. Petersburg, FL has been used to derive the PV power pattern in this case and load data simulated from [84], while the wind power pattern has been generated via a random process in MATLAB. Since 4-hours horizon is considered in the upper level optimization, the PV, load and the wind power have to be forecasted for the next four hours. It is assumed that the current measured value will be kept for one hour, next three hours of PV and load powers are predicted using the proposed ARMA model.

The upper and lower limits of the SOC of the battery have been selected as 90% and 10% respectively. Thus, the maximum and minimum energy stored in the battery is 1.8 and 0.2 MWh. Moreover, the maximum battery power is 2 MW. The optimization problem is solved for 4-hours time horizons. In RT-LAB simulation, every minute in the real world is represented by 4 seconds to reduce the simulation time. The optimization procedure is requested every 10 minutes. The model is to be run for 1 hour and 36 minutes to simulate a 24-hour operation of the microgrid.

Fig. 6.10 shows the power output of PV, load and wind versus PV, load, wind and battery. It illustrates how the battery contributes to the microgrid operation for peak shaving. According to the results, the battery could not completely compensate the deviation of the PV, load and wind

output from power reference point. The capacity of the battery that has been utilized during the simulation is presented in Fig. 6.11.

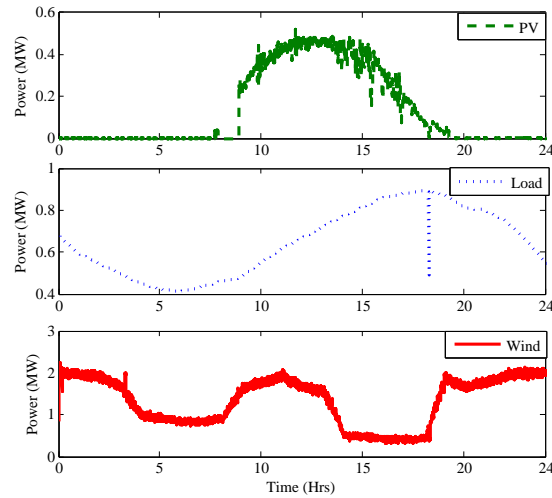


Figure 6.9. Power generation from each DG.

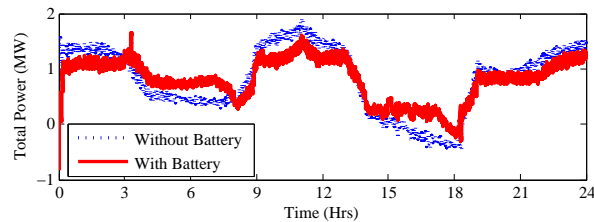


Figure 6.10. Total dynamic power contribution in the microgrid with and without battery.

6.6.3 Test 2: Sensitivity Analysis of Battery Size

In this case sensitivity analysis is conducted to validate the effect of battery size on microgrid performance. Two different battery sizes are considered in this case which are 4 MWh and 10 MWh. Fig. 6.12 shows the effect of different battery size on microgrid power. When there is no battery, the microgrid power will face with a lot of changes during the time. However, by adding the battery, the microgrid power will be smoother. It is also noted that when the battery power is increased to 10 MWh, microgrid power is more flat because the battery has compensated using its higher capacity.

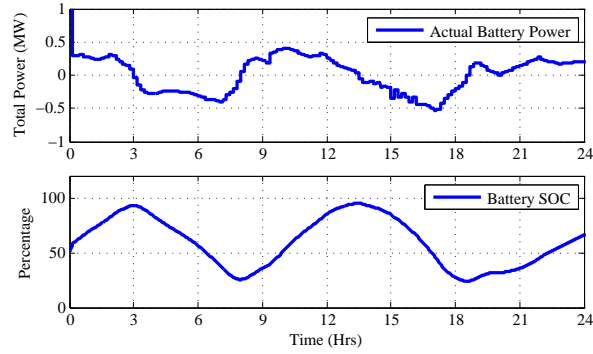


Figure 6.11. Battery power and energy stored in the battery.

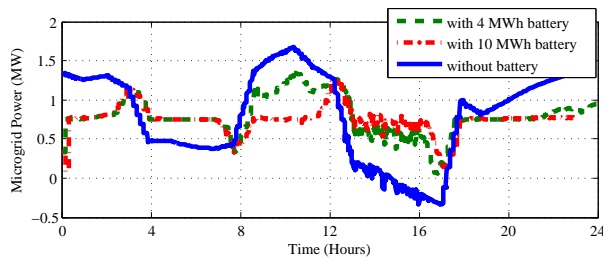


Figure 6.12. Effect of battery size on microgrid total power.

Fig. 6.13 shows the comparison between total power without battery and battery power in two cases. It is observed that when there is a 10 MWh battery in the system, the battery can compensate the microgrid power. Here, the system power represents the power exported to the main grid and the battery power represents the generated power from the battery. Therefore, negative sign of the battery power means the battery is being charged.

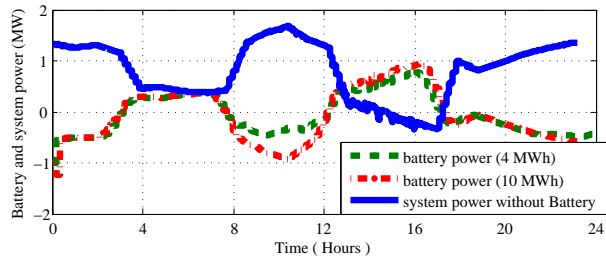


Figure 6.13. Comparison between 5 MWh and 10 MWh battery for total microgrid power.

6.6.4 Test 3: Real-time Simulator Performance

The third case is carried out to investigate the performance of real-time simulations for optimization algorithms. In order to evaluate the real time performance in RT-LAB simulation, every minute in the real world is represented by 60 seconds which exactly provides real-time results. The optimization procedure is requested every 10 minutes and RT-LAB simulation step size is set to $25 \mu s$. Performance of battery energy storage system in following the reference power is shown in 6.14. In order to compare the RT-LAB speed, the second sub-figure shows the response time of RT-LAB to the power reference change. The response of the battery model in RT-LAB is observed as 4 seconds, which means the bandwidth of the battery power control is 4 seconds.

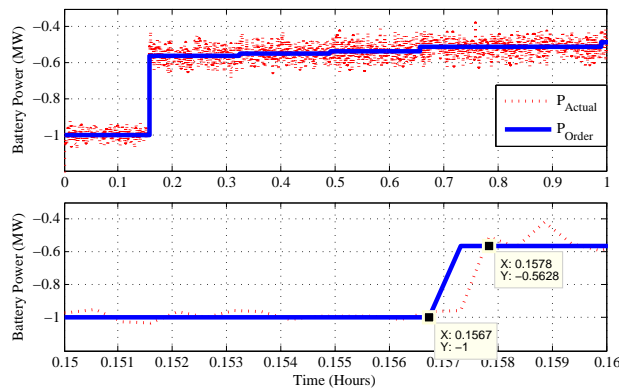


Figure 6.14. RT-LAB performance in tracking the reference battery power.

Fig 6.15 shows the battery active power, reactive power and output voltage for 6 hours. It is observed that the battery power command can be successfully followed by the proposed controller. Furthermore, the reactive power reference is set to zero, which is kept constant during the optimization process and the voltage is also kept constant at the rated value (13.8 kV).

6.7 Conclusion

A two-level optimization and control architecture for a microgrid has been designed and tested in RT-lab based real-time digital simulation. During the grid-connected mode, at the upper-level for every 10 minutes, wind power, load and PV power output for four hours time horizon are estimated. Then the battery dispatch profile for the next 4 hours is determined with SOC limits considered.

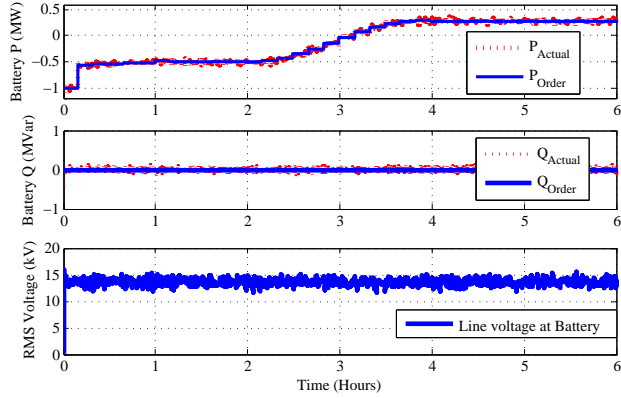


Figure 6.15. Battery measurements and commands in RT-LAB.

The current step battery dispatch level will be sent to the battery converter power control as the power order. The lower-level converter control makes sure the battery will follow the command. Real-Time simulation of a Microgrid including detailed PV, wind and load structure is carried out in RT-Lab to test the proposed optimization algorithm. Simulation results demonstrate the effectiveness of the two-level optimization and control architecture. Higher Battery energy storage systems can be implemented to fully compensate the intermittent nature of the dynamic DGs. The proposed upper level control can be adopted to the future USF St. Petersburg microgrid which consists of 100 kW PV station, 200 kW energy storage system, and controllable loads.

Table 6.3. Parameters of the system

Fig. 4	R	0.01Ω
	L	$0.012 H$
	C_f	$1 \mu F$
Fig. 5 (PQ loop)	K_p	0.001
	K_i	0.5
Fig. 6 (VF loop)	K_p	1.673
	K_i	374.75
Figs. 5-6 Current loop	K_{pi}	5
	K_{ii}	50

CHAPTER 7

MICROGRID OPERATION WITH INTERMITTENT LOADS

This Chapter ¹ presents, modeling and simulation of intermittent loads in a Microgrid.

7.1 Introduction

Microgrid concept has attracted much attention today, due to its reliability, efficiency and low operation cost. Renewable Energy Sources play a major role in this concept and due to the intermittent nature of renewable energy such as wind and solar, operational implications will occur. Certain loads such as pulse power loads (PPL) and electric cars [90] will increase these implications. Hence the system impact of these kinds of loads should be studied in order to provide better solutions. Among these loads PPLs have a major effect on the stability of the system due to their highly intermittent nature.

The PPLs are largely employed in areas of high power radars, lasers, high energy physics experiments and weapon systems such as rail guns [91, 92]. The peak power of a pulse load can vary from several hundred kW to several hundred MW and the time duration is typically from microseconds to seconds[92, 93]. Some PPLs are directly connected to the main grid. But if the PPL power demand cannot be met by a direct connection due to the impact on the power quality of the system, PPL will be connected to an energy storage device, generally a capacitor which has to be charged within a certain amount of time. Then the storage will be discharged rapidly providing the power to the pulsed load.

If the PPL is connected to the power system through a capacitor, the main method of controlling above effects is controlling the charging current of the storage element. Some work[94, 91] has been

¹This section is based on the work published in journal of Technology & Innovation 14.2 (2012): 167-178. Permission is included in Appendix A.

done related to this. They have proposed Limit Based Control (LBC) [94], Trapezoidal Based Control(TBC) [94] and Profile Based Control (PBC) [91] which will reduce the impact of PPLs on the microgrid power system.

Since the Renewable Energy Sources (RES) play a major role in a microgrid, Power Electronic Converters are necessary parts of a microgrid. Back to back converters hugely employ in wind power generation either with Doubly Fed Induction Generators (DFIG) or Permanent Magnet Synchronous Generators (PMSG) while inverters are frequently used with battery storage systems and solar power. Though many work[91, 92, 93, 95, 94] have been done related to PPL impact, most of them [91, 94, 93] consider the PPL connected to a shipboard power system which includes a single generator unit and propulsion system as the main load. Therefore an investigation has to be done to see the PPL impact on the stability of a microgrid with power electronic converters and how these converters can participate to improve the system stability. Hence for the proposed work, a microgrid with Voltage Source Converter (VSC) based inverter and a synchronous generator are considered in order to provide a better approach towards the smart grid. Microgrid system models used in [96] and [91] are considered as major references when implementing the study system for this work. Microgrid behavior under different control architectures is discussed in this chapter.

The work done in [91] considers the impact of a PPL load on the system voltage profile only. For the work here, the impact on both the voltage and the frequency of the microgrid system is considered.

7.2 Power Management in Microgrid Systems

Architecture of the microgrid can be explained in two levels, Component Level and the Management Level (Control Level). The microgrid is in fact a subpart of a power distribution system. It consists of Distributed Energy Resources (DERs) and loads. DERs include Distributed Generation (DG) units and Distributed Storage (DS) units. Loads include residential type loads, commercial type loads and industrial parks. Microgrid is connected to the utility grid through Point of Common Coupling (PCC) which is located at the low voltage bus of the substation transformer.

Two control strategies are generally exercised in Microgrid Control and they are centralized control and decentralized control. In centralized control, Microgrid Central Controller (MCC) is responsible for a major part of controlling. It issues the commands such as power production set points to the DERs and set points for loads to be served and shed. Function of the Local Controllers (LCs) in centralized control is, following the MCC instructions. The main disadvantage of the centralized control is the high cost involves with the fast communication system. This problem can be avoided by occupying decentralized control in power management. Droop control is an example of a decentralized control [2, 3, 4] and will be discussed in the following paragraphs.

In central control architecture, the inverter's active power and reactive power references are set by the central controller. These values are set according to the power requirement of the PPL. This can be achieved through fast communication between Microgrid Central Controller (MCC) and Local Controllers (LCs) of the PPL and the inverter.

In decentralized control, the power references are set according to the local measurements of frequency and voltage. Control block diagram of the inverter is presented in Fig.7.1. Reference values for the active and reactive power is calculated according to the droop characteristics of the inverter [96].

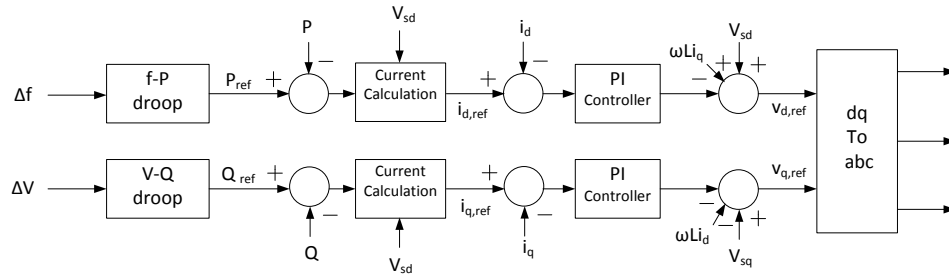


Figure 7.1. Control diagram of the inverter.

Assuming the slope of the f - P characteristics of the inverter is R_f , the active power change of the inverter for a small change of frequency is given by,

$$\Delta P = -\frac{1}{R_f} \Delta f \quad (7.1)$$

Similarly for a small change in voltage, the required reactive power is given by,

$$\Delta Q = -\frac{1}{R_v} \Delta V \quad (7.2)$$

where R_v is the slope of the V - Q characteristics.

Using the droop control, a VSC interfaced distribution energy resource can respond to the local measurements and adjust its power output automatically.

7.3 Study System

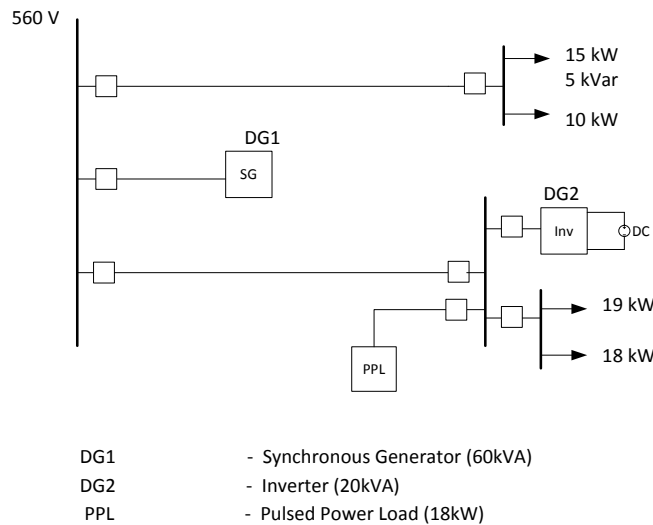


Figure 7.2. Single line diagram of the microgrid.

Fig. 7.2 shows the single line diagram of the system which is built for the case study here. It contains two DG units, including a diesel engine synchronous generator and a converter-interfaced DER. The system is very similar to the shipboard power system employed in [91] except for the fact that the proposed study system has a VSC based inverter as a DER. The rated voltage of the system is 560V. This system includes 60 kVA Synchronous generator and 20kVA inverter based DER. It is assumed that in normal operation the inverter is operating at 10kW and 5kVar. The system consists of 52 kW and 5kVar constant power loads and a 18 kW peak power pulsed power load.

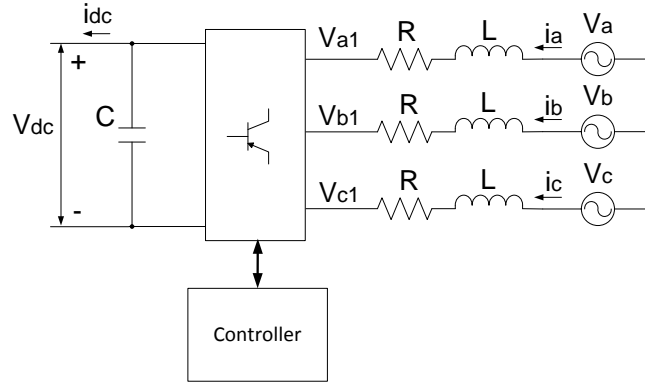


Figure 7.3. Schematic diagram of the VSC model.

7.3.1 Diesel Engine Synchronous Generator

Synchronous generators in the proposed study system are driven by diesel engines. The diesel generator includes three main parts, which are synchronous generator, governor control and the excitation system.

The synchronous generator used for the proposed study is a salient-pole type which is implemented as a model in PSCAD library. Woodward governor model which is a speed governor typically employed with synchronous generators[97] is used in-order to provide torque input to the synchronous generator. The input to the governor control is the offset of the actual speed and the reference speed and the result is a controlled output torque, which will be sent to the input torque of the synchronous generator in-order to minimize the offset. Since the reference speed is set according to the system frequency, which is 60-Hz for the proposed study system, Governor control is responsible for keeping the system frequency within the limits.

Automatic Voltage Regulator (AVR) is employed to maintain a constant voltage at the terminals of the synchronous generator. This will control the excitation current of the machine, consecutively keeping the terminal voltage at the rated value.

7.3.2 VSC Based Inverter

Since Converter-interfaced DERs are generally connected to a rectifier, for simplicity a DER can be modeled with a constant dc source connected to an inverter which is based on VSC topology

[98]. The schematic diagram of a VSC model is presented in Fig. 7.3. Here the resistance, R and the inductance stand for equivalent resistance and inductance between the converter and the grid. V_{dc} represents the dc voltage while v_{a1} , v_{b1} and v_{c1} stand for the ac voltage generated by the VSC at nominal frequency. The grid voltages are symbolized as v_a , v_b and v_c . The currents denoted by i_a , i_b and i_c are flowing into the converter. Thus, they should be negative while DER provides the power to the system.

The VSC model dynamics in abc frame can be obtained by applying KCL and KVL to the system.

$$\begin{bmatrix} v_a \\ v_b \\ v_c \end{bmatrix} = R \begin{bmatrix} i_a \\ i_b \\ i_c \end{bmatrix} + L \frac{d}{dt} \begin{bmatrix} i_a \\ i_b \\ i_c \end{bmatrix} + \begin{bmatrix} v_{a1} \\ v_{b1} \\ v_{c1} \end{bmatrix} \quad (7.3)$$

Applying coordination transformation from abc to d-q reference frame,(3) can be written as

$$\begin{bmatrix} v_d \\ v_q \end{bmatrix} = R \begin{bmatrix} i_d \\ i_q \end{bmatrix} + L \frac{d}{dt} \begin{bmatrix} i_d \\ i_q \end{bmatrix} + \omega_s L \begin{bmatrix} -i_q \\ i_d \end{bmatrix} + \begin{bmatrix} v_{d1} \\ v_{q1} \end{bmatrix} \quad (7.4)$$

where ω_s is the angular frequency of the AC system. However the angle, (θ) between two reference frames is required to do the abc to d-q transformation. This can be measured using a Phase-Locked-Loop (PLL)[98, 4, 99].

The active power and reactive power flowing into the VSC inverter can be written as [100, 99],

$$P = v_d i_d + v_q i_q \quad (7.5)$$

$$Q = v_q i_d - v_d i_q \quad (7.6)$$

If the d axis component of the converter ac voltage is aligned along with its space vector, the q axis component will be zero. Hence equations (7.5) and (7.6) can be modified as,

$$P = v_d i_d \quad (7.7)$$

$$Q = -v_d i_q \quad (7.8)$$

This proves that the active power can be controlled by i_d while the reactive power can be controlled by i_q .

7.3.3 PPL Model and Control

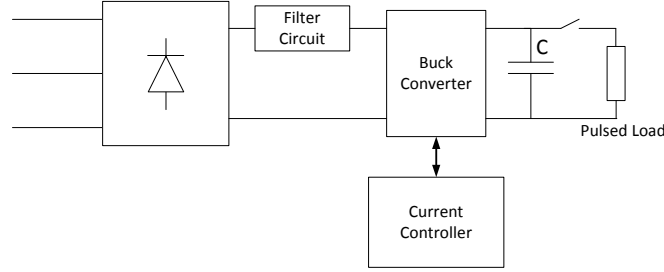


Figure 7.4. PPL model.

As mentioned earlier in this chapter a PPL can be connected to a microgrid either directly or through a storage element. In this particular study system, at steady state, the DERs are operating close to their rated power values. Consequently the system is working in its marginal conditions. Hence a directly connected PPL will cause the system to go unstable due to the total peak power demand of PPL and the constant power loads will exceed the total generating capacity. For the work here a PPL connected through a capacitor is considered since a proportional control mechanism can be employed to charge the capacitor while maintaining the stability of the microgrid system. Frequency of occurrence of the PPL depends on the application of the PPL. But it is common practice to charge the capacitor as quickly as possible [91, 93, 94].

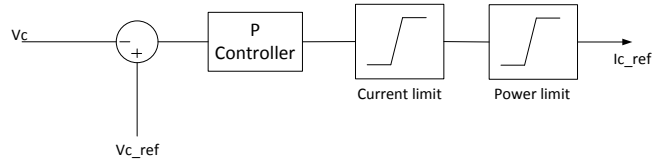


Figure 7.5. Capacitor current control (limit based control).

Fig.7.4 presents the PPL model used for the proposed case study. It consists of a three phase rectifier, a filter circuit and a buck converter. The charging current of the capacitor can be controlled

by adjusting the duty cycle of the buck converter. The control objective here is to charge the capacitor as quickly as possible while maintaining the stability of the system. Limit Based Control (LBC) control [94] is employed to achieve the above objective. The control block diagram is shown in Fig.7.5. Here current limit is set based on the maximum current capacity of the PPL rectifier and the buck converter while the power limit is set based on the maximum power transfer capability of the system.

The parameters of the PPL model are listed in Table 7.1. The parameters of the synchronous generator for the diesel engines are listed in Table 7.2. The parameters of the inverter model are listed in Table 7.3.

Table 7.1. PPL model parameters

Storage circuit parameters: $C = 2.02F$, $L = 3mH$, $R = .25\Omega$
Filter circuit parameters: $L = .113mH$, $R = .25\Omega$, $C = 1.4\mu F$

Table 7.2. Synchronous generator parameters in per unit

Inertia of the generator: $H = 3.117s$
$R_a = .0052$
$X_d = 1.014$, $X'_d = .314$, $X''_d = .28$
$X_q = .77$, $X''_q = .375$
$T'_{do} = 16.55$, $T''_{do} = 0.039$, $T''_{qo} = .071$

Table 7.3. Inverter model parameters

$V_{DC} = 2kV$, $C = 50\mu F$
Controller parameters: $kp = .01$, $ki = .001s$
Transformer parameters: $X = .1$
Line parameters: $L = .01H$, $R = .001\Omega$

7.4 Simulation Results

The proposed Microgrid is implemented using PSCAD/EMTDC software package. PSCAD model for the Microgrid is shown in Fig. 7.6 and it represents the system shown by the single line diagram in Fig. 7.2. If the Microgrid is connected to the main grid which can be considered as the infinity bus, the impact of PPL will be minimized due to the high inertia of the infinity

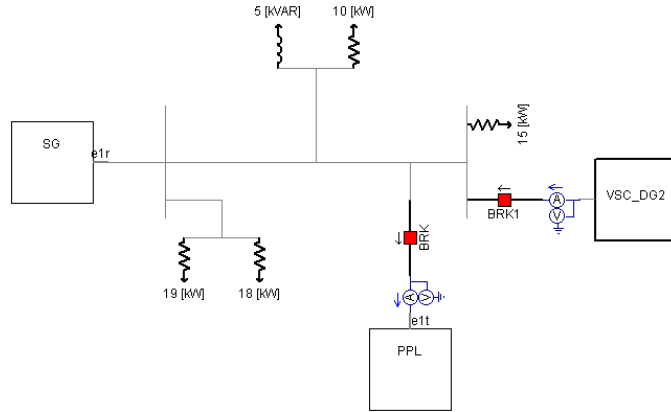


Figure 7.6. PSCAD model of the microgrid.

bus. However when the microgrid is operating in islanded mode the PPL has a considerable effect because of the low inertia of the system. Therefore the work here is focused on the impact of the PPL in islanded mode operation.

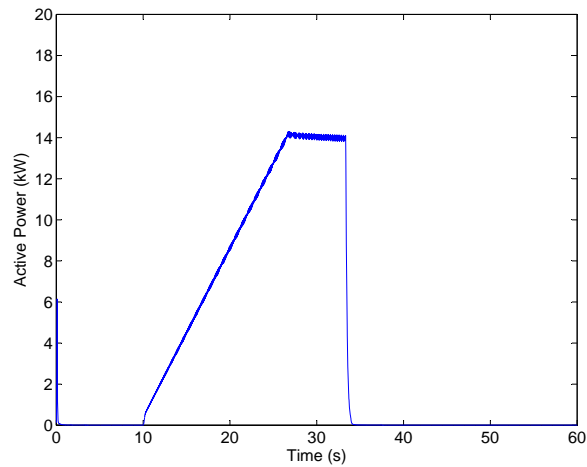


Figure 7.7. PPL power with limit based control.

Limit based control is implemented to control the charging current of the PPL storage capacitor. Only one PPL charging cycle is considered within 100-s in order to compare the system behavior for different control architectures. Fig. 7.7 shows the active power transferred into the capacitor during the charging process. Charging process starts at $t=10$ -s and stops at $t=33.4$ -s. Hence the charging time of the capacitor is 23.4-s with the limit based control. It can be seen that until $t=$

26.5-s current limit is effective and after that power limit is dominating the controlled charging current of the capacitor. Since the objective of this work is to study how to use an inverter based DER to reduce the impact of PPL load on the microgrid system stability, two main cases are considered to support that. These two cases represent the passive control and the active control of the inverter.

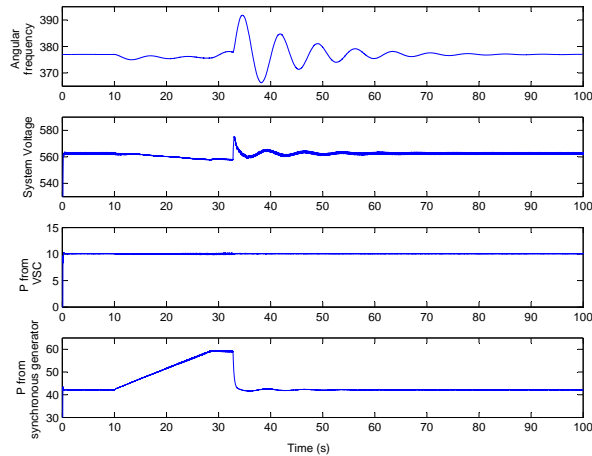


Figure 7.8. Passive control of the inverter, (a) angular frequency of the system (b) system voltage (c) active power from the inverter (d) active power from synchronous generator.

7.4.1 Passive Control of the Inverter

In this case the inverter doesn't participate in controlling frequency and the voltage of the system. It just provides fixed P and Q to the system. Hence only the Synchronous generator is responsible of maintaining the system frequency and the voltage at nominal values. Fig. 7.8 presents angular frequency, system voltage and active power contribution from each generator for this case. It is visible that only the synchronous generator supplies the power required by PPL. Transients can be observed in system frequency and voltage profiles. Voltage fluctuation of the system is about 2.7% at 33.5-s which is above the maximum permissible voltage fluctuation, 2% (when the fluctuations per minute is 1) [101, 102]. This will cause visible and uncomfortable voltage flicker in the system. Frequency fluctuation of the system is about 4% and which will effect on the transient stability of the system. However the limit based control implemented for the charging

process of the capacitor, and the control system of the synchronous generator ensures the dynamic stability of the system.

7.4.2 Active Control of the Inverter

In this case inverter is actively participating in controlling the system frequency and the voltage. The control strategies presented in section II, centralized and decentralized controls are implemented for the inverter control.

7.4.2.1 Centralized Control

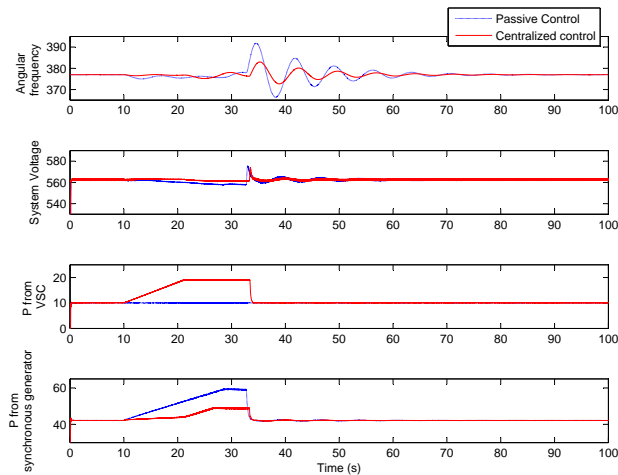


Figure 7.9. Active control of the inverter with centralized control compared to passive control, (a) angular frequency of the system (b) system voltage (c) active power from the inverter (d) active power from the synchronous generator.

The inverter active power and reactive power references are set by the central controller. These values are set according to the power requirement of the PPL. The voltage at the capacitor will be measured. The power requirement is computed based on the measurement and the reference current order and will be sent to the inverter. This can be achieved through fast communication between the Microgrid Central Controller (MCC) and Local Controllers (LCs) of the PPL and the inverter. Fig. 7.9 shows a comparison of the angular frequency, system voltage and active power contribution from each generator with passive control and centralized active control. Since

the inverter is participating in providing power to the PPL, system transients are much lower in active control. Frequency fluctuation of the system is about 1% which is acceptable and the voltage fluctuation of the system is about 2.0% which is at maximum permissible voltage fluctuation level [101, 102] resulting visible voltage flicker in the system. The dynamic stability of the system is improved compared to the passive control. Note that the maximum power from the inverter is limited to 20 kW. The rest of the power demand will come from the synchronous generator.

7.4.2.2 Decentralized Control

In this control architecture LC of the inverter is responsible for keeping the voltage and the frequency of the system at nominal values. This is achieved through implementing frequency and voltage droop control within the inverter control. Control block diagram of the inverter is presented in Fig.7.1. Reference values for the active and reactive power is calculated according to the droop characteristics of the inverter.

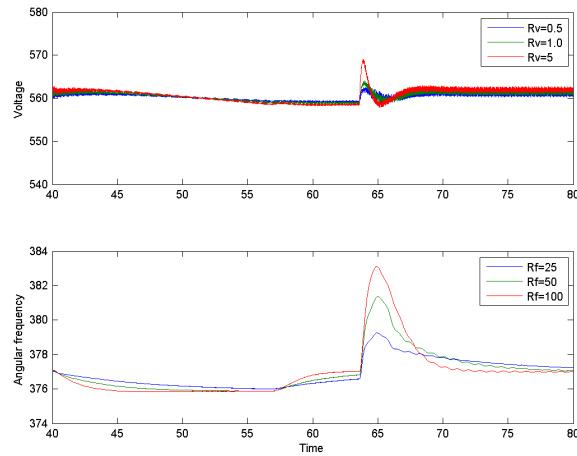


Figure 7.10. Angular frequency and the voltage of the system for different R_f and R_v .

Fig. 7.10 shows the system frequency and the voltage behavior for a PPL starts at 39 seconds and stops at 63 seconds at different R_f and R_v values. It can be seen that the lower the R_f and R_v are, the faster the response is from the inverter. However, if R_f or R_v is too small, the control

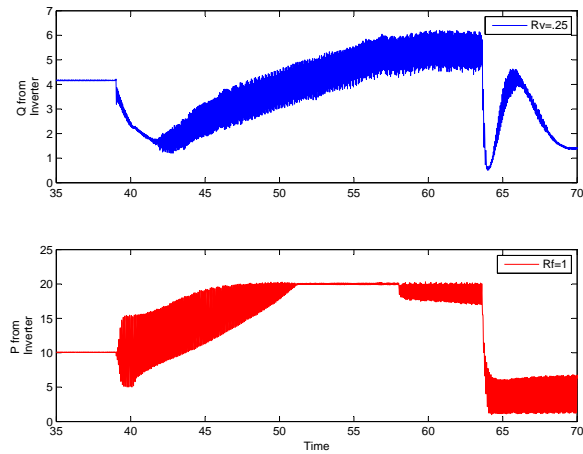


Figure 7.11. Power output from the inverter for lower R_f and R_v .

loop of the inverter goes unstable and the output power oscillates as shown in Fig. 7.11. Hence R_f is chosen to be 25 while R_v is set to .5.

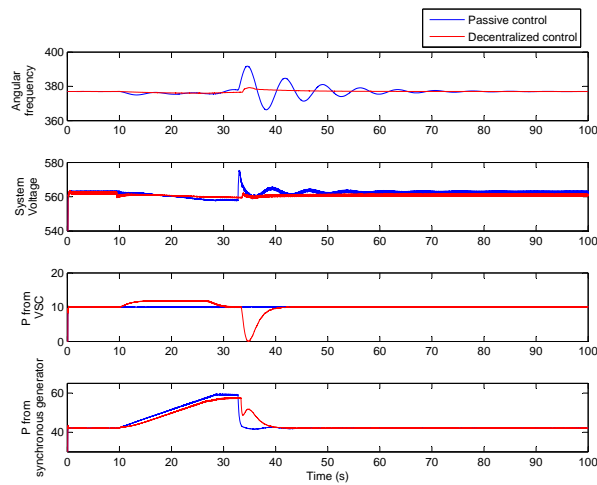


Figure 7.12. Active control of the inverter with decentralized control compared to passive control, (a) angular frequency of the system (b) system voltage (c) active power from the inverter (d) active power from the synchronous generator.

Fig. 7.12 presents a comparison of the angular frequency, system voltage and active power contribution from each generator with passive control and decentralized active control. Here frequency transients and the voltage transients of the system are dying out much quicker compared to other

control mechanisms. Frequency fluctuation of the system is about .7% and the voltage fluctuation of the system is about .4% which is well below the permissible voltage fluctuation level [101, 102]. The dynamic stability of the system is much better compared to the other two control methods.

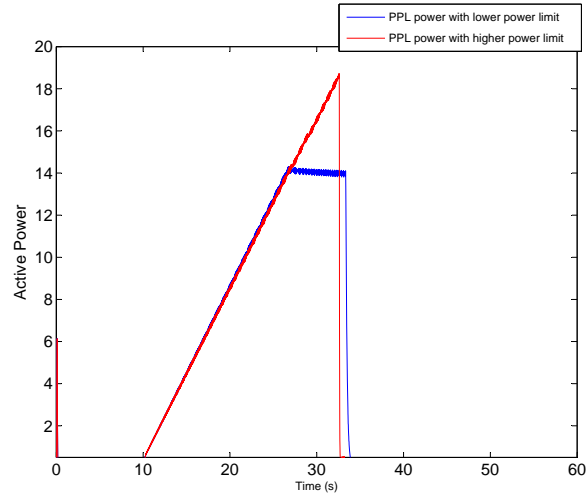


Figure 7.13. PPL power with limit based control.

Fig. 7.13 shows the charging power profile of the PPL capacitor with an increased power limit compared to the previous charging profile with low power limit. About 3 % improvement can be observed in the charging time with an increased power limit. The angular frequency profile and the voltage profile of the system for the above case is presented in Fig. 7.14.

To show a more realistic picture of the PPL, a repetitive pulsed load is simulated with the passive control and the decentralized control. The pulsed load is simulated in every 40-s as shown in Fig. 7.15 .The angular frequency and the voltage profile comparison is made in Fig. 7.16.

7.5 Conclusion

This chapter presents a study of microgrid operation with pulsed power loads and how to utilize inverter based DERs to improve the stability of the system. Same power limit was considered for limit based control in all three cases in order to provide a better comparison based on stability. However with the active control the power limit can be increased further without affecting the system stability. This will lead to a shorter charging time which will be a major advantage for

PPLs. It is observed that the fully autonomous operation of a microgrid can be achieved by implementing decentralized control in the inverter and decentralized control with droop control is better than the passive control and the centralized control to handle the transients caused by PPLs.

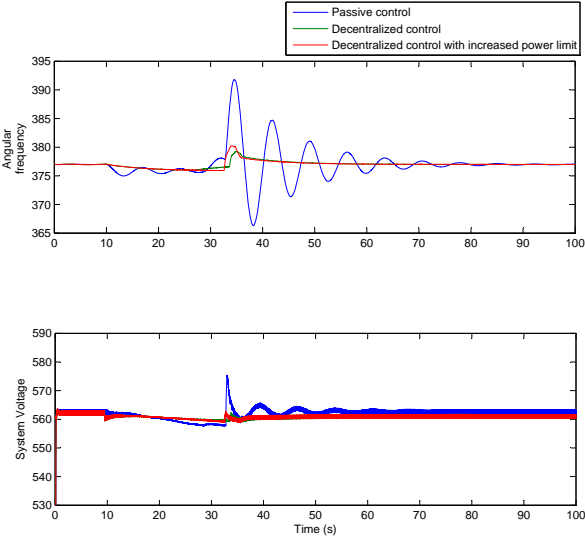


Figure 7.14. Effect of increased power limit in active control of the inverter with decentralized control, (a) angular frequency of the system (b) system voltage.

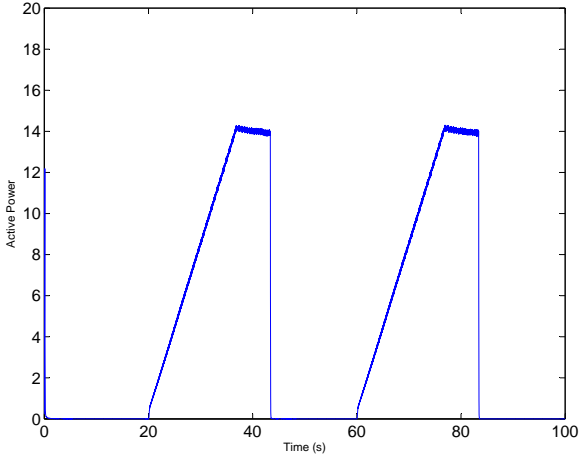


Figure 7.15. Repetitive PPL.

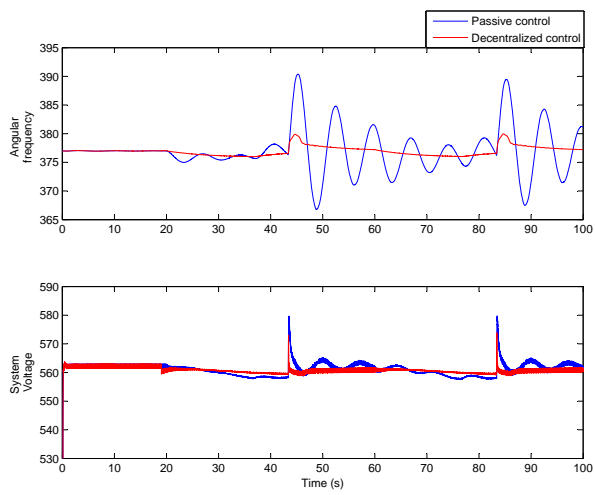


Figure 7.16. Active control of the inverter with decentralized control compared to passive control for repetitive PPL, (a) angular frequency of the system (b) system voltage.

CHAPTER 8

RT-LAB MODELING AND HIL SETUP FOR MICROGRIDS

8.1 Introduction

This chapter presents modeling and simulations of microgrids in a real time simulator. The first section ¹ demonstrate a HIL test bed to test the real battery system connected to real time simulation model of a microgrid implemented in RT-LAB. Modeling of a single phase PV system for real time simulation is presented in next section ².

8.2 Real-Time Simulation and Hardware-In-The-Loop Tests of a Battery System

Simulating the physical system will be the ideal way to test the behavior of the control and operation of the system. However, building a tested with the full physical system is expensive. Hence HIL simulations are one of the cutting edge technology emerging in todays world. Here, the system is built on a hybrid platform, consist of physical systems and system software. Some work dedicated to HIL studies can be found in the literature [103, 104, 105, 106]. Lithium ion batteries have a significant share in the electronic market and are penetrating into the electric vehicle market and grid storage market today. Inherent benefits of Li-ion batteries such as 80% Depth Of Discharge (DOD), higher energy density (up to 115Wh/kg) and better efficiency (90-96%) [107] make this transition faster. As with any other type of batteries, Li-ion batteries also degrade over time due to various factors. Hence it is vital to study the degradation of these batteries in order to identify the conditions that effect on the degradation. HIL simulation can be adopted to study this battery degradation and its characteristics. A microgrid system composed of a wind farm, a PV system,

¹This section is based on the work published in Power & Energy Society General Meeting, 2015 IEEE. Permission is included in Appendix A.

²This section is based on the work published in PES General Meeting Conference & Exposition, 2014 IEEE , vol., no., pp.1-5, 27-31 July 2014. Permission is included in Appendix A.

a battery energy storage system, a plug-in electric vehicle (PEV) and loads have been built in RT-LAB simulators to achieve the above task. Here the battery system is replaced with the real battery pack and several case studies were conducted to demonstrate the capabilities of the test bed.

8.2.1 System Topology

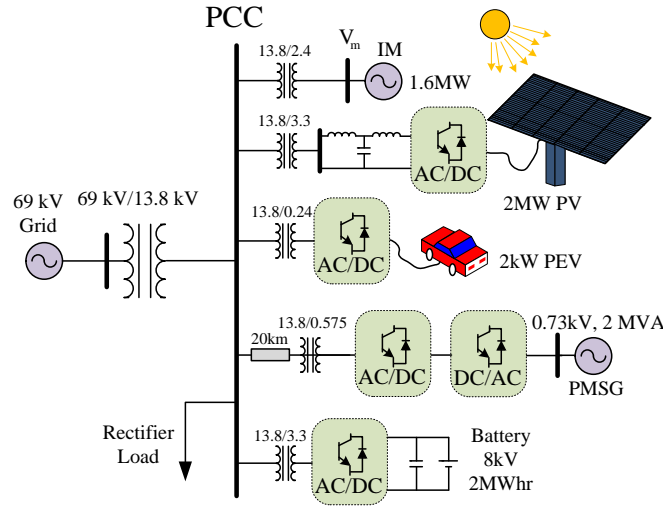


Figure 8.1. Microgrid topology.

The microgrid which is implemented in RT-LAB is presented in in Fig. 8.1. Here the microgrid is consist of a battery energy storage system, a PV system, a wind farm, a plug-in electric vehicle (PEV) and loads. The battery system which consist of two battery packs connected in series has a capacity of 2 WMh and capable of providing 2 MW maximum power. Each Battery pack rated voltage is 4.1 kV. The rated capacity of the PV array is 2 MW with 2 kV dc voltage. PV system is working in Maximum Power Point Tracking (MPPT) control mode. The 2 MW wind farm consists of the wind turbine model, Permanent magnet Synchronous Generator (PMSG) and back to back converter. Table 8.1 lists the parameters of each component in the microgrid.

Table 8.1. Simulation system parameters

Quantity	Value
ac grid voltage	69kV (L-L RMS)
Induction machine ratings	2.4kV, 1.6MW
PEV battery ratings	0.375kV, 53kWhr
Battery ratings	8.2kV, 2MWhr
PV ratings	2kV, 2MVA
PMSG ratings	0.73kV, 2MVA
Load ratings	100ohm+500mH

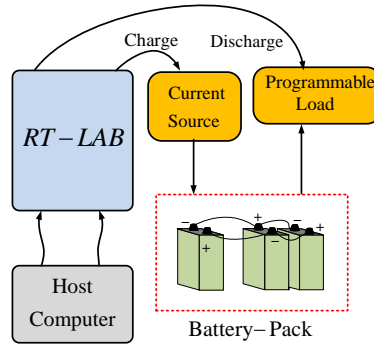


Figure 8.2. HIL testbed setup.

8.2.1.1 HIL Testbed Setup

A real battery cell with the rating of 3.2 V, 40 Ahr is used to implement the HIL system as illustrated in Fig. 8.2. Since the battery system in the microgrid ratings are higher, the scaling factors are used to convert voltage and current measurements and commands back and forth. Here scaling factors are chosen as 2560 and 6 for the voltage and the current. An external controlled voltage source is utilized to represent the battery system in the RT- LAB Simulink model. Here the external control signal is received via scaled up analog input of the Rt- LAB device. This Analog signal is nothing but the voltage measurement of the real battery pack. The DC current flowing from the Simulink model battery system is measured and scaled down signal is sent via the analog output to the programmable current source(Magna) or load (BK 8500). Fig. 8.3 demonstrate the configuration for the HIL simulation of the battery system .

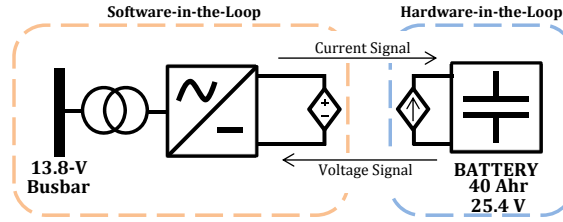


Figure 8.3. Hardware-in-the-loop simulation of the battery system.

8.2.1.2 Battery Inverter Control

The implemented battery inverter has the capability of operating in 3 modes: power control, dc-link voltage control and voltage/frequency control. One of the first two modes can be employed when the microgrid is connected to grid while the last mode can be used for islanded operation. The control loop of the VSC controller shown in Fig. 8.4 consist of two control loops: inner current control loop and outer control loop. While the inner control loop controls the current outer control loop can be either active power control or dc voltage control or ac voltage and frequency control [108, 109] depends on the mode of operation.

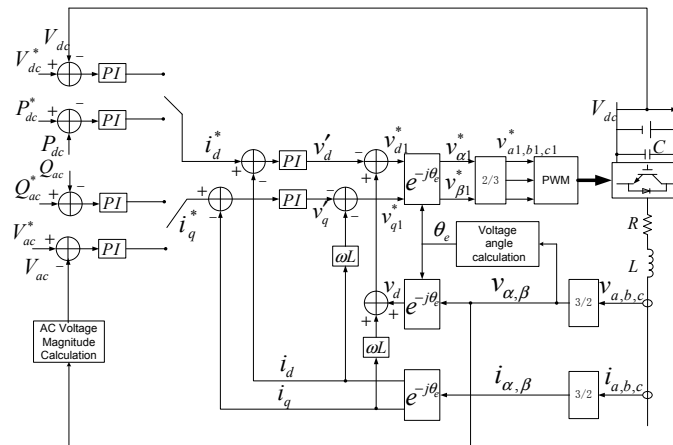


Figure 8.4. Control of the battery inverter.

An upper level control strategy which is presented in Fig. 8.5 is implemented to monitor the battery SOC and protect the batteries from over charging or discharging.

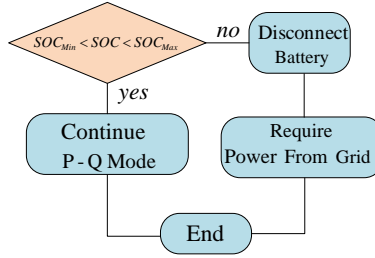


Figure 8.5. Upper level control considering SOC.

8.2.1.3 Coordinated Control of Battery and PV

Here, the coordinated control strategy make sure that the total power produced by PV and the battery keep at a constant value. This is achieved via controlling the power of the battery according to the PV power output. This will compensate the intermittent nature of the PV output and make sure to have a smooth total power injection. The coordinated control strategy considering battery SOC limits is presented in Fig. 8.6.

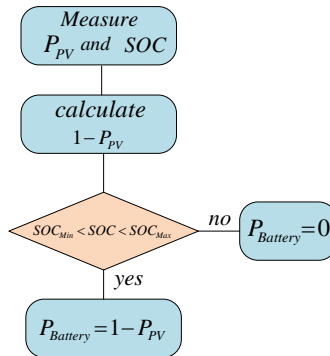


Figure 8.6. Coordinated control of a battery and a PV.

8.2.2 Simulation Results for Battery Performance in Microgrid

8.2.2.1 Base Case

Battery power order and the actual power of the battery is shown in Fig. 8.7. Here battery is operating in $P - Q$ control mode and the results validate the accurate operation of the implemented control mode. Negative sign indicates charging of the batteries and positive sign indicates discharging the batteries.

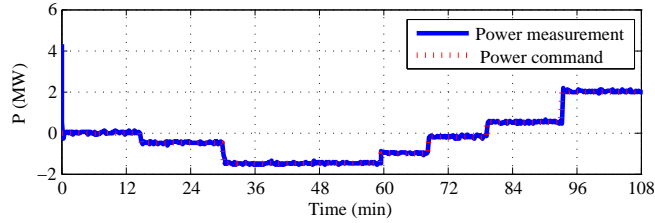


Figure 8.7. Reference active power change for a battery connected to the microgrid.

8.2.2.2 Performance of PV and Battery

Fig. 8.8 shows the results of the implemented, coordinated control strategy. Here the total power from PV and the battery is set to 1 MW. The irradiance level is changed during the simulation and battery power output changes accordingly. Due to a sudden irradiance change after 1 hour, the PV power falls down from 0.35 MW to -0.5 MW, and the battery power will increase from 0.65 MW to 1.5 immediately to compensate this PV power change.

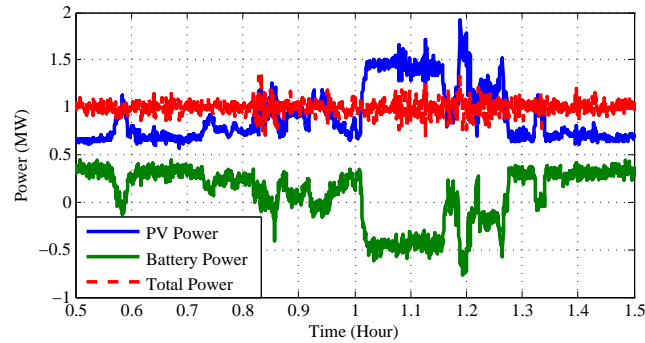


Figure 8.8. Coordinated control of battery and PV.

8.2.2.3 Simulation Results Considering SOC Limits

If the battery hits the SOC limits while operating in the coordinated control the upper control strategy will disconnect the battery resulting the loss of coordination control.

Fig. 8.9 shows that at 0.45 second, the SOC of the battery hit the maximum SOC limit, $SOC_{Max} = 0.908$ and the battery is disconnected from the system. The battery will remain disconnected until the battery control gets a command to discharge. It can be seen that at 0.57

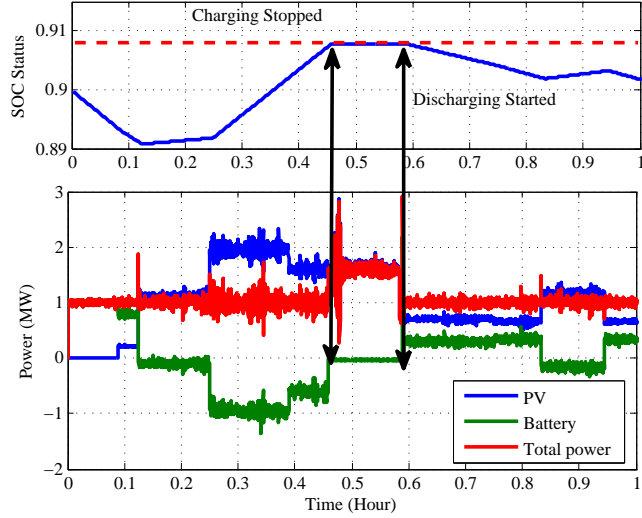


Figure 8.9. Coordinated control of battery and PV considering SOC limits.

second, the PV power is less than 1 MW and the battery starts discharging resulting SOC to be decreased.

8.2.3 HIL Experiments Results

The HIL testbed is built using a Programmable current source, programmable load, a battery cell and OP 5600 RT- LAB device. Constant current charging and discharging mechanism has been implemented to initiate the battery degradation study. Based on the battery SOC Vs voltage characteristics provided by the manufacturer upper voltage limit is chosen to be 3.58 V and the lower bound is chosen to be 3.1 V. Fig. 8.10 presents 60 hours of data collected through RT-LAB with this setup. Fig. 8.11 illustrates the charging and discharging curves in detail.

The round-trip efficiency of the battery is calculated by using the graph presented in Fig. 8.12. It can be seen that the stored energy during charging process is 138.26 VAh while discharged energy is 130.36 VAh. Hence the round-trip efficiency of the battery is 94.3 % at the current operating point.

The internal resistance of the battery can be obtained by referring to the Fig. 8.13. Since the discharging of the battery can be represented by the equivalent circuit as shown in Fig. 8.14 the

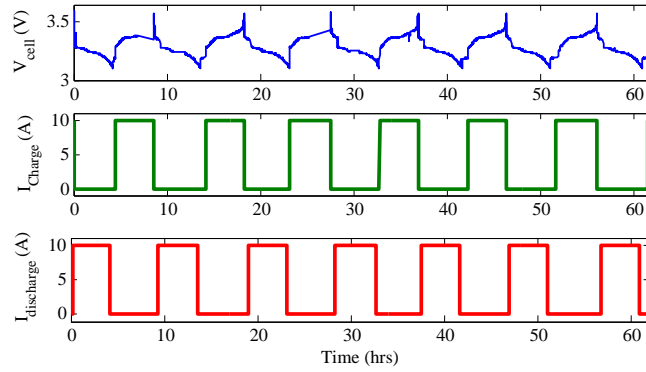


Figure 8.10. Measured voltage and current profiles of a single battery cell.

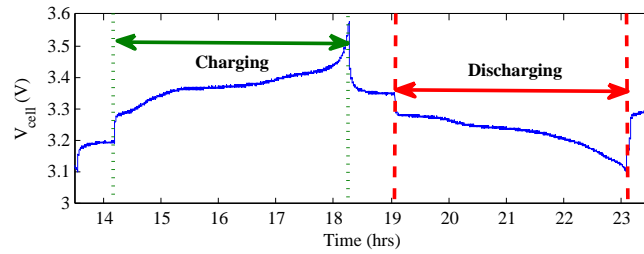


Figure 8.11. Voltage and current profiles of a battery cell.

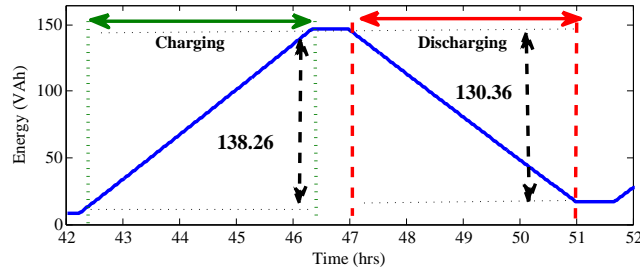


Figure 8.12. Energy profile of the battery cell.

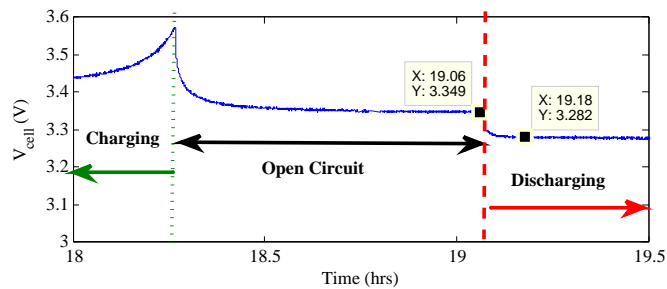


Figure 8.13. Battery cell voltage profile for calculation of internal resistance.

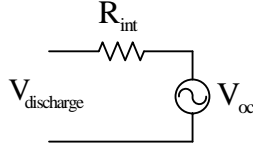


Figure 8.14. Resistance calculation circuit.

internal resistance can be calculated using,

$$R_{int} = \frac{V_{oc} - V_{discharge}}{I_{discharge}} \quad (8.1)$$

The discharge current, $I_{discharge}$ is set as 10 A. The internal resistance can be obtained as 6.8 mΩ by referring to Fig. 8.13 open circuit voltage curve .

8.3 Real-Time Modeling of Single-Phase PV in RT-LAB

Real time simulators have been widely used to simulate modern power systems with power electronic components in real time. Some work can be found in the literature related to modeling of power system components in the RT - LAB [76, 110, 111]. Single phase PV systems play a major role in the domestic power generation and can be a major part of future microgrids. Hence it is essential to have an accurate single phase PV model in RT- LAB for further simulations and studies. This section is dedicated to model a detailed single-stage PV in RT-LAB. Here, Phase Locked Loop (PLL), Proportional Resonance (PR) controller, Maximum Power Point Tracking (MPPT) control, and converter is modeled in RT- LAB.

Fig. 8.15 presents the Real-time digital simulation setup with oscilloscopes connected to an RT - LAB device to monitor real time simulation outputs.

Traditional two stage converters consist of DC to DC converter which will boost the DC voltage and DC to AC converter which will connect the PV system to AC grid.

8.3.1 System Configuration

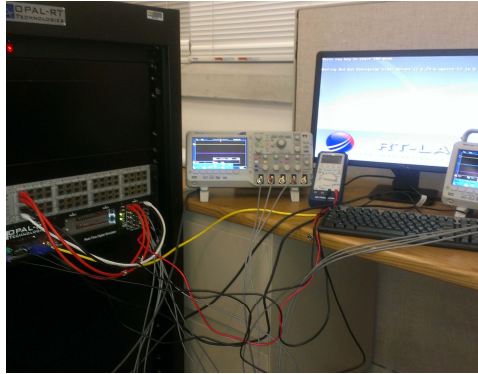


Figure 8.15. Real-time digital simulation setup using RT-Lab.

However single stage converter has some advantages as: higher efficiency, lower price, and easier implementation compared to two stage converters [69]. Hence single stage single phase PV system which is illustrated in Fig. 8.16 is implemented.

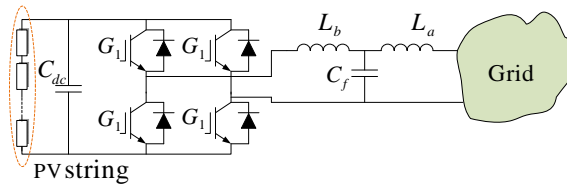


Figure 8.16. System under investigation for simulation in RT-LAB, $L_a = 10e - 3$, $L_b = 20e - 3$, $C_f = 1e - 6$, $C_{dc} = 10e - 3$.

PV array which is composed of 96 *SunPowerSPR – 305 – WHT* PV cells, which is modeled in the RT-LAB. The PV array power rating is 2MW and voltage rating is 350V and consist of 1 parallel string, 8 series modules, open circuit voltage of 64.2 per cell, and short circuit current of 5.96 per cell.

8.3.2 PV Control

8.3.2.1 MPPT Control

Maximum Power Point Tracking (MPPT) strategy is utilized to absorb the maximum power from PV cells at a given time. The incremental conductance technique where the output current and

the voltage of the PV panel is used to calculate the conductance and incremental conductance is used as the MPPT technique. Here the conductance ($\frac{I_{PV}}{V_{PV}}$) is compared with incremental conductance ($\frac{dI_{PV}}{dV_{PV}}$) and PV voltage will be changed accordingly to reach to the maximum power point [69]:

$$\frac{dP}{dV} = \frac{d(V.I)}{dV} = I + V \frac{dI}{dV} = 0 \quad (8.2)$$

$$\frac{dI}{dV} = -\frac{I}{V} \quad (8.3)$$

Here, Maximum power is guaranteed when the conductance is equal to incremental conductance. An integral regulator is utilized to minimize the error which is $(\frac{dI}{dV} + \frac{I}{V})$. Fig 8.17 illustrates the MPPT control digram implemented in the RT - LAB.

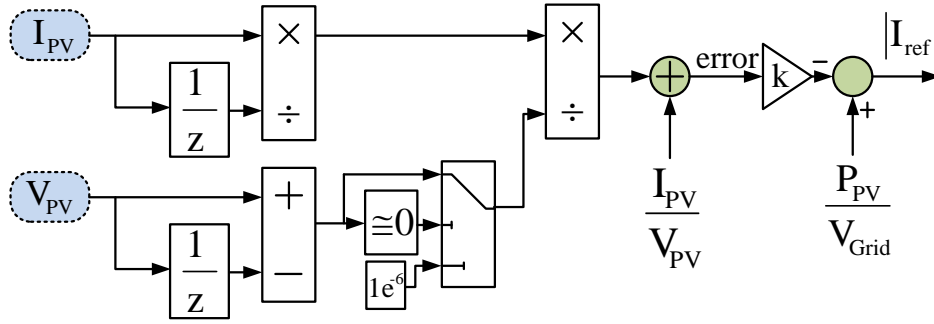


Figure 8.17. The MPPT structure for single phase PV in RT-LAB.

The I-V characteristic of the PV and error curves are presented in Fig 8.18. As it can be seen that $\frac{dI}{dV}$ is always negative. Here, the error: $\frac{dI}{dV} + \frac{I}{V}$ will be 0 when $\theta_1 = \theta_2$ and in the left side region from that point error is greater than zero and right hand side error is less than zero. When the error is greater than zero current magnitude will be decreased and current magnitude will be increased when error is less than zero to come back to zero error.

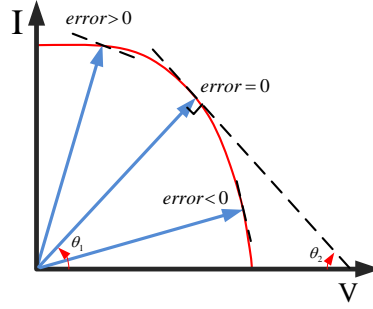


Figure 8.18. Error signal description based on I-V characteristic of PV.

8.3.2.2 Proportional Controller (PR)

The main equation of PR controller can be mentioned as [112]:

$$F_{PR} = K_p + K_r \frac{s}{s^2 + (h\omega)^2} \quad (8.4)$$

The PR controller for single phase PV has been designed to compensate the high order frequencies of: 3rd, 5th, 7th, and 9th. The block diagram of the proposed controller has been illustrated in Fig. 8.19.

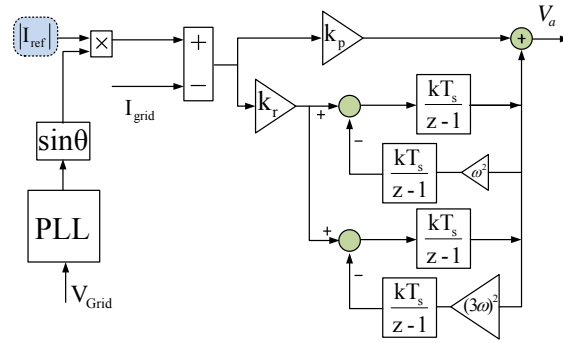


Figure 8.19. The PR controller structure for single phase PV.

The MPPT block provides to the reference current signal magnitude and it will be synchronized with the grid voltage using a PLL. This synchronized current sin waveform will be compared with actual current and the error signal will be fed to the PR controller. The output of the PR controller is the voltage reference of the converter and will be sent to the pulse generation unit to switch the

IGBTs. Since RT-LAB is using fixed step size for simulations the whole model has to build in the discrete time domain. Discrete time domain model of the PR controller, considering the third harmonic is illustrated in Fig. 8.19.

8.3.3 Case Studies

RT-LAB models in general consist of three main blocks: Master subsystem, Slave subsystem and Console subsystem. Master subsystem in general includes the controls and hardware communication models. It works as the brain of the model. The system components such as transmission lines, generators machines, transformers and converters are modeled inside the slave block. Depend on the system size one or more slave blocks can be included in one RT-LAB model. The console is working as the Real time user interface and the monitor. These subsystems will have communication between each other.

8.3.3.1 Normal Case

Normal operation of the PV system is simulated first to observe the PV model operation. A step change to the irradiance is applied at 10 sec to see PV model response for a sudden irradiance change. A ramp change is applied at 20 sec to see the PV system response to slow changes of irradiance. These Irradiance change patterns are presented in Fig. 8.20.

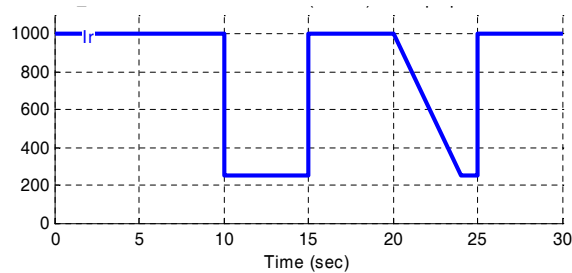


Figure 8.20. Irradiance change for PV in order to verify the stable operation.

The real time operation result of the PV system is illustrated in Fig. 8.21. These signals are recorded from an oscilloscope connected to the RT-LAB device. Here, the first signal is the reference current fed to the PR controller and the second signal is actual PV current. Third signal

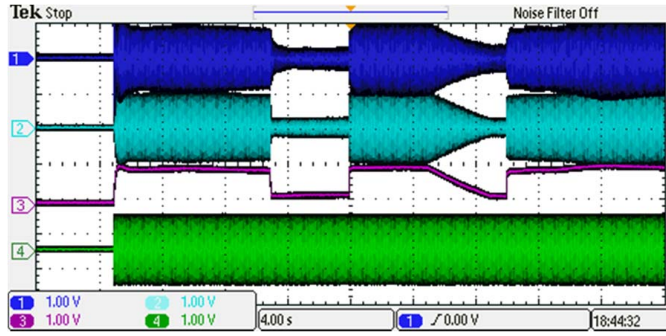


Figure 8.21. PV responses due to the irradiance change composed of ramp and step changes.

is the PV power and the last signal is the grid voltage which is supposed to be content thorough the operation. Fig. 8.22 illustrated the PV current order and actual PV current. It can be observed

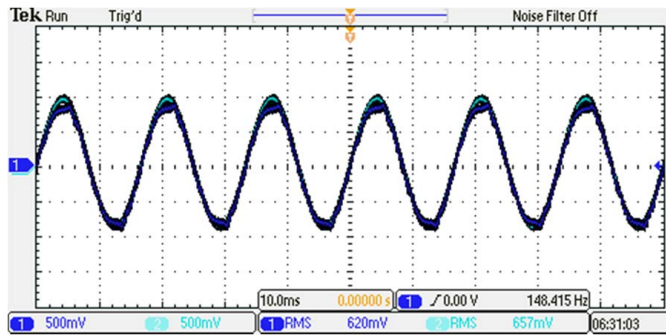


Figure 8.22. Comparison of reference current and measured current of the PV.

that the actual current follows the PV current order leading to stable operation.

Fig. 8.23 presents the PV response to the irradiance ramp change. It can be seen PV can respond well to the slow irradiance changes. The PV response to the irradiance step change is shown in Fig. 8.24 and the result shows that the built PV model can respond well to sudden irradiance changes.

8.3.3.2 Experimental Case with External Input

Here the irradiance measurement is fed to the RT-LAB via its hardware input ports to make the simulation more realistic. The irradiance level signal is created using Chroma Programmable AC source model 61501 which is shown in Fig. 8.25.

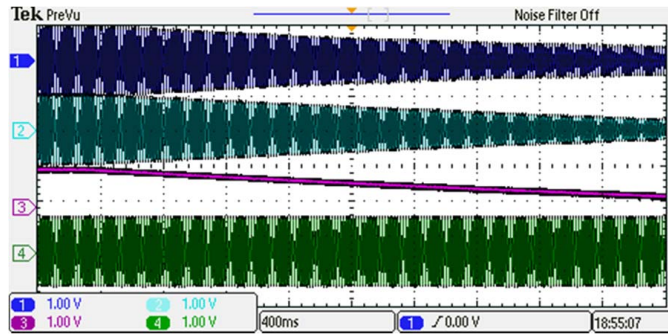


Figure 8.23. PV response to the ramp change in irradiance.

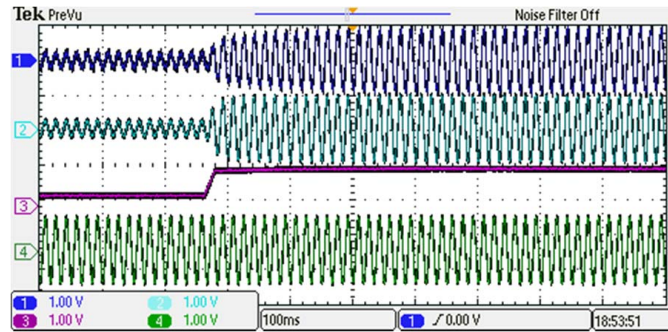


Figure 8.24. PV response to the step change in irradiance.



Figure 8.25. Chroma setup.

A random irradiance signal is generated from the Chroma model and fed into the RT-LAB device. Fig. 8.28 and Fig. 8.27 present the generated irradiance pattern and PV model response to that. It can be observed that the PV system is able to follow the irradiance pattern accurately.

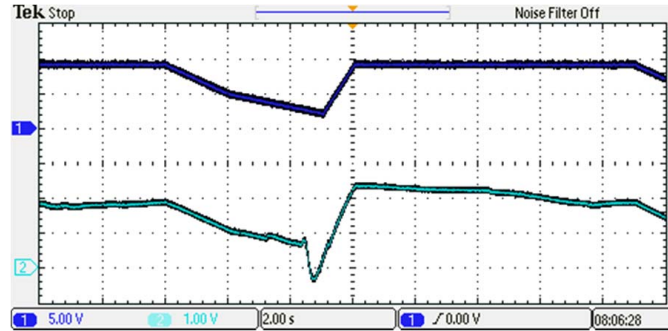


Figure 8.26. Measured irradiance by Chroma and PV output power.

Fig. 8.27 presents the reference current, measured actual current, PV power and grid voltage waveforms recorded in an oscilloscope.

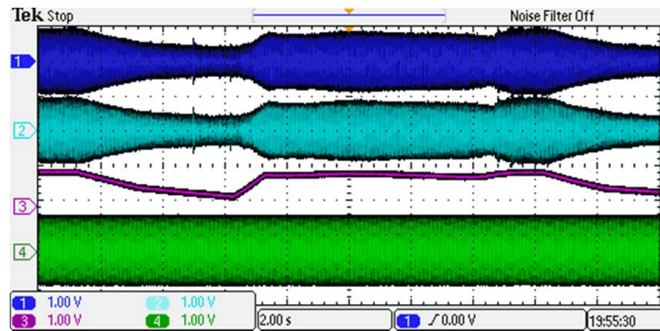


Figure 8.27. Results of the simulation with changing irradiance.

Fig. 8.28 shows the performance metric of the model. This performance matrix is obtained by utilizing the Opmonitor Block in the RT-LAB. Here idle time is the idle time during the execution of previous time step. It can be seen that the RT-LAB model is capable of doing required tasks within the given step size. Here step size is 25 microseconds, but the computational time is well below that. In fact the computational time is about 4 % ($\frac{25-24}{25} * 100\%$) of total time step resulting minimum usage of the CPU. It can be seen that the number of overruns is zero throughout the simulation process which clarify the perfect running conditions.

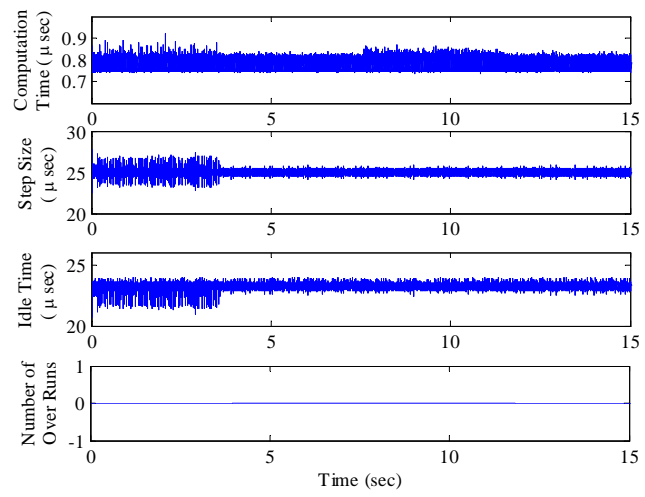


Figure 8.28. Simulation results from opmonitor block.

CHAPTER 9

CONCLUSIONS

This dissertation can be concluded as follows.

Initialization and steady state calculations for power systems with renewable energy penetration are presented in chapter 3. Steady state calculations for a system with wind power integration and initialization of an unbalanced system with the single phase PV system is conducted as case studies. The dynamic phasor approach is utilized in the later case.

Chapter 4 and 5 present the capability of dynamic phasor and impedance modeling techniques. First, the SSR problem in the TCSC compensated network is analyzed in detail to identify the stability limits of the system. Chapter 5 develops a detailed model for unbalanced microgrid. Single phase PV, induction machine, power factor correction and loads are modeled and analyzed using small signal analysis.

Upper level control of a microgrid is presented in Chapter 6. The micro grid consists of a PV system, wind farm, a battery storage and some loads. Prediction algorithms are proposed to predict PV power, wind power and load power. Multi-horizon Optimization algorithm is developed and implemented in real-time simulator to optimized power import of the microgrid by controlling the battery power output.

Chapter 7 investigates the intermittent load applications in microgrid. A pulsed power load is implemented as intermittent load and VSC based inverter is proposed to mitigate the system dynamics due to the pulsed load behavior. A test bed for microgrid simulations using real time simulator and hardware in loop is developed in chapter 8.

REFERENCES

- [1] X. Lu, M. B. McElroy, and J. Kiviluoma, "Global potential for wind-generated electricity," *Proceedings of the National Academy of Sciences*, vol. 106, no. 27, pp. 10 933–10 938, 2009.
- [2] M. Chandorkar, D. Divan, and R. Adapa, "Control of parallel connected inverters in stand-alone ac supply systems," *Industry Applications, IEEE Transactions on*, vol. 29, no. 1, pp. 136 –143, jan/feb 1993.
- [3] R. Majumder, B. Chaudhuri, A. Ghosh, R. Majumder, G. Ledwich, and F. Zare, "Improvement of stability and load sharing in an autonomous microgrid using supplementary droop control loop," *Power Systems, IEEE Transactions on*, vol. 25, no. 2, pp. 796 –808, may 2010.
- [4] F. Katiraei and M. Iravani, "Power management strategies for a microgrid with multiple distributed generation units," *Power Systems, IEEE Transactions on*, vol. 21, no. 4, pp. 1821 –1831, nov. 2006.
- [5] O. Gomis-Bellmunt, A. Junyent-Ferre, A. Sumper, and J. Bergas-Jan, "Ride-through control of a doubly fed induction generator under unbalanced voltage sags," *Energy Conversion, IEEE Transactions on*, vol. 23, no. 4, pp. 1036 –1045, dec. 2008.
- [6] S. Seman, J. Niiranen, and A. Arkkio, "Ride-through analysis of doubly fed induction wind-power generator under unsymmetrical network disturbance," *Power Systems, IEEE Transactions on*, vol. 21, no. 4, pp. 1782 –1789, nov. 2006.
- [7] J. Hu, Y. He, L. Xu, and B. Williams, "Improved control of dfig systems during network unbalance using pi-r current regulators," *Industrial Electronics, IEEE Transactions on*, vol. 56, no. 2, pp. 439 –451, feb. 2009.
- [8] L. Xu and Y. Wang, "Dynamic modeling and control of dfig-based wind turbines under unbalanced network conditions," *Power Systems, IEEE Transactions on*, vol. 22, no. 1, pp. 314 –323, feb. 2007.
- [9] Y. Zhou, P. Bauer, J. Ferreira, and J. Pierik, "Operation of grid-connected dfig under unbalanced grid voltage condition," *Energy Conversion, IEEE Transactions on*, vol. 24, no. 1, pp. 240 –246, march 2009.
- [10] D. Santos-Martin, J. Rodriguez-Amenedo, and S. Arnalte, "Direct power control applied to doubly fed induction generator under unbalanced grid voltage conditions," *Power Electronics, IEEE Transactions on*, vol. 23, no. 5, pp. 2328 –2336, sept. 2008.

- [11] J. Lopez, E. Gubia, P. Sanchis, X. Roboam, and L. Marroyo, “Wind turbines based on doubly fed induction generator under asymmetrical voltage dips,” *Energy Conversion, IEEE Transactions on*, vol. 23, no. 1, pp. 321–330, march 2008.
- [12] T. Brekken and N. Mohan, “A novel doubly-fed induction wind generator control scheme for reactive power control and torque pulsation compensation under unbalanced grid voltage conditions,” in *Power Electronics Specialist Conference, 2003. PESC '03. 2003 IEEE 34th Annual*, vol. 2, june 2003, pp. 760–764 vol.2.
- [13] R. Pena, R. Cardenas, E. Escobar, J. Clare, and P. Wheeler, “Control system for unbalanced operation of stand-alone doubly fed induction generators,” *Energy Conversion, IEEE Transactions on*, vol. 22, no. 2, pp. 544–545, june 2007.
- [14] A. Stankovic, S. Sanders, and T. Aydin, “Dynamic phasors in modeling and analysis of unbalanced polyphase ac machines,” *Energy Conversion, IEEE Transactions on*, vol. 17, no. 1, pp. 107–113, mar 2002.
- [15] T. H. Demiray, “Simulation of power systems dynamics using dynamic phasor models,” Ph.D. dissertation, Swiss Federal Institute of Technology, Zurich, 2008.
- [16] T. Demiray, F. Milano, and G. Andersson, “Dynamic phasor modeling of the doubly-fed induction generator under unbalanced conditions,” in *Power Tech, 2007 IEEE Lausanne*, july 2007, pp. 1049–1054.
- [17] A. Stankovic, B. Lesieutre, and T. Aydin, “Modeling and analysis of single-phase induction machines with dynamic phasors,” *Power Systems, IEEE Transactions on*, vol. 14, no. 1, pp. 9–14, feb 1999.
- [18] Z. Miao, “Impedance-model-based ssr analysis for type 3 wind generator and series-compensated network,” 2012.
- [19] J. H. Enslin and P. J. Heskes, “Harmonic interaction between a large number of distributed power inverters and the distribution network,” *Power Electronics, IEEE Transactions on*, vol. 19, no. 6, pp. 1586–1593, 2004.
- [20] T.-L. Lee and P.-T. Cheng, “Design of a new cooperative harmonic filtering strategy for distributed generation interface converters in an islanding network,” *Power Electronics, IEEE Transactions on*, vol. 22, no. 5, pp. 1919–1927, 2007.
- [21] B. Fox, D. Flynn, L. Bryans, N. Jenkins, D. Milborrow, M. OMalley, R. Watson, and O. Anaya-Lara, “Wind power integration,” *The Institution of Engineering and Technology*, 2007.
- [22] Y.-K. Wu and J.-S. Hong, “A literature review of wind forecasting technology in the world,” in *Power Tech, 2007 IEEE Lausanne*. IEEE, 2007, pp. 504–509.
- [23] A. Khan and M. Shahidehpour, “One day ahead wind speed forecasting using wavelets,” in *Power Systems Conference and Exposition, 2009. PSCE'09. IEEE/PES*. IEEE, 2009, pp. 1–5.

- [24] A. Junyent-Ferré, O. Gomis-Bellmunt, A. Sumper, M. Sala, and M. Mata, “Modeling and control of the doubly fed induction generator wind turbine,” *Simulation Modelling Practice and Theory*, vol. 18, no. 9, pp. 1365–1381, 2010.
- [25] J. F. M. Padrón and A. E. F. Lorenzo, “Calculating steady-state operating conditions for doubly-fed induction generator wind turbines,” *Power Systems, IEEE Transactions on*, vol. 25, no. 2, pp. 922–928, 2010.
- [26] L. Yong and S. Tao, “Economic dispatch of power system incorporating wind power plant,” in *Power Engineering Conference, 2007. IPEC 2007. International.* IEEE, 2007, pp. 159–162.
- [27] Z. Bo and C. Yi-jia, “Multiple objective particle swarm optimization technique for economic load dispatch,” *Journal of Zhejiang University SCIENCE A*, vol. 6, no. 5, pp. 420–427, 2005.
- [28] L. Wang and C. Singh, “Tradeoff between risk and cost in economic dispatch including wind power penetration using particle swarm optimization,” in *Power System Technology, 2006. PowerCon 2006. International Conference on.* IEEE, 2006, pp. 1–7.
- [29] J. Sloopweg, H. Polinder, and W. Kling, “Initialization of wind turbine models in power system dynamics simulations,” in *Power Tech Proceedings, 2001 IEEE Porto*, vol. 4. IEEE, 2001, pp. 6–pp.
- [30] A. M. Stankovic, S. R. Sanders, and T. Aydin, “Dynamic phasors in modeling and analysis of unbalanced polyphase ac machines,” *Energy Conversion, IEEE Transactions on*, vol. 17, no. 1, pp. 107–113, 2002.
- [31] P. Mattavelli, A. M. Stankovic, and G. C. Verghese, “Ssr analysis with dynamic phasor model of thyristor-controlled series capacitor,” *Power Systems, IEEE Transactions on*, vol. 14, no. 1, pp. 200–208, 1999.
- [32] D. Das, H. Nagi, and D. Kothari, “Novel method for solving radial distribution networks,” *IEE Proceedings-Generation, Transmission and Distribution*, vol. 141, no. 4, pp. 291–298, 1994.
- [33] G. Irwin, A. Jindal, and A. Isaacs, “Sub-synchronous control interactions between type 3 wind turbines and series compensated ac transmission systems,” in *IEEE Power & Energy General Meeting*, Jul. 2011.
- [34] L. Fan, R. Kavasseri, Z. Miao, and C. Zhu, “Modeling of DFIG-based wind farms for SSR analysis,” *IEEE Trans. Power Del.*, vol. 25, no. 4, pp. 2073–2082, Oct. 2010.
- [35] L. Fan, C. Zhu, Z. Miao, and M. Hu, “Modal analysis of a DFIG-based wind farm interfaced with a series compensated network,” *IEEE Trans. Energy Convers.*, vol. 26, no. 4, pp. 1010–1020, Dec. 2011.
- [36] L. Fan and Z. Miao, “Mitigating SSR using DFIG-based wind generation,” *IEEE Trans. Sustainable Energy*, vol. 3, no. 3, pp. 349–358, Jul. 2012.
- [37] ———, “Nyquist-stability-criterion-based SSR explanation for type-3 wind generators,” *IEEE Trans. Energy Convers.*, vol. 27, no. 3, pp. 807–809, Sep. 2012.

- [38] Z. Miao, “Impedance-model-based SSR analysis for type 3 wind generator and series-compensated network,” *IEEE Trans. Energy Convers.*, vol. 27, no. 4, pp. 984–991, Dec. 2012.
- [39] ———, “Impact of unbalance on electrical and torsional resonances in power electronic interfaced wind energy systems,” *IEEE Trans. Power Syst.*, vol. 28, no. 3, pp. 3105–3113, Aug. 2013.
- [40] L. A. Pilotto, A. Bianco, W. F. Long, and A.-A. Edris, “Impact of tcsc control methodologies on subsynchronous oscillations,” *IEEE Trans. Power Del.*, vol. 18, no. 1, pp. 243–252, Jan. 2003.
- [41] R. K. Varma, S. Auddy, and Y. Semsedini, “Mitigation of subsynchronous resonance in a series-compensated wind farm using FACTS controllers,” *IEEE Trans. Power Del.*, vol. 23, no. 3, pp. 1645–1654, Jul. 2008.
- [42] D. Jovicic and G. N. Pillai, “Analytical modeling of TCSC dynamics,” *IEEE Trans. Power Del.*, vol. 20, no. 2, pp. 1097–1104, Apr. 2005.
- [43] X. Jiang and A. Gole, “A frequency scanning method for the identification of harmonic instabilities in hvdc systems,” *IEEE Trans. Power Del.*, vol. 10, no. 4, pp. 1875–1881, Nov. 1995.
- [44] N. Johansson, L. Angquist, and H.-P. Nee, “A comparison of different frequency scanning methods for study of subsynchronous resonance,” *IEEE Trans. Power Syst.*, vol. 26, no. 1, pp. 356–363, Feb. 2011.
- [45] S. G. Jalali, R. A. Hedin, M. Pereira, and K. Sadek, “A stability model for the advanced series compensator (ASC),” *IEEE Trans. Power Del.*, vol. 11, no. 2, pp. 1128–1137, Apr. 1996.
- [46] P. Mattavelli, G. C. Verghese, and A. M. Stankovic, “Phasor dynamics of thyristor-controlled series capacitor systems,” *IEEE Trans. Power Syst.*, vol. 12, no. 3, pp. 1259–1267, Aug. 1997.
- [47] N. G. Hingorani and L. Gyugyi, *Understanding FACTS: concepts and technology of flexible AC transmission systems*. IEEE press New York, 2000.
- [48] M. Belkhat, “Stability criteria for ac power systems with regulated loads,” Ph.D. dissertation, Purdue University, West Lafayette, 1997.
- [49] M. Céspedes and J. Sun, “Modeling and mitigation of harmonic resonance between wind turbines and the grid,” in *Energy Conversion Congress and Exposition (ECCE)*. IEEE, 2011, pp. 2109–2116.
- [50] B. Friedland, *Control System Design: an introduction to state-space methods*. Courier Dover Publications, 2005.
- [51] IEEE SSR Working Group, “Second benchmark model for computer simulation of subsynchronous resonance,” *IEEE Trans. Power App. Syst.*, vol. 104, no. 5, pp. 1057–1066, 1985.

- [52] L. Fan, R. Kavasseri, Z. L. Miao, and C. Zhu, "Modeling of DFIG-based wind farms for SSR analysis," *IEEE Trans. Power Del.*, vol. 25, no. 4, pp. 2073–2082, Oct. 2010.
- [53] M. Braun, G. Arnold, and H. Laukamp, "Plugging into the zeitgeist," vol. 7, no. 3, pp. 63–76, 2009.
- [54] A. K. Abdelsalam, A. M. Massoud, S. Ahmed, and P. N. Enjeti, "High-performance adaptive perturb and observe mppt technique for photovoltaic-based microgrids," *IEEE Trans. Power Electron.*, vol. 26, no. 4, pp. 1010–1021, 2011.
- [55] H. Kanchev, D. Lu, F. Colas, V. Lazarov, and B. Francois, "Energy management and operational planning of a microgrid with a PV-based active generator for smart grid applications," *IEEE Trans. Ind. Electron.*, vol. 58, no. 10, pp. 4583–4592, 2011.
- [56] K. Tan, P. So, Y. Chu, and M. Chen, "Coordinated control and energy management of distributed generation inverters in a microgrid," *IEEE Trans. Power Del.*, vol. 28, no. 2, pp. 704–713, Apr. 2013.
- [57] *PSCAD Manual*, Manitoba HVDC Research Center. [Online]. Available: www.pscad.com
- [58] *SimPowerSystems For Use with Simulink®*, TransÉnergie Technologies Hydro-Québec. [Online]. Available: <http://www.mathworks.com>
- [59] J. Sun, "Small-signal methods for ac distributed power systems—a review," *IEEE Trans. Power Electron.*, vol. 24, no. 11, pp. 2545–2554, 2009.
- [60] A. M. Stankovic and T. Aydin, "Analysis of asymmetrical faults in power systems using dynamic phasors," *Power Systems, IEEE Transactions on*, vol. 15, no. 3, pp. 1062–1068, 2000.
- [61] P. C. Stefanov and A. M. Stankovic, "Modeling of upfc operation under unbalanced conditions with dynamic phasors," *Power Systems, IEEE Transactions on*, vol. 17, no. 2, pp. 395–403, 2002.
- [62] M. Daryabak, S. Filizadeh, J. Jatskevich, A. Davoudi, M. Saeedifard, V. Sood, J. Martinez, D. Aliprantis, J. Cano, and A. Mehrizi-Sani, "Modeling of lcc-hvdc systems using dynamic phasors," 2014.
- [63] V. A. Caliskan, O. Verghese, and A. M. Stankovic, "Multifrequency averaging of dc/dc converters," *IEEE Trans. Power Electron.*, vol. 14, no. 1, pp. 124–133, 1999.
- [64] A. M. Stankovic, B. C. Lesieutre, and T. Aydin, "Modeling and analysis of single-phase induction machines with dynamic phasors," *Power Systems, IEEE Transactions on*, vol. 14, no. 1, pp. 9–14, 1999.
- [65] G. Díaz, C. Gonzalez-Moran, J. Gomez-Aleixandre, and A. Diez, "Complex-valued state matrices for simple representation of large autonomous microgrids supplied by pq and vf generation," *IEEE Trans. Power Syst.*, vol. 24, no. 4, pp. 1720–1730, 2009.

- [66] N. L. Sultanis, S. A. Papathanasiou, and N. D. Hatziargyriou, "A stability algorithm for the dynamic analysis of inverter dominated unbalanced lv microgrids," *IEEE Trans. Power Syst.*, vol. 22, no. 1, pp. 294–304, 2007.
- [67] L. Piyasinghe, Z. Miao, and L. Fan, "Dynamic phasor based model of type 1 wind generator for unbalanced operation," in *Power Electronics and Machines in Wind Applications (PEMWA)*. IEEE, 2012, pp. 1–5.
- [68] O. Gomis-Bellmunt, A. Junyent-Ferre, A. Sumper, and J. Bergas-Jan, "Ride-through control of a doubly fed induction generator under unbalanced voltage sags," *IEEE Trans. Energy Convers.*, vol. 23, no. 4, pp. 1036–1045, 2008.
- [69] M. Ciobotaru, R. Teodorescu, and F. Blaabjerg, "Control of single-stage single-phase pv inverter," in *European Conference on Power Electronics and Applications*. IEEE, 2005, pp. 10–pp.
- [70] C. Meza, J. J. Negroni, D. Biel, and F. Guinjoan, "Energy-balance modeling and discrete control for single-phase grid-connected pv central inverters," *IEEE Trans. Ind. Electron.*, vol. 55, no. 7, pp. 2734–2743, 2008.
- [71] Y. Yang, K. Zhou, and F. Blaabjerg, "Harmonics suppression for single-phase grid-connected photovoltaic systems in different operation modes," in *The Applied Power Electronics Conference and Exposition, 2013*.
- [72] Y. Wang, P. Zhang, W. Li, W. Xiao, and A. Abdollahi, "Online overvoltage prevention control of photovoltaic generators in microgrids," *IEEE trans. Smart Grid*, vol. 3, no. 4, pp. 2071–2078, Dec 2012.
- [73] A. Yazdani and R. Iravani, *Voltage-sourced converters in power systems: modeling, control, and applications*. John Wiley & Sons, 2010.
- [74] Z. Miao, L. Xu, V. Disfani, and L. Fan, "An soc-based battery management system for microgrids," *Smart Grid, IEEE Transactions on*, vol. 5, no. 2, pp. 966–973, March 2014.
- [75] L. Xu, Z. Miao, and L. Fan, "Control of a back-to-back vsc system from grid-connection to islanded mode in microgrids," in *Energytech, 2011 IEEE*. IEEE, 2011, pp. 1–6.
- [76] W. Li, G. Joós, and J. Bélanger, "Real-time simulation of a wind turbine generator coupled with a battery supercapacitor energy storage system," *Industrial Electronics, IEEE Transactions on*, vol. 57, no. 4, pp. 1137–1145, 2010.
- [77] C. Abbey and G. Joós, "A stochastic optimization approach to rating of energy storage systems in wind-diesel isolated grids," *Power Systems, IEEE Transactions on*, vol. 24, no. 1, pp. 418–426, 2009.
- [78] L. Kuznia, B. Zeng, G. Centeno, and Z. Miao, "Stochastic optimization for power system configuration with renewable energy in remote areas," *Annals of Operations Research*, vol. 210, no. 1, pp. 411–432, 2013.







- [79] S. Teleke, M. Baran, S. Bhattacharya, and A. Huang, "Optimal control of battery energy storage for wind farm dispatching," *Energy Conversion, IEEE Transactions on*, vol. 25, no. 3, pp. 787–794, Sept 2010.
- [80] R. Hermans, M. Almassalkhi, and I. Hiskens, "Incentive-based coordinated charging control of plug-in electric vehicles at the distribution-transformer level," in *American Control Conference (ACC), 2012*. IEEE, 2012, pp. 264–269.
- [81] Y. Riffonneau, S. Bacha, F. Barruel, and S. Ploix, "Optimal power flow management for grid connected pv systems with batteries," *Sustainable Energy, IEEE Transactions on*, vol. 2, no. 3, pp. 309–320, July 2011.
- [82] G. Gurlaskie, Z. Miao, L. Fan, L. Xu, V. Disfani, L. Piyasinghe, and J. Khazaei, "Final report submitted to duke energy: Community power systems simulation," University of South Florida, FL, Tech. Rep., 2014.
- [83] R. Huang, T. Huang, R. Gadh, and N. Li, "Solar generation prediction using the arma model in a laboratory-level micro-grid," in *Smart Grid Communications (SmartGridComm), 2012 IEEE Third International Conference on*. IEEE, 2012, pp. 528–533.
- [84] "ComEd, Historical Load Profiles," <https://www.comed.com/customer-service/rates-pricing/retail-electricity-metering/Pages/historical-load-data.aspx>, 2015, [Online; accessed 01-01-2015].
- [85] M. Grant, S. Boyd, and Y. Ye, "Cvx: Matlab software for disciplined convex programming," 2008.
- [86] F. Katiraei, M. Iravani, and P. Lehn, "Micro-grid autonomous operation during and subsequent to islanding process," *Power Delivery, IEEE Transactions on*, vol. 20, no. 1, pp. 248 – 257, jan. 2005.
- [87] C. Schauder and H. Mehta, "Vector analysis and control of advanced static var compensators," *Generation, Transmission and Distribution, IEE Proceedings C*, vol. 140, no. 4, pp. 299–306, jul 1993.
- [88] G. Li, M. Yin, M. Zhou, and C. Zhao, "Modeling of vsc-hvdc and control strategies for supplying both active and passive systems," in *Power Engineering Society General Meeting, 2006. IEEE*, 0-0 2006, p. 6 pp.
- [89] H. Chen, "Research on the control strategy of vsc based hvdc system supplying passive network," in *Power Energy Society General Meeting, 2009. PES '09. IEEE*, july 2009, pp. 1–4.
- [90] Y. Chen, A. Oudalov, and J. Wang, "Integration of electric vehicle charging system into distribution network," in *Power Electronics and ECCE Asia (ICPE & ECCE), 2011 IEEE*, May-June 2011, pp. 593 – 598.
- [91] J. Crider and S. Sudhoff, "Reducing impact of pulsed power loads on microgrid power systems," *IEEE Trans. Smart Grid*, vol. 1, no. 3, pp. 270–277, Dec. 2010.


- [92] N. Mohan and J. Broach, “Converters for supplying pulsed power loads,” *IEEE Trans. Ind. Appl.*, no. 1, pp. 85–91, Jan. 1979.
- [93] M. Steurer, M. Andrus, J. Langston, L. Qi, S. Suryanarayanan, S. Woodruff, and P. Ribeiro, “Investigating the impact of pulsed power charging demands on shipboard power quality,” in *Electric Ship Technologies Symposium, 2007. ESTS '07. IEEE*, May 2007, pp. 315 – 321.
- [94] B. Cassimere, C. R. Valdez, S. Sudhoff, S. Pekarek, B. Kuhn, D. Delisle, and E. Zivi, “System impact of pulsed power loads on a laboratory scale integrated fight through power (iftp) system,” in *Electric Ship Technologies Symposium, 2005 IEEE*, July 2005, pp. 176 – 183.
- [95] H. Smolleck, S. Ranade, N. Prasad, and R. Velasco, “Effect of pulsed-power loads upon an electric power grid,” *IEEE Trans. Power Del.*, vol. 6, no. 4, pp. 1629–1640, Oct. 1991.
- [96] Z. Miao, A. Domijan, and L. Fan, “Investigation of microgrids with both inverter interfaced and direct ac-connected distributed energy resources,” *IEEE Trans. Power Del.*, vol. 26, no. 3, pp. 1634–1642, JULY 2011.
- [97] I. Kamwa, D. Lefebvre, and L. Loud, “Small signal analysis of hydro-turbine governors in large interconnected power plants,” in *Power Engineering Society Winter Meeting, 2002. IEEE*, vol. 2, 2002, pp. 1178 – 1183 vol.2.
- [98] S. Wall, “Performance of inverter interfaced distributed generation,” in *Transmission and Distribution Conference and Exposition, 2001 IEEE/PES*, vol. 2, 2001, pp. 945 –950 vol.2.
- [99] A. Yazdani and R. Iravani, *Voltage-Sourced Converters in Power Systems*. John Wiley & Sons, Inc., 2010.
- [100] C. Schauder and H. Mehta, “Vector analysis and control of advanced static var compensators,” *Generation, Transmission and Distribution, IEE Proceedings C*, vol. 140, no. 4, pp. 299 –306, jul 1993.
- [101] “Ieee recommended practices and requirements for harmonic control in electrical power systems,” *IEEE Std 519-1992*, 1993.
- [102] J. Sun, D. Czarkowski, and Z. Zabbar, “Voltage flicker mitigation using pwm-based distribution statcom,” in *Power Engineering Society Summer Meeting, 2002 IEEE*, vol. 1, july 2002, pp. 616 –621 vol.1.
- [103] M. Steurer, C. Edrington, M. Sloderbeck, W. Ren, and J. Langston, “A megawatt-scale power hardware-in-the-loop simulation setup for motor drives,” *Industrial Electronics, IEEE Transactions on*, vol. 57, no. 4, pp. 1254–1260, 2010.
- [104] H. Li, M. Steurer, K. L. Shi, S. Woodruff, and D. Zhang, “Development of a unified design, test, and research platform for wind energy systems based on hardware-in-the-loop real-time simulation,” *Industrial Electronics, IEEE Transactions on*, vol. 53, no. 4, pp. 1144–1151, 2006.
- [105] O. Craciun, A. Florescu, S. Bacha, I. Munteanu, and A. I. Bratcu, “Hardware-in-the-loop testing of pv control systems using rt-lab simulator,” in *Power Electronics and Motion Control Conference (EPE/PEMC), 2010 14th International*. IEEE, 2010, pp. S2–1.

- [106] L. Gauchia and J. Sanz, “A per-unit hardware-in-the-loop simulation of a fuel cell/battery hybrid energy system,” *Industrial Electronics, IEEE Transactions on*, vol. 57, no. 4, pp. 1186–1194, 2010.
- [107] K. Burman, D. Olis, V. Gevorgian, A. Warren, R. Butt, P. Lilienthal, and J. Glassmire, “Integrating renewable energy into the transmission and distribution system of the us virgin islands,” National Renewable Energy Laboratory (NREL), Golden, CO., Tech. Rep., 2011.
- [108] P. F. Ribeiro, B. K. Johnson, M. L. Crow, A. Arsoy, and Y. Liu, “Energy storage systems for advanced power applications,” *Proceedings of the IEEE*, vol. 89, no. 12, pp. 1744–1756, 2001.
- [109] T. B. Johansson and L. Burnham, *Renewable energy: sources for fuels and electricity*. Island press, 1993.
- [110] C. Dufour, S. Abourida, and J. Bélanger, “Hardware-in-the-loop simulation of power drives with rt-lab,” in *Power Electronics and Drives Systems, 2005. PEDS 2005. International Conference on*, vol. 2. IEEE, 2005, pp. 1646–1651.
- [111] V. Jalili-Marandi, L.-F. Pak, and V. Dinavahi, “Real-time simulation of grid-connected wind farms using physical aggregation,” *Industrial Electronics, IEEE Transactions on*, vol. 57, no. 9, pp. 3010–3021, 2010.
- [112] R. Teodorescu and F. Blaabjerg, “Proportional-resonant controllers. a new breed of controllers suitable for grid-connected voltage-source converters,” 2004.


APPENDICES

Appendix A Reuse Permissions of Published Papers for Chapters 3, 4, 5, 7, 8

 **Copyright Clearance Center**  **RightsLink**     **Live Chat**

 **IEEE**
Requesting permission to reuse content from an IEEE publication

Title: An optimal power flow algorithm considering wind power penetration
Conference Proceedings: North American Power Symposium (NAPS), 2011
Author: Piyasinghe, L.P.; Lingling Fan
Publisher: IEEE
Date: 4-6 Aug. 2011
Copyright © 2011, IEEE

Logged in as:
Lakshan Piyasinghe
 **LOGOUT**

Thesis / Dissertation Reuse

The IEEE does not require individuals working on a thesis to obtain a formal reuse license, however, you may print out this statement to be used as a permission grant:

Requirements to be followed when using any portion (e.g., figure, graph, table, or textual material) of an IEEE copyrighted paper in a thesis:

- 1) In the case of textual material (e.g., using short quotes or referring to the work within these papers) users must give full credit to the original source (author, paper, publication) followed by the IEEE copyright line © 2011 IEEE.
- 2) In the case of illustrations or tabular material, we require that the copyright line © [Year of original publication] IEEE appear prominently with each reprinted figure and/or table.
- 3) If a substantial portion of the original paper is to be used, and if you are not the senior author, also obtain the senior author's approval.

Requirements to be followed when using an entire IEEE copyrighted paper in a thesis:

- 1) The following IEEE copyright/ credit notice should be placed prominently in the references: © [year of original publication] IEEE. Reprinted, with permission, from [author names, paper title, IEEE publication title, and month/year of publication]
- 2) Only the accepted version of an IEEE copyrighted paper can be used when posting the paper or your thesis on-line.
- 3) In placing the thesis on the author's university website, please display the following message in a prominent place on the website: In reference to IEEE copyrighted material which is used with permission in this thesis, the IEEE does not endorse any of [university/educational entity's name goes here]'s products or services. Internal or personal use of this material is permitted. If interested in reprinting/republishing IEEE copyrighted material for advertising or promotional purposes or for creating new collective works for resale or redistribution, please go to http://www.ieee.org/publications_standards/publications/rights/rights_link.htm to learn how to obtain a License from RightsLink.


If applicable, University Microfilms and/or ProQuest Library, or the Archives of Canada may supply single copies of the dissertation.

 **BACK**


 **CLOSE WINDOW**

Copyright © 2015 [Copyright Clearance Center, Inc.](#) All Rights Reserved. [Privacy statement](#). [Terms and Conditions](#).
Comments? We would like to hear from you. E-mail us at customercare@copyright.com

Appendix A (Continued)



Home Account Info Help Live Chat



Title: Initialization of unbalanced radial distribution systems for small signal stability analysis
Conference Proceedings: Power & Energy Society General Meeting, 2015 IEEE
Author: Khazaei, J.; Zhixin Miao; Piyasinghe, L.; Lingling Fan
Publisher: IEEE
Date: 26-30 July 2015
Copyright © 2015, IEEE

Logged in as:
Lakshan Piyasinghe
Account #:
3000958370
LOGOUT

Thesis / Dissertation Reuse

The IEEE does not require individuals working on a thesis to obtain a formal reuse license, however, you may print out this statement to be used as a permission grant:

Requirements to be followed when using any portion (e.g., figure, graph, table, or textual material) of an IEEE copyrighted paper in a thesis:

- 1) In the case of textual material (e.g., using short quotes or referring to the work within these papers) users must give full credit to the original source (author, paper, publication) followed by the IEEE copyright line © 2011 IEEE.
- 2) In the case of illustrations or tabular material, we require that the copyright line © [Year of original publication] IEEE appear prominently with each reprinted figure and/or table.
- 3) If a substantial portion of the original paper is to be used, and if you are not the senior author, also obtain the senior author's approval.

Requirements to be followed when using an entire IEEE copyrighted paper in a thesis:

- 1) The following IEEE copyright/ credit notice should be placed prominently in the references: © [year of original publication] IEEE. Reprinted, with permission, from [author names, paper title, IEEE publication title, and month/year of publication]
- 2) Only the accepted version of an IEEE copyrighted paper can be used when posting the paper or your thesis on-line.
- 3) In placing the thesis on the author's university website, please display the following message in a prominent place on the website: In reference to IEEE copyrighted material which is used with permission in this thesis, the IEEE does not endorse any of [university/educational entity's name goes here]'s products or services. Internal or personal use of this material is permitted. If interested in reprinting/republishing IEEE copyrighted material for advertising or promotional purposes or for creating new collective works for resale or redistribution, please go to http://www.ieee.org/publications_standards/publications/rights/rights_link.html to learn how to obtain a License from RightsLink.

If applicable, University Microfilms and/or ProQuest Library, or the Archives of Canada may supply single copies of the dissertation.

BACK

CLOSE WINDOW

Copyright © 2015 Copyright Clearance Center, Inc. All Rights Reserved. [Privacy statement](#), [Terms and Conditions](#).

Comments? We would like to hear from you. E-mail us at customercare@copyright.com

Appendix A (Continued)

9/17/2015

Rightslink® by Copyright Clearance Center



RightsLink®

[Home](#) [Account Info](#) [Help](#)



Title: Impedance Model-Based SSR Analysis for TCSC Compensated Type-3 Wind Energy Delivery Systems
Author: Piyasinghe, L.; Zhixin Miao; Khazaei, J.; Lingling Fan
Publication: Sustainable Energy, IEEE Transactions on
Publisher: IEEE
Date: Jan. 2015
Copyright © 2015, IEEE

Logged in as:
Lakshan Piyasinghe

[LOGOUT](#)

Thesis / Dissertation Reuse

The IEEE does not require individuals working on a thesis to obtain a formal reuse license, however, you may print out this statement to be used as a permission grant:

Requirements to be followed when using any portion (e.g., figure, graph, table, or textual material) of an IEEE copyrighted paper in a thesis:

- 1) In the case of textual material (e.g., using short quotes or referring to the work within these papers) users must give full credit to the original source (author, paper, publication) by the IEEE copyright line © 2011 IEEE.
- 2) In the case of illustrations or tabular material, we require that the copyright line © [Year of original publication] IEEE appear prominently with each reprinted figure and/or table.
- 3) If a substantial portion of the original paper is to be used, and if you are not the senior author, also obtain the senior author's approval.

Requirements to be followed when using an entire IEEE copyrighted paper in a thesis:

- 1) The following IEEE copyright/ credit notice should be placed prominently in the references: © [year of original publication] IEEE. Reprinted, with permission, from [author names, paper title, IEEE publication title, and month/year of publication]
- 2) Only the accepted version of an IEEE copyrighted paper can be used when posting the paper or your thesis on-line.
- 3) In placing the thesis on the author's university website, please display the following message in a prominent place on the website: In reference to IEEE copyrighted material which is used with permission in this thesis, the IEEE does not endorse any of [university/educational entity's name goes here]'s products or services. Internal or personal use of this material is permitted. If interested in reprinting/republishing IEEE copyrighted material for advertising or promotional purposes or for creating new collective works for resale or redistribution, please go to http://www.ieee.org/publications_standards/publications/rights/rights_link.html to learn how to obtain a License from RightsLink.

If applicable, University Microfilms and/or ProQuest Library, or the Archives of Canada may supply single copies of the dissertation.

[BACK](#)

[CLOSE WINDOW](#)


Copyright © 2015 [Copyright Clearance Center, Inc.](#) All Rights Reserved. [Privacy statement](#). [Terms and Conditions](#).
Comments? We would like to hear from you. E-mail us at customercare@copyright.com


<https://s100.copyright.com/AppDispatchServlet#formTop>


1/1


Appendix A (Continued)

9/17/2015 Rightslink® by Copyright Clearance Center

 **Copyright Clearance Center**

 **RightsLink®**

[Home](#) [Account Info](#) [Help](#)  **Live Chat**

 **IEEE**
Requesting permission to reuse content from an IEEE publication

Title: Dynamic Phasor-Based Modeling of Unbalanced Radial Distribution Systems

Author: Zhixin Miao; Piyasinghe, L.; Khazaei, J.; Lingling Fan

Publication: Power Systems, IEEE Transactions on

Publisher: IEEE

Date: Nov. 2015

Copyright © 2015, IEEE

Logged in as:
Lakshan Piyasinghe
[LOGOUT](#)

Thesis / Dissertation Reuse

The IEEE does not require individuals working on a thesis to obtain a formal reuse license, however, you may print out this statement to be used as a permission grant:

Requirements to be followed when using any portion (e.g., figure, graph, table, or textual material) of an IEEE copyrighted paper in a thesis:

- 1) In the case of textual material (e.g., using short quotes or referring to the work within these papers) users must give full credit to the original source (author, paper, publication) followed by the IEEE copyright line © 2011 IEEE.
- 2) In the case of illustrations or tabular material, we require that the copyright line © [Year of original publication] IEEE appear prominently with each reprinted figure and/or table.
- 3) If a substantial portion of the original paper is to be used, and if you are not the senior author, also obtain the senior author's approval.

Requirements to be followed when using an entire IEEE copyrighted paper in a thesis:

- 1) The following IEEE copyright/ credit notice should be placed prominently in the references: © [year of original publication] IEEE. Reprinted, with permission, from [author names, paper title, IEEE publication title, and month/year of publication]
- 2) Only the accepted version of an IEEE copyrighted paper can be used when posting the paper or your thesis on-line.
- 3) In placing the thesis on the author's university website, please display the following message in a prominent place on the website: In reference to IEEE copyrighted material which is used with permission in this thesis, the IEEE does not endorse any of [university/educational entity's name goes here]'s products or services. Internal or personal use of this material is permitted. If interested in reprinting/republishing IEEE copyrighted material for advertising or promotional purposes or for creating new collective works for resale or redistribution, please go to http://www.ieee.org/publications_standards/publications/rights/rights_link.html to learn how to obtain a License from RightsLink.

If applicable, University Microfilms and/or ProQuest Library, or the Archives of Canada may supply single copies of the dissertation.

[BACK](#)

[CLOSE WINDOW](#)

Copyright © 2015 [Copyright Clearance Center, Inc.](#) All Rights Reserved. [Privacy statement](#) [Terms and Conditions](#).
Comments? We would like to hear from you. E-mail us at customercare@copyright.com

Appendix A (Continued)



Lakshan Piyasinghe <lakshan@mail.usf.edu>

FW: RE: Fwd: Reuse Permission -Journal of Technology and Innovation

5 messages

bob@cognizantcommunication.com <bob@cognizantcommunication.com> Wed, Oct 14, 2015 at 10:34 AM
To: lakshan@mail.usf.edu

-----Original Message-----

From: bob@cognizantcommunication.com
Sent: Wednesday, October 14, 2015 10:28am
To: lakshan@gmail.usf.edu
Cc: Imiranda@cognizantcommunication.com
Subject: RE: Fwd: Reuse Permission -Journal of Technology and Innovation

Permission Granted Bob Miranda Cognizant Communication Corp.

--

---Original Message-----

From: "Inquiries Cognizant Communication" <inquiries@cognizantcommunication.com>
Sent: Wednesday, October 14, 2015 8:34am
To: "Bob Miranda" <bob@cognizantcommunication.com>
Subject: Fwd: Reuse Permission -Journal of Technology and Innovation

Sent from my iPhone

Begin forwarded message:

From: Lakshan Piyasinghe <lakshan@mail.usf.edu>
Date: October 13, 2015 at 9:05:47 PM EDT
To: inquiries@cognizantcommunication.com
Subject: Reuse Permission -Journal of Technology and Innovation

Dear Sir/Madam

I'm Lakshan Piyasinghe, a PhD candidate at the University of South Florida. I have a paper published in journal of Technology and Innvoation. Following are the details of the article.

Title: DROOP CONTROL IN VOLTAGE SOURCE CONVERTERS FOR MICROGRID OPERATION WITH PULSED POWER LOADS


Source: Technology & Innovation, Volume 14, Number 2, 2012, pp. 167-178(12)

I would like to reuse this material for my dissertation, which is due by the end of this semester.


Could you please let me know how can I get the Reuse Persmisson for the particular article.

Thanks you very much for your valued time and the consideration.

Appendix A (Continued)



Home Account Info Help Live Chat



Title: Real-time simulation and hardware-in-the-loop tests of a battery system
Conference Proceedings: Power & Energy Society General Meeting, 2015 IEEE
Author: Khazaei, J.; Piyasinghe, L.; Disfani, V.R.; Zhixin Miao; Lingling Fan; Gurlaskie, G.
Publisher: IEEE
Date: 26-30 July 2015

Logged in as:
Lakshan Piyasinghe
Account #:
3000958370
[LOGOUT](#)

Copyright © 2015, IEEE

Thesis / Dissertation Reuse

The IEEE does not require individuals working on a thesis to obtain a formal reuse license, however, you may print out this statement to be used as a permission grant:

Requirements to be followed when using any portion (e.g., figure, graph, table, or textual material) of an IEEE copyrighted paper in a thesis:

- 1) In the case of textual material (e.g., using short quotes or referring to the work within these papers) users must give full credit to the original source (author, paper, publication) followed by the IEEE copyright line © 2011 IEEE.
- 2) In the case of illustrations or tabular material, we require that the copyright line © [Year of original publication] IEEE appear prominently with each reprinted figure and/or table.
- 3) If a substantial portion of the original paper is to be used, and if you are not the senior author, also obtain the senior author's approval.

Requirements to be followed when using an entire IEEE copyrighted paper in a thesis:

- 1) The following IEEE copyright/ credit notice should be placed prominently in the references: © [year of original publication] IEEE. Reprinted, with permission, from [author names, paper title, IEEE publication title, and month/year of publication]
- 2) Only the accepted version of an IEEE copyrighted paper can be used when posting the paper or your thesis on-line.
- 3) In placing the thesis on the author's university website, please display the following message in a prominent place on the website: In reference to IEEE copyrighted material which is used with permission in this thesis, the IEEE does not endorse any of [university/educational entity's name goes here]'s products or services. Internal or personal use of this material is permitted. If interested in reprinting/republishing IEEE copyrighted material for advertising or promotional purposes or for creating new collective works for resale or redistribution, please go to http://www.ieee.org/publications_standards/publications/rights/rights_link.html to learn how to obtain a License from RightsLink.

If applicable, University Microfilms and/or ProQuest Library, or the Archives of Canada may supply single copies of the dissertation.

[BACK](#)

[CLOSE WINDOW](#)

Copyright © 2015 [Copyright Clearance Center, Inc.](#) All Rights Reserved. [Privacy statement](#) [Terms and Conditions](#).
Comments? We would like to hear from you. E-mail us at customercare@copyright.com

Appendix A (Continued)

9/17/2015 Rightslink® by Copyright Clearance Center

 **Copyright Clearance Center**

 **RightsLink®**

[Home](#) [Account Info](#) [Help](#) [Live Chat](#)

 **IEEE**
Requesting permission to reuse content from an IEEE publication

Title: Real-time digital simulation modeling of single-phase PV in RT-LAB

Conference Proceedings: PES General Meeting | Conference & Exposition, 2014 IEEE

Author: Khazaei, J.; Piyasinghe, L.; Zhixin Miao; Lingling Fan

Publisher: IEEE

Date: 27-31 July 2014

Copyright © 2014, IEEE

Logged in as:
Lakshan Piyasinghe
[LOGOUT](#)

Thesis / Dissertation Reuse

The IEEE does not require individuals working on a thesis to obtain a formal reuse license, however, you may print out this statement to be used as a permission grant:

Requirements to be followed when using any portion (e.g., figure, graph, table, or textual material) of an IEEE copyrighted paper in a thesis:

- 1) In the case of textual material (e.g., using short quotes or referring to the work within these papers) users must give full credit to the original source (author, paper, publication) followed by the IEEE copyright line © 2011 IEEE.
- 2) In the case of illustrations or tabular material, we require that the copyright line © [Year of original publication] IEEE appear prominently with each reprinted figure and/or table.
- 3) If a substantial portion of the original paper is to be used, and if you are not the senior author, also obtain the senior author's approval.

Requirements to be followed when using an entire IEEE copyrighted paper in a thesis:

- 1) The following IEEE copyright/ credit notice should be placed prominently in the references: © [year of original publication] IEEE. Reprinted, with permission, from [author names, paper title, IEEE publication title, and month/year of publication]
- 2) Only the accepted version of an IEEE copyrighted paper can be used when posting the paper or your thesis on-line.
- 3) In placing the thesis on the author's university website, please display the following message in a prominent place on the website: In reference to IEEE copyrighted material which is used with permission in this thesis, the IEEE does not endorse any of [university/educational entity's name goes here]'s products or services. Internal or personal use of this material is permitted. If interested in reprinting/republishing IEEE copyrighted material for advertising or promotional purposes or for creating new collective works for resale or redistribution, please go to http://www.ieee.org/publications_standards/publications/rights/rights_link.html to learn how to obtain a License from RightsLink.

If applicable, University Microfilms and/or ProQuest Library, or the Archives of Canada may supply single copies of the dissertation.

[BACK](#)

[CLOSE WINDOW](#)

Copyright © 2015 [Copyright Clearance Center, Inc.](#) All Rights Reserved. [Privacy statement](#). [Terms and Conditions](#).
Comments? We would like to hear from you. E-mail us at customercare@copyright.com

ABOUT THE AUTHOR

Lakshan Piyasinghe was born in 1982 in Gampola Sri Lanka. He obtained his bachelor degree in Electrical Engineering from University of Moratuwa, Sri Lanka in 2006 and his Master's degree from University of South Florida in July, 2013. He received his Ph.D. degree in Electrical Engineering from the University of South Florida in December, 2015. His research interests include modeling of Renewable energy sources and power electronics, Stability analysis and real-time digital simulation.